

Multifluid Simulations of the Magnetorotational Instability in Accretion Disks Around Protostars

Wayne O’Keeffe

B.Sc.

A Dissertation Submitted for the Degree of Doctor of Philosophy

Dublin City University

Supervisor:

Dr. Turlough P. Downes

School of Mathematical Sciences

Dublin City University

June 2013

Declaration

I hereby certify that this material, which I now submit for assessment on the programme of study leading to the award of Doctor of Philosophy is entirely my own work, that I have exercised reasonable care to ensure that the work is original, and does not to the best of my knowledge breach any law of copyright, and has not been taken from the work of others save and to the extent that such work has been cited and acknowledged within the text of my work.

Signed: _____

ID Number: 57118141

Date: 25th June 2013

Acknowledgements

There are many people and organisations I would like to thank for their help in completing this work.

Firstly I would like to thank my supervisor, Dr. Turlough Downes, whose support, guidance, and enthusiasm helped me greatly along the way.

I would like to thank all present and former members of the astrophysics group, Aoife, Seán, Steven, Sarah and Mohsen for giving me their time and helping me along the way and also would like to thank all those I have met in the Dublin Institute of Advanced Studies, I learned so much during our group discussions. A special thanks to all the postgrads and staff in DCU, both past and present for providing such a fun and friendly work environment, I made some great friends during my time there. A very important thanks to the Department of mathematical sciences in DCU for providing financial support during my fourth year, without this it would have been a much harder journey.

I would like to thank the SFI/HEA Irish Centre for High-End Computing (ICHEC) and SCI-SYM for their support and access to very important computational resources used in developing the code to complete this work. A very special thanks goes to Jülich Supercomputing Centre in Germany for supplying the compute hours to complete the resolution study and production runs presented in this work without which this work would not have been possible.

Finally I like to thank my family and friends for their support and for helping me when my enthusiasm wavered and the work got the better of me, and for tearing me away from the computer screen when required. I couldn't have done it without you.

Contents

1	Introduction	1
1.1	Molecular Clouds	2
1.1.1	Giant Molecular Clouds	2
1.1.2	Cloud Cores and Gravitational Collapse	4
1.1.3	Role of Magnetic Fields	8
1.2	Process of Star Formation	11
1.2.1	First and Second Hydrostatic cores	11
1.2.2	Protostars	12
1.2.3	High-Mass Star Formation	14
1.2.4	Main-Sequence of stars	14
1.3	Accretion disks	16
1.3.1	Accretion Mechanisms	18
1.4	The Magnetorotational Instability	24
1.4.1	Simplified description of the MRI	25
1.4.2	Growth and Saturation of the instability.	26
1.4.3	Channel Solutions	27
2	Magnetohydrodynamics	29
2.1	MHD models	30
2.2	The Multi-fluid Model	39

2.3	Generalised Ohm's Law	42
2.4	Multifluid MRI	47
3	Numerical Methods	56
3.1	The multifluid Equations	57
3.2	HYDRA: Multifluid MHD code	60
3.2.1	Numerical Algorithm	61
3.2.2	$\nabla \cdot \mathbf{B}$ control	63
3.3	Stability Analysis	65
3.3.1	Super-time-stepping	69
3.3.2	Hall Diffusion Scheme	70
3.4	Accretion Disk Model	72
3.4.1	Computational Domain	73
3.4.2	Gravity	74
3.4.3	Boundary Conditions	75
3.4.4	Initial conditions	77
3.4.5	Units	80
4	Resolution Study	83
4.1	Analysis techniques	84
4.1.1	Magnetic and Kinetic Stresses	84
4.1.2	Magnetic and Kinetic Energies	86
4.2	Comparison Between Global and Quarter disk approaches	87
4.3	Ideal MHD Resolution Study	90
4.3.1	Ideal Case: Maxwell Stress and Alpha Parameter	91
4.3.2	Ideal Case: Magnetic and Kinetic Energies	93

4.3.3	Comparisons of ideal MHD regime with previous numerical studies	97
4.4	Multifluid Resolution Study	100
4.4.1	Multifluid Case: Maxwell Stress and Alpha Parameter	100
4.4.2	Multifluid Case: Magnetic and Kinetic Energies	103
5	Ideal MHD Versus Multifluid	106
5.1	Comparison of Ideal MHD and Fully Multifluid Studies	107
6	Ambipolar Diffusion Dominated Study of the MRI	116
6.1	Numerical Set-up	116
6.2	Results of Ambipolar Dominated Study of the MRI Compared to the Ideal MHD case	117
6.3	Results of Ambipolar Dominated Study of the MRI Versus the full Multifluid MHD case	121
7	Hall Diffusion Dominated Study of the MRI	128
7.1	Numerical Set-up	128
7.2	Results of Hall Dominated Study of the MRI Versus the Full Multifluid case	129
8	Zero-Net Flux and Initial Field Orientation	137
8.1	Zero-Net Flux case	137
8.1.1	Numerical Set-up	139
8.1.2	Results	140
8.2	Initial Magnetic Field Orientation relative to Rotation Axis of Accretion Disk	145
8.2.1	Numerical Set-up	146
8.2.2	Results	146

Abstract

Turbulence is believed to be of importance in molecular cloud formation as well as the star formation processes within them, such as accretion of matter onto young stars from the surrounding accretion disk.

The kinetic viscosity associated with differentially rotating accretion disks is not believed to be strong enough to account for observed accretion rates. Turbulent motion, driven by the magnetorotational instability (MRI), may provide an anomalous viscosity well in excess of the kinetic viscosity alone leading to enhanced transport of angular momentum, resulting in a higher rate of accretion onto the forming star.

We perform large-scale 3D multifluid simulations of a weakly ionised accretion disk and examine the development and saturation of the turbulence driven by the MRI. This numerical study is carried out using the multifluid MHD code HYDRA.

An important effect of multifluid MHD is diffusion of the magnetic field. Simulations which isolate ambipolar and Hall diffusion are studied individually and comparisons between these and ideal MHD and full multifluid simulations are presented. The stresses (magnetic and kinetic) and an estimation of the anomalous viscosity are calculated for all models. From this information we can determine how accretion is affected by the multifluid physics in the presence of the MRI.

Chapter 1

Introduction

The first modern theories regarding star formation appeared in the 18th century. One of the first was the Nebular Hypothesis which was proposed by Immanuel Kant in 1755 (Kant, 1755). Kant's hypothesis suggested that rotating clouds of gas and dust can collapse and flatten due to gravity and eventually lead to the formation of stars and planets.

Kant's ideas may have been inspired somewhat by the work of Emanuel Swedenborg who in 1734 proposed a theory regarding the formation of our solar system (Swedenborg, 1734). Swedenborg's suggestion that the planets in our solar system gradually evolved from a belt of matter which spread from the sun is quite close to what was proposed 20 years later by Kant. A similar model was proposed independently by Simon-Pierre Laplace in 1796 though there are some differences (Laplace, 1796).

The Kant-Laplace hypothesis, as it is commonly known, remained a popular model among astronomers for another 100 years. The main problem with the model is that it failed to explain the distribution of angular momentum in our solar system which is quite uneven. It is estimated that only 1% of the angular momentum of our solar system is contained in the Sun while 98% is located in the planets although the sun contains over 99% of the mass of the solar system. The Kant-Laplace hypothesis still remains the basis of the modern theory of star formation. It is now known that star formation occurs in relatively dense clouds of gas and dust which are called molecular clouds (Shu et al., 1987), so called as almost all their hydrogen is in molecular form.

1.1 Molecular Clouds

Most of the mass in our galaxy is present in stars, yet the total volume of space taken up by the stars is quite tiny compared to the total volume of the Milky Way galaxy. However, the space in between is not an empty vacuum, but contains a low density of dust and gas.

Evidence for the existence of interstellar dust was discovered over 200 years ago, when “holes in the sky” were noticed. The reason for this lack of light emitted from certain regions of the sky was guessed at many times, but it was not until much later that it was proposed that interstellar dust was causing a scattering of star light. The suggestion of the presence of interstellar gas came earlier than that of interstellar dust. The presence was shown by studying the light coming from the area of space of interest and specifically examining the absorption lines and emission lines of the electromagnetic spectrum (Ferrière, 2001).

The gas and dust that fills interstellar space is known as the interstellar medium, this is specifically the gas and dust that is not present in stars. Typical atomic densities range from less than 10^{-3}cm^{-3} in warm and hot regions up to $10^7 - 10^{11} \text{cm}^{-3}$ in cold regions and molecular clouds.

The size of molecular clouds can vary substantially and range from small isolated clouds, called Bok globules, which measure as little as a parsec (pc) across to giant molecular clouds which can be several tens to perhaps hundreds of parsecs across and may contain as much as $10^6 M_{\odot}$ of matter (Sanders et al., 1985). Molecular clouds are not homogeneous clouds of gas and dust however and smaller scale structures have been observed to exist within, such as filaments and cores.

1.1.1 Giant Molecular Clouds

Giant molecular clouds (GMC) are the main star forming regions and are typically found in the spiral arms of our galaxy and are usually found concentrated in large complexes or spiral arm segments that can be up to a kiloparsec across and have masses of up to $10^7 M_{\odot}$. These segments can contain a number of GMC's of varying sizes, although smaller molecular clouds may



Figure 1.1: The Large Magellanic Cloud (Credit: AURA/NOAO/NSF)

also be found outside these regions (Stark and Lee, 2006). Giant molecular clouds have been observed to be inhomogeneous in structure, containing relatively dense clumps of dust and gas and rarefied regions (Williams et al., 1995). The clumps are typically a few parsecs across and contain approximately $10^3 - 10^4 M_{\odot}$. These clumps are quite cold with temperatures of 10K - 20K, and contain smaller structures called cloud cores.

The mean density of giant molecular clouds is quite difficult to determine due to the in-homogeneity and size of giant molecular clouds. The W51 cloud for example has an average H_2 volume density of 40cm^{-3} (Carpenter and Sanders, 1998) whereas one observation of the core containing the G49.5-0.4 HII region shows a mean H_2 volume density of approximately 10^4cm^{-3} over a 3 parsec region (Sievers et al., 1991).

It is also quite difficult to infer details as to the lifetime of giant molecular clouds. Blitz et al. (2007) described the evolution sequence of giant molecular clouds present within the Large Magellanic Cloud (LMC) (see Fig.1.1) by dividing it into four stages and evolutionary time-scales were inferred. It was estimated that giant molecular clouds in the LMC had an initial starless phase where no high-mass stars are to be seen, which lasts approximately

7Myrs. This is then followed by a phase, lasting 14Myrs, where there are a lot of small HII regions present indicating that the formation of several high-mass stars is under way. The next phase, lasting 6Myrs, is the most active star forming phase where many star rich clusters and HII regions are present. The final phase indicates the end of life for a typical GMC. In this phase most of the mass contained in the GMC originally is now contained in clusters. This gives a total lifetime of a typical GMC in the LMC of approximately 27Myrs.

1.1.2 Cloud Cores and Gravitational Collapse

It has been mentioned above that molecular clouds are inhomogeneous containing relatively dense or rarefied regions. The clumps and cores within molecular clouds contain a high proportion of the mass of a molecular cloud. It is believed that star formation mainly occurs within cloud cores (Larson, 2002). Cloud cores have been observed to be strong emitters of radiation. This is believed to be because of the formation of stars within them. The properties of cloud cores vary somewhat. Cold cores have been observed to have temperatures of approximately 10K and to contain roughly 1 - 10 M_{\odot} , while warm cores are considerably larger and contain roughly 10 - 1000 M_{\odot} of matter and have temperatures between 20 - 100K.

The star formation process begins when a cloud core undergoes gravitational collapse. Typically, cloud cores, and the clumps of gas and dust that surround them, are not ordinarily susceptible to gravitational collapse. Many forces, such as gas pressure, oppose the inward force of self gravity and it is only when certain conditions are met that gravitational collapse may become likely to occur. A set of criteria were first set out by Sir James Jeans (Jeans, 1902). Jeans' analysis concluded that whether or not a cloud of gas collapsed was highly dependent on the size, temperature and mass contained within this cloud.

The Jeans length is a critical length scale at which the thermal kinetic energy and gravitational potential energy are of a magnitude to allow an equilibrium of forces such that the gas cloud is neither collapsing or expanding. This may be derived easily using the virial theorem as a starting point. If the rotational forces, magnetic pressure, surface forces and any external

forces (external to the cloud) can be ignored, then the virial theorem states that the cloud will be at a state of equilibrium if the time-average total potential energy (U) is twice the time-average total thermal kinetic (K) energy contained by the cloud.

$$\langle K \rangle = - \langle U \rangle / 2 \quad (1.1)$$

Should this balance be disturbed in favour of gravitational potential energy then the cloud may collapse. To derive the Jeans Length, expressions describing the total average thermal kinetic and potential energies must be derived. To do this, it is assumed that the above energy balance is in place. It is also assumed that the cloud is a spherical cloud of particles with a uniform distribution of mass. The radius of the cloud is represented by R . Therefore the average kinetic energy of a particle is given by $\frac{3}{2}K_B T$ and the time averages are replaced by the totals.

$$\langle K \rangle = K, \quad \text{and} \quad \langle U \rangle = U \quad (1.2)$$

The total gravitational potential energy may be obtained by considering the particle cloud to consist of an infinite number of shells of thickness dr . The total gravitational energy is given by the total work required to strip all of these shells from the sphere and move them to an infinite distance from the sphere.

Since the volume of a shell may be written as $dV = 4\pi r^2 dr$, where dr is the thickness of the shell, then the mass of the gas contained in a single shell can be written as

$$m = 4\pi r^2 \rho dr \quad (1.3)$$

where ρ is the mean density of the gas.

To find the total gravitational potential energy of a self-gravitating sphere it is necessary to define what potential energy is. The definition of potential energy is given by

$$U = - \int_{s_0}^{s_1} F ds \quad (1.4)$$

where U is the work required to move an object to position s_1 from position s_0 .

The universal law of gravitation is also required and is given by

$$F_g = -G \frac{Mm}{r^2} \quad (1.5)$$

where G is the gravitational constant and M and m may be considered to be point masses and r is the distance between the point masses. This equation also holds when considering the larger mass to be a spherically symmetric body with total mass M and where r is the distance from the center of mass to the point mass m . F_g is the force of attraction between M and m .

The gravitational potential energy of the point mass m is given by

$$U = -G \int_{\infty}^r -\frac{Mm}{r^2} dr = -G \frac{Mm}{r} \quad (1.6)$$

If $M = 4/3\pi r^3 \rho$ is the total mass contained within the cloud of particles and m is the mass contained in a shell of thickness dr , then the contribution of a shell to the total gravitational potential energy of the spherical cloud is then given by

$$dU = -\frac{G(\frac{4}{3}\pi r^3 \rho)(4\pi r^2 \rho)}{r} dr = -\frac{16G\pi^2 \rho^2}{3} r^4 dr \quad (1.7)$$

To obtain the total gravitational potential energy of the system, this expression is integrated over all radii up to R to give

$$U = -\frac{16G\pi^2 \rho^2}{3} \int_0^R r^4 dr = -\frac{16G\pi^2 \rho^2 R^5}{15} \quad (1.8)$$

The total kinetic energy is given by

$$K = \frac{4\pi R^3 \rho}{3\mu} \frac{3K_B T}{2} = \frac{2\pi R^3 \rho K_B T}{\mu} \quad (1.9)$$

where μ is the mean mass per particle.

By substituting Eq. 1.8 and Eq. 1.9 into Eq. 1.1 and then solving for R an expression for the Jean's length may be obtained.

$$\lambda_J = \sqrt{\frac{15K_B T}{4\mu G \pi \rho}} \quad (1.10)$$

This expression provides a lower limit for the radius of the cloud, above which the cloud would become susceptible to gravitational collapse.

The Jeans mass may be obtained by finding the volume of a spherical cloud with a radius equal to the Jeans length and finding the mass contained within it and is given by

$$M_J = \frac{4}{3}\pi\rho\lambda_J^3 \quad (1.11)$$

This gives us an upper limit to the mass contained in a spherical gas cloud of radius λ_J . If the mass of the cloud is greater than this critical value, the cloud will be gravitationally unstable and may collapse.

One thing that is interesting to note is, if an unstable molecular cloud were in free-fall collapse, then considering a giant molecular cloud with a mass typical of those observed in the Milkyway galaxy, the free-fall time-scale would be quite short and should lead to much higher rates of star formation (Mouschovias and Spitzer Jr., 1976; Zuckerman and Palmer, 1974). Giant molecular clouds themselves are not static entities, and some net rotation is known to be present but this would be insufficient to provide enough support against gravitational collapse. On large scales, supersonic turbulence may be considered as a supporting mechanism. While supersonic turbulence may prevent the global collapse of the cloud, it does little to prevent any local gravitational collapse in cloud cores (Heitsch et al., 2000).

Magnetic fields may play an important role in the collapse of molecular clouds and may prolong the collapse through magnetic support (Crutcher, 2012).

1.1.3 Role of Magnetic Fields

Magnetic fields affect the motions of both charged and neutral particles. Charged species such as electrons, ions or charged dust particles are influenced by the Lorentz force which is proportional to the velocity of the charged species. The Lorentz force acts in a direction perpendicular to both the velocity vector of the charged particle and the direction of the magnetic field lines and is given by

$$\mathbf{F} = q\mathbf{v} \times \mathbf{B} \quad (1.12)$$

Neutral particles, in the presence of a magnetic field may move freely along and across field lines as long as no charged particles are present. If a charged species is present, then the neutral particles will be influenced by the charged species through collisional interactions as the neutral particles move across field lines.

The path of a charged particle also depends on the charge of the particle. Fig.1.2 shows the paths of two oppositely charged particles entering a magnetic field. The velocity vector in this case is perpendicular to the field lines. The particles are seen to enter a circular motion about the field lines, the radius of which is known as the Larmor radius. If a charged particle was to enter the magnetic field with a velocity vector oblique to the field lines then the velocity component parallel with the field lines will be unaffected resulting in a helical orbit. Charged particle motion becomes more complicated when the various sources of drift due to non-uniform fields and curvature in the field lines and other sources such as the electric field are taken into account.

Magnetic fields may inhibit the gravitational collapse of cloud cores. How much influence the magnetic field has on the collapse is dependent on the field strength and to some extent on the topology of the field. In the case of weak magnetic fields, magnetic pressure can easily be overcome by gravity, at least initially. As magnetic flux is accreted inwards sufficient magnetic pressure may slow collapse. In the case of strong magnetic fields, the ions and electrons are supported by the magnetic field against collapse. However, the neutrals are not directly influenced by the magnetic field but are influenced

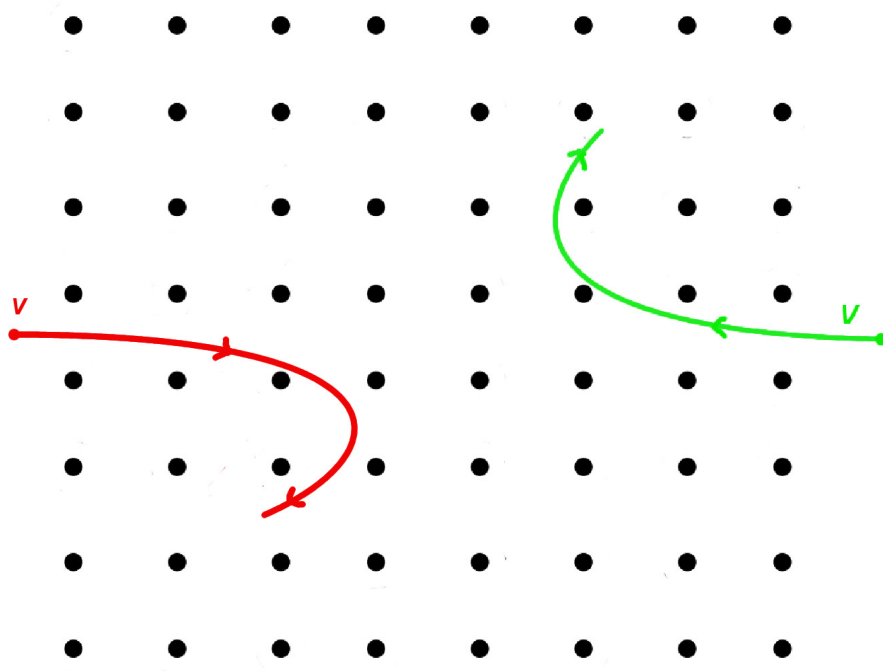


Figure 1.2: Illustration of the path of moving charged particles in the presence of a uniform magnetic field. The magnetic field lines (represented by black dots) are orientated outwards through the page. The red and green paths are the trajectories of negatively charged and positively charged particles respectively. The charged particles will then enter a circular motion about the field line.

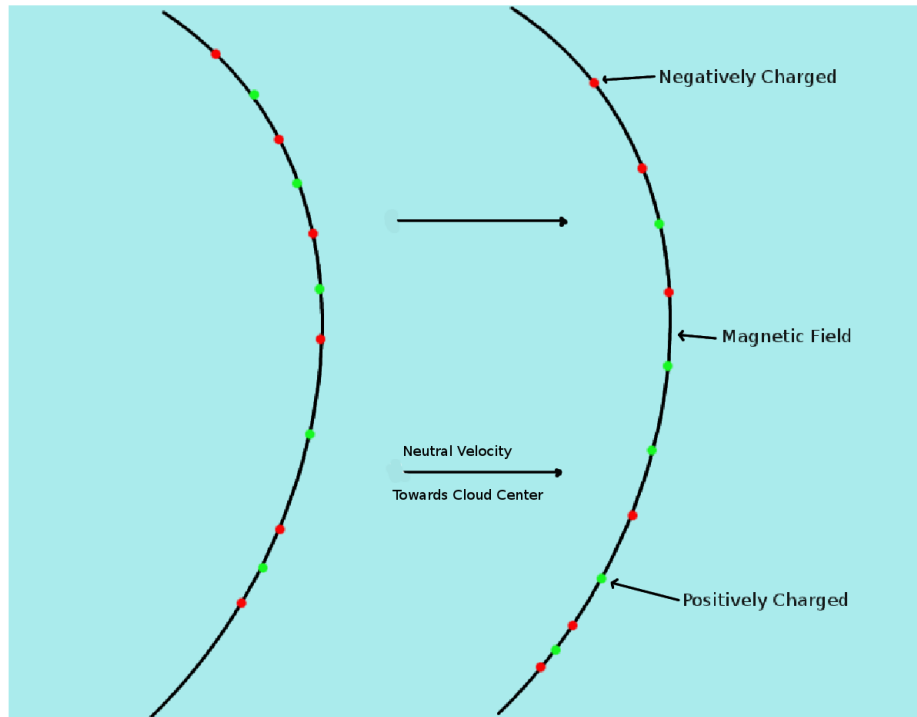


Figure 1.3: Illustration of diffusion of neutral species across the magnetic field lines. Relative to the neutral species, the ions and electrons are diffusing to the left.

indirectly through collisions with the charged species (see Fig.1.3). The neutrals are impeded from collapse by these collisions but gradually slip through while falling towards the center of gravity of the cloud. The B-field, ions and electrons diffuse outwards relative to the neutrals, this process is called ambipolar diffusion. As the mass about the center of gravity increases the gravitational attraction to the center of the core increases and may eventually overcome the thermal and magnetic pressure support. At this point the remaining mass in the core may collapse more quickly. This may then lead to the formation of an accretion disk (Shu et al., 1993, 1987). The mechanism by which this occurs will be explained in a later section (see section 1.3).

1.2 Process of Star Formation

In this section, an overview of stellar evolution is provided from the point at which the prestellar core begins to collapse across the entire evolutionary process up to joining the main sequence of stars.

Star formation can be broadly categorised into low-mass and high-mass star formation. High-mass and low-mass stars form via the same process of gravitational collapse. In high-mass star formation collapse occurs much quicker. Accretion disks may form during the formation process. High-mass stars are rare and the clouds that lead to high-mass star formation tend to be warmer, more massive and are mainly located in the spiral arms of galaxies whereas low-mass stars tend to form in cooler clouds located throughout the galactic disk. As the high-mass stars evolve faster than low-mass stars, the most massive stars can finish their life cycle while the least massive stars are still forming. The following section describes the evolution of low-mass star formation.

1.2.1 First and Second Hydrostatic cores

The first and second hydrostatic cores occur in the early stages of low-mass star formation. The first hydrostatic core is a brief phase that occurs between the initiation of gravitational collapse of the parent core and the birth of a protostar. Their existence was first proposed by Larson in 1969 (Larson, 1969).

The first hydrostatic core has not been definitively observed yet as it is contained deep within the cloud from which it evolves and so is heavily obscured by the envelope of gas and dust surrounding it. Also, the lifetime of the first core is short compared to the main accretion phase (Larson, 1969; Tomisaka and Tomida, 2011). Although, some unconfirmed candidates have been identified (Chen et al., 2010; Enoch et al., 2010). The cloud core prior to collapse typically has too much angular momentum, and the magnetic flux is usually large compared to the values seen in early main sequence stars and the first core is believed to be the point in evolution where a major redistribution of these parameters occurs (Tomisaka and Tomida, 2011).

The first core is formed during the gravitational collapse of the cloud. As collapse progresses towards the center of gravity, the density of gas and dust in this region of the cloud increases. As the in-fall continues, this region of the cloud will become opaque. Thermal radiation which is an efficient cooling mechanism in interstellar molecular gas with a number density in the range $n \sim 10^4 - 10^{10} \text{ H II cm}^{-3}$, will become inefficient at higher densities (Masunaga and Inutsuka, 2000). The temperature will begin to rise in this region rapidly resulting in an increasing thermal pressure which slows and may reach hydrostatic equilibrium and halt the gravitational collapse. This is the first core. Outside this core, material is still under gravitational collapse. It has been predicted that flat disks are formed while the first core is forming (Saigo et al., 2008), and also that bipolar outflows may also be observed during the period of the first cores existence (Tomisaka, 2002).

Once the first core forms, the continued in-fall of mass and thermal energy raises the temperature correspondingly. Once the temperature within the first core reaches an average of approximately 2000K (Larson, 1969) the hydrogen molecules (H₂) will begin to dissociate which will provide an energy sink so that the increase in thermal energy slows and collapse may now re-initiate. Once all the H₂ has been dissociated, the thermal energy no longer has a sink leading to a rapid rise in thermal pressure which again slows and halts the collapse. This is the second core (or protostellar core). The next phase is the accretion phase where matter is accreted onto the second core either by free falling on to the core or by joining the accompanying rotating accretion disk (see section 1.3 for a description of accretion disk physics).

1.2.2 Protostars

Protostars are classified depending on their evolution and are separated into four distinct classes by the slope of their spectral energy distribution (SED) (André and Montmerle, 1994) which corresponds to a decreasing mass of circumstellar material around the central object (See Fig.1.4).

Class 0 A class 0 protostar forms with the formation of the second hydrostatic core. Class 0 Protostars are cloud cores which show some evidence of containing a protostar. A class 0 protostar are also characterised by the appearance of bipolar outflows. The mass contained in the cloud core would

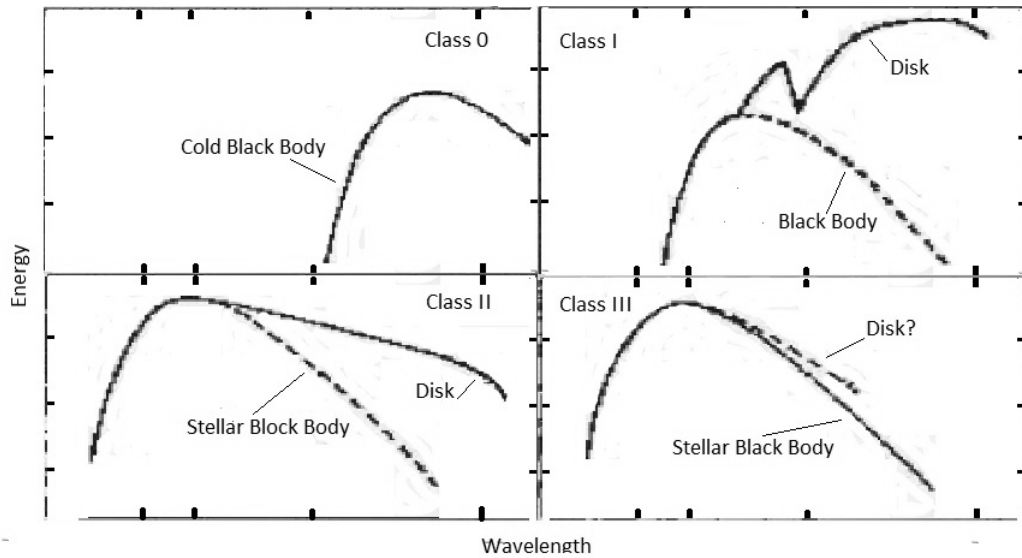


Figure 1.4: Schematic illustrating the spectral energy distribution of proto-star classes (0-III).

be much larger than the mass contained in the protostar. As the cloud collapses, the slow rotational motions are enhanced as angular momentum is conserved. Eventually, the density of the cloud core increases and becomes more opaque, the core's temperature increases as heat cannot efficiently radiate away, the protostar now enters class I (Lada, 1987). The SED of this class of protostar resembles a cold black body. The majority of the emission comes from the dust and gas in the cloud.

Class I Accretion disks are prominent features of class I protostars and the envelope of matter surrounding the protostar will have reduced somewhat by falling onto the protostar and accretion continues as the disk rotates while depositing matter onto the star. Bipolar outflows may continue through the class I & II phases but will die out once most of the material in the disk has accreted. The SED of class I protostars shows a warmer black body emission corresponding to the central object and the emission from the disk is evident.

Class II At this point of protostellar evolution, most of the material in the envelope and disk will have accreted onto the star, leaving a thin accretion disk surrounding the protostar. The luminosity is dominated by the accretion. Most of the emission is coming from the central object but there is still emission from the disk which is optically thick.

Class III Eventually, the accretion phase will end once most of the disk mass

has fallen onto the central object and the protostar will become a class III protostar. Some material may remain in the disk which may lead to planetary formation around the protostar. Planetary formation may also occur at an earlier stage. The SED will still show some emission from the remnants of the disk.

Once the mass distribution around the prestellar core has stopped contracting and has reached equilibrium the object will nearly be ready to join the main-sequence of stars. If the density and temperature of the core is high enough then the process of hydrogen fusion may begin and the star will become a zero age main sequence star (ZAMS). If the prestellar core is not hot enough, then the fusion process may not begin and the protostar will become a substellar object such as a brown dwarf.

1.2.3 High-Mass Star Formation

High-mass star formation is not very well understood compared to low-mass star formation. High-mass stars have briefer protostellar phases than low-mass stars and tend to evolve quickly compared to low-mass stars. High-mass stars are rare and therefore the closest examples are distant. They tend to form from large clouds and therefore are very deeply embedded during their early life and as they evolve so quickly compared to low-mass stars, the circumstellar disk and bipolar outflows may be destroyed by the time the star becomes observable. Another difficulty is that high-mass stars (or massive stars) rarely develop in isolation. Most high-mass stars are formed in clusters with interactions with other forming stars which makes observation difficult.

1.2.4 Main-Sequence of stars

The majority of known stars follow a mass-luminosity relationship outlined in the Hertzsprung-Russell (H-R) diagram (see Fig.1.5). The H-R diagram is a theoretical diagram which plots stellar luminosities versus the surface temperature of the stars. For main-sequence stars, luminosity (L) is a function of mass and is related approximately by a power law

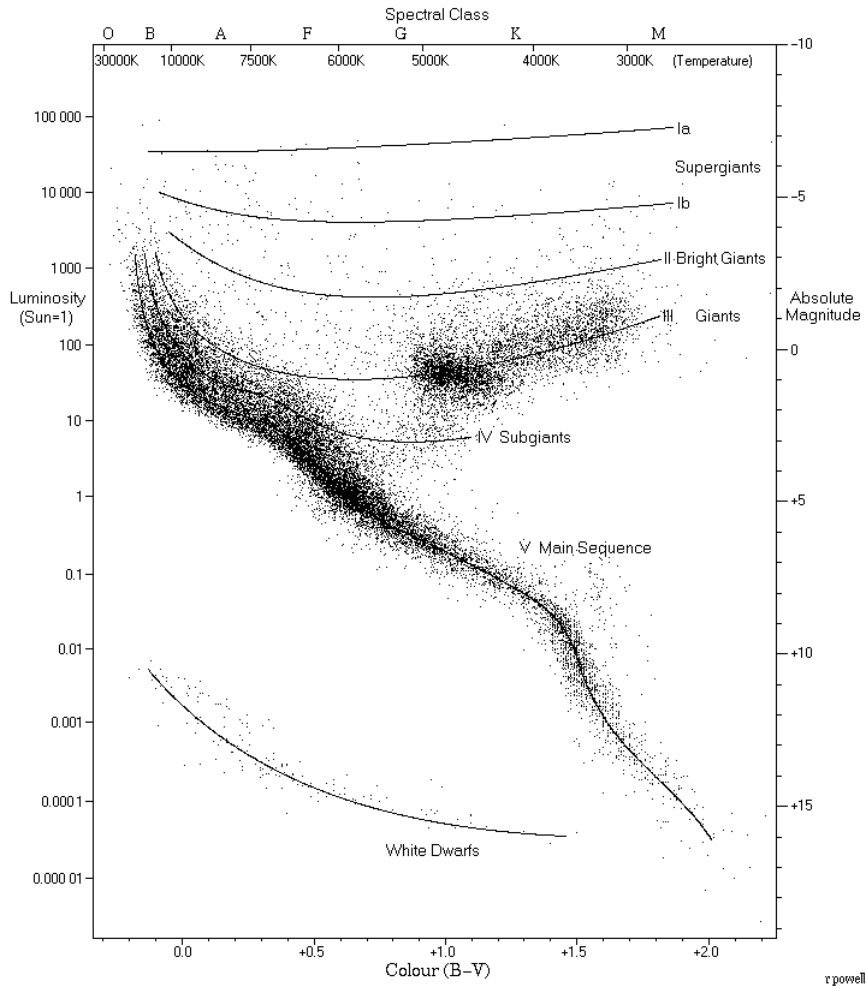


Figure 1.5: Hertzsprung-Russell diagram. A plot of luminosity (absolute magnitude) against the spectral class of the stars ranging from the high-temperature stars on the left side of the diagram to the low temperature on the right side. (Image obtained from www.atlasoftheuniverse.com)

$$\frac{L}{L_{\odot}} = \left(\frac{M}{M_{\odot}} \right)^{3.5} \quad (1.13)$$

where L_{\odot} and M_{\odot} are the luminosity and Mass of the star respectively. The properties of a given pre-main sequence star, such as final mass and temperature will determine where the star will join the main sequence curve. Once a star joins the main-sequence of stars, it remains among the main sequence for most of its life-time.

Stars such as the giants, super-giants and sub-stellar objects are not part of the main sequence of stars.

1.3 Accretion disks

Accretion disks form via a combination of gravity and rotation. Most star forming cloud cores have indeed been observed to rotate (Goodman, 1993). In the previous section, the mechanism by which a gas cloud collapsed under gravity was discussed. However, the local and global motions of the cloud were ignored for simplicity. Generally some degree of net rotation will be present in cloud cores. This net rotation will have consequences during the collapse of the cloud and may result in the formation of a disk of gas and dust which rotates and accretes upon a central mass.

Cloud cores will have some net rotation present and will have some mean plane of rotation. Once gravitational collapse is triggered and the core begins to fall in upon itself, the radial distribution of mass will change and therefore so will the angular momentum distribution within the core. As material falls inwards, the angular velocity of the material must increase to conserve angular momentum. It is the angular momentum contained within the cloud core, the thermal pressure, rate of cooling, and other processes that prevents the material from simply free falling to the center of the core. The total angular momentum about the center of gravity is given by the sum of the angular momenta of all particles (i) contained within the core

$$\mathbf{L} = \sum_i l_i \boldsymbol{\omega}_i \quad (1.14)$$

where l_i is the rotational inertia of particle i and $\boldsymbol{\omega}_i$ is the angular velocity of particle i . The rotational inertia of the particle i is given by $l_i = m_i r_i^2$. Assuming there is no momentum transfer out of the core to an ambient medium then this quantity must be conserved. If there is a contraction of the cloud core and material moves inwards, then there will be a reduction in the moment of inertia of individual particles, therefore there must be a corresponding increase in the angular velocity of those particles. A net rotation axis will exist for this collection of particles and the particles will tend to settle towards a mean plane of rotation due to self-gravity, while particles that are close to that axis of rotation but still far away from the center of mass will tend to free fall towards it (See Fig.1.6). The mean plane of rotation is the plane perpendicular to the angular momentum vector \mathbf{L} .

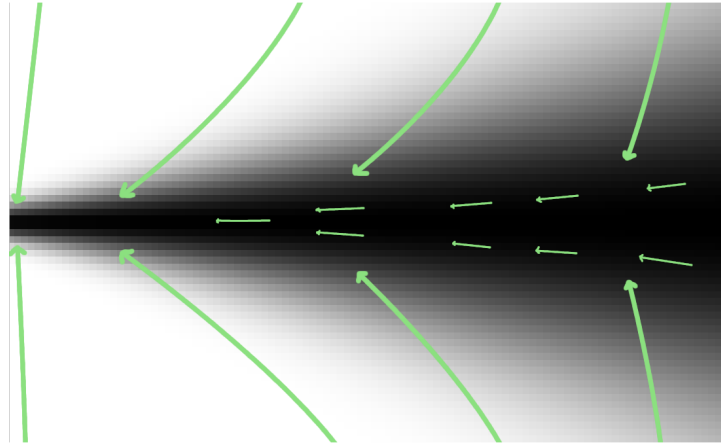


Figure 1.6: Illustration of cross-section of forming flared accretion disk(disk is rotating perpendicular to the page). Darker regions indicate higher gas densities near the mean plane of rotation. Thick lines represent the trajectory of the gas that is still part of the core and is falling onto the disk due to self-gravity. Thin lines indicate accretion.

It is through this mechanism that an accretion disk may form. The in-fall of material will slow and the majority of matter will become part of a disk structure and the infall rate will converge to an approximately constant value Larson (2003). At this point the central object has become a protostar of low but increasing mass with the rotating disk situated within what remains of the cloud core which is still falling towards the protostar.

The accretion disk structure around a young star will be of a differentially rotating cloud of gas and dust which will be geometrically thin in the vertical direction (perpendicular to the plane of rotation). Such a disk will be in approximate Keplerian rotation about the star, where the rotation profile is determined mainly by the gravitational potential of the central object. Rotation, thermal pressure and magnetic fields will support the disk against collapse. The structure of the disk is determined by the disk temperature, which can be related to the accretion luminosity, which is the maximum power that can be generated from material falling onto the central object. The disk is expected to be more dense towards the midplane because of self gravity.

One of the prominent features of these systems is bipolar outflows (see Fig.1.7). These outflows may appear in the form of highly collimated jets of material which have very high velocities or in the form of molecular outflows which are considerably slower and not as collimated. Bipolar outflows are one mechanism through which a protostellar disk may lose its mass (and momentum) through a process other than accretion (Sheikhnezami et al., 2012). The typical radius of the accretion disk varies widely and is directly proportional to the total mass contained in the original cloud core. A typical accretion disk radius is of the order of 100 - 1000 AU (Visier, 05-09-2012).

Estimations regarding the life-time of accretion disks are variable. The time taken for the accretion disk within 1 AU to go from being optically thick to being optically thin was estimated to be approximately 10^5 years (Skrutskie et al., 1990; Wolk and Walter, 1996). Another study argued that the accretion phase terminates 10^6 years after initial collapse of the cloud core (Haisch et al., 2001). It has also been suggested that in some cases, the accretion phase may last up to and beyond 10^7 years (Lawson et al., 2004; Mamajek et al., 2002; Muzerolle et al., 2000).

Estimates of the rate at which material accretes onto the central object have been calculated by for instance, assuming that in the class 0 and class 1 phases, the luminosity due to accretion dominates the entire radiative output from the star disk system (Enoch et al., 2009). Another method, which is useful especially in the case of class II protostars, is that used by Gullbring et al. (1998) where data from flux-calibrated spectra which is used to derive the excess hot continuum emission produced by accretion onto the central object. The accretion rate can be useful in determining what physical processes are likely to be active in the disk and contributing to the accretion rate. Much of the theoretical research into accretion disks in recent years has been concerned with the study of the various accretion mechanisms involved which will be discussed in the next subsection.

1.3.1 Accretion Mechanisms

For a fluid element within an accretion disk to fall inwards towards the central object, it must lose some angular momentum somehow. The principle of conservation of angular momentum tells us that the momentum lost must be

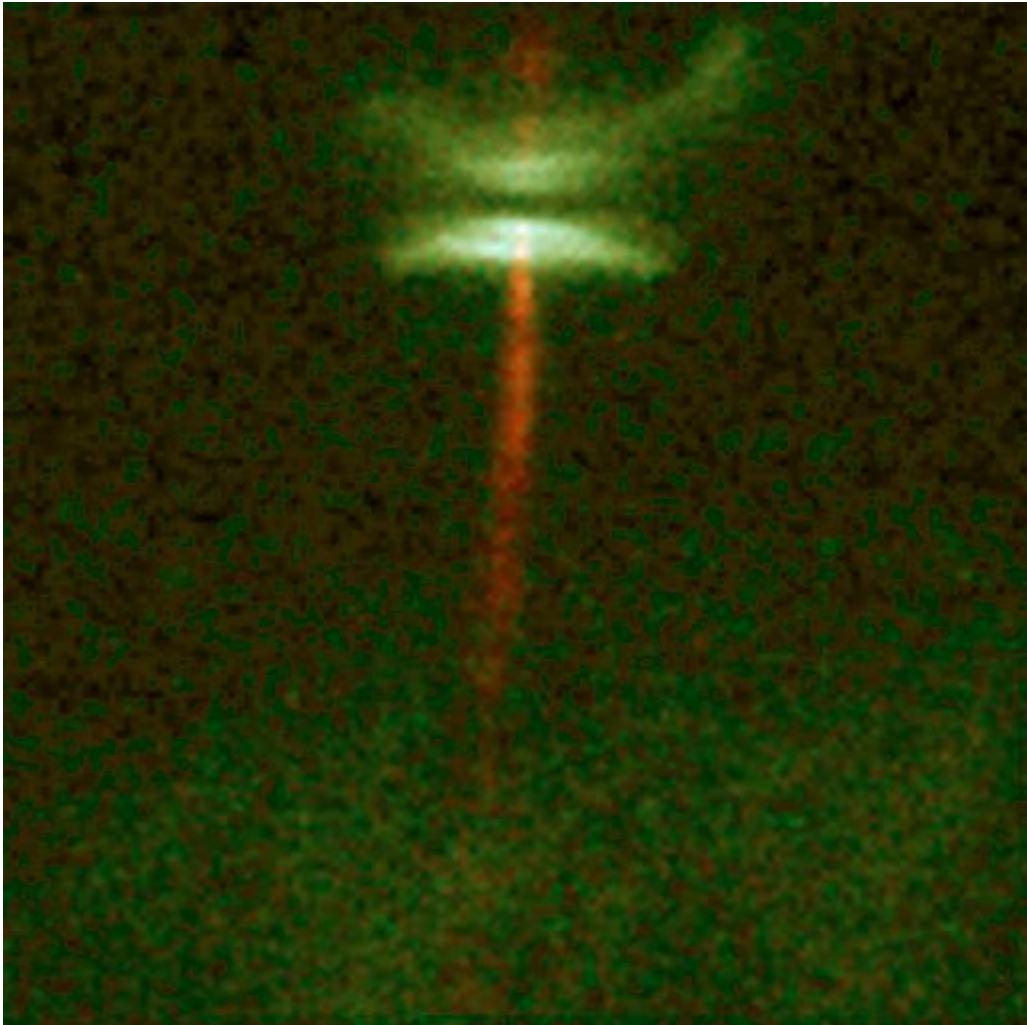


Figure 1.7: Image of HH30, a young star/disk system showing bipolar outflows being launched from a dusty accretion disk. The disk is edge on and the central object is hidden from view but light from the young star is illuminating the disk material nearby.(Credit: WFPC2 Science Team and NASA/ESA)

transferred elsewhere and cannot simply disappear. Therefore some material will lose angular momentum, and some will gain angular momentum. The accretion rate therefore has an influence on the disk structure and the long term evolution of the disk. If the global situation is considered, it becomes obvious that for the accretion disk to continue to deposit its matter upon the central object and for the net inflow of mass to be sustained, the net angular momentum transport must be away from the central object. The question of what mechanism (or mechanisms) is responsible for this transport is one that has been studied in great detail in recent times and is still very much an open question (Balbus and Hawley (1998); Pringle (1981); Stone (2011) and references therein).

In observations, accretion rates have been estimated to be approximately $10^{-7} - 10^{-9} M_{\odot}$ per year (Gullbring et al., 1998) and a mean rate of roughly $10^{-8} M_{\odot}$ for protostellar disk systems of 1Myr age was determined for protostars of roughly solar mass. Using observations and computational simulations, a comparison can be made between the accretion rates calculated from observational data and the estimated accretion rate obtained by computational simulations of different accretion processes to try and extract information about the dominance of any one or combination of processes. A short summary of some processes believed to be active in accretion disks and their effectiveness in transporting angular momentum follows.

Molecular viscosity is an obvious candidate to consider as the main process responsible for the observed accretion rate as accretion disks are quite dense relative to the surrounding envelope. As accretion disks are differentially rotating objects the inherent shear naturally leads to viscous heating. Molecular viscosity converts the shear motion of the gas into heat through friction. The heat produced by the friction may then be radiated away in the region where it is produced or it is advected inward with the accreting dust and gas. The viscous torques associated with differential rotation are responsible for the transport of angular momentum from neighbouring annuli where the inner annulus has a higher angular velocity.

However it has been shown that the dissipative (viscous) and emission processes associated with viscosity can't solely be responsible for the observed accretion rates (Pringle, 1981). Given the length scales involved with protostellar disks, the molecular viscosity would be much too small to be

responsible for such rates of mass inflow.

The Reynolds number, which gives an indication of the relative importance of inertial or viscous effects in a flow. It is defined by

$$R_e = \frac{VL}{\nu} \quad (1.15)$$

where V is the mean velocity of the fluid, L is the characteristic length scale of the flow and ν is the kinematic viscosity. This dimensionless number is large in accretion disks due to the large length scales and velocities involved and the low viscosity. Typical Reynolds numbers occurring in real accretion disks may be larger than 10^6 (Bonanno and Urpin, 2008). High Reynolds numbers are typically associated with turbulent flows, while low Reynolds numbers are associated with laminar flows. A low Reynolds number suggests that inertial forces are similar or smaller than viscous forces and any disturbances to the flow may be damped by viscosity. As the Reynolds number of a flow increases the effectiveness of viscous damping decreases and disturbances may grow over time and may lead to instability and turbulence. It is known that turbulent eddies can indeed give rise to significant angular momentum transfer.

Another source for hydrodynamic instability is **convective turbulence** caused by viscous heating and cooling in accretion disks. Accretion disks do have some vertical structure and stratification and convective turbulence has been examined to ascertain whether sufficient turbulence is generated by this process to provide sufficient angular momentum transport to allow the high accretion rates encountered. Convection is a local process by which surface cooling may lead to a vertical temperature gradient in a self-gravitating disk thus causing convection currents and turbulence (Stone and Balbus, 1996).

A number of quasi-local hydrodynamic simulations of this process have been performed. In this approach only a small patch of the disk is simulated and boundary conditions that are appropriate to the shearing nature of the disk are used. A significant portion of the vertical structure is included in the computational domain. Although in most cases a very small range of initial thermal temperature gradients were used, it has been shown that the net angular momentum transport can be inwards as well as outwards, although long term time averages show that the net transport is inward in

all cases studied and small. Also it was found that the turbulence was not self-sustaining (Stone and Balbus, 1996).

Tidal forces caused by the uneven distribution of mass in the rotating disk about the star have also been considered (Goodman et al., 1993) but have not supplied any evidence of contributing greatly to angular momentum transport.

The **baroclinic instability** was suggested as an efficient transport mechanism of angular momentum by Klahr and Bodenheimer (2003) which arises because of the radial stratification of accretion disks. It occurs naturally in rotational shear flows when surfaces of constant density are inclined versus surfaces of constant pressure. In the simulations performed the instability proved to be quite effective.

Gravitational instabilities of a self-gravitating disk (Toomre, 1964) may also lead to turbulence in the disk and contributing to the outward angular momentum transport. Bipolar outflows which are prominent features of protostellar disks is also an efficient mechanism for the removal of angular momentum.

The effect of magnetic fields have been largely ignored thus far in this discussion. It is known that accretion disks and protostars are typically magnetised. Although the effect the magnetic field might have on the evolution of accretion disks was mentioned in a few works in the late 60's and early 70's (Lynden-Bell, 1969; Shakura and Sunyaev, 1973), very little progress was made until 1991 when it was suggested that the presence of a weak magnetic field in a differentially rotating fluid, such as an accretion disk, led to a powerful instability capable of generating turbulence and more importantly, sustaining it. This instability is the magnetorotational instability (Balbus and Hawley, 1991). It must be noted that the effect of magnetic fields on plasmas in shear flow had been studied in a non-astrophysical context by Velikhov (1959) and Chandrasekhar (1960).

The **magnetorotational instability** is a local instability acting over relatively small length scales compared to the disk radius and was shown to be very effective in transferring angular momentum. For the magnetorotational instability (MRI) to be active, all that it required is a differentially rotating body with a weak embedded magnetic field. The instability is mediated by

the magnetic tension existing between nearby fluid elements which leads to angular momentum being transported outwards radially (Balbus and Hawley, 1991) thereby affecting the rate of accretion.

In any rotating, weakly magnetised system, the MRI will be an important process to consider. As the instability occurs on very small length scales, it makes it difficult to perform meaningful simulations demonstrating the process. This is largely due to the computational cost of applying a suitably sized grid structure to an accretion disk. Local simulations have been used extensively to study the instability due to the lesser computational cost. However, recently global studies are emerging due to the greater availability of computational resources. This instability will be explained in greater detail in section 1.4.

1.4 The Magnetorotational Instability

Accretion disks are expected to be stable if they are considered to be governed by the hydrodynamic equations of motion and generally satisfy the Rayleigh stability criterion,

$$\frac{d}{dR}(R^2\Omega)^2 > 0 \quad (1.16)$$

It has already been stated that hydrodynamic instabilities such as convective turbulence do not typically result in significant angular momentum transport. So what processes are responsible for the angular momentum transfer expected for significant accretion flow?

Turbulence is known to be an efficient transport medium for angular momentum, but requires an instability to produce, grow and sustain itself in an accretion disk. It is known that accretion disks and other astrophysical objects are at least partially ionised and that magnetic fields may play a role in their evolution (Ilgner and Nelson, 2006a,b).

The magnetorotational instability (MRI) was first considered in a non-astrophysical context in 1959 by E. Velikhov (Velikhov, 1959) whilst studying the stability of an ideal magnetised fluid under the conditions of Couette flow. Velikhov's results were later generalised in a paper written a year later by S.Chandrasekhar (1960).

In the following years, with the exception of a body of work by Klaus Fricke in 1969 (Fricke, 1969), very little work was done to advance the understanding of the MRI. This lack of progress continued until Balbus and Hawley (1991) proposed that magnetic fields played an important role in the accretion stage of star formation and suggested that the MRI could be responsible for the discrepancy between observed and calculated accretion rates and could create and sustain turbulent flows on quite small scales compared to the disk size.

1.4.1 Simplified description of the MRI

Consider a geometrically thin accretion disk of fluid in the ideal MHD approximation which is threaded by a weak vertical (normal to the plane of the disk) magnetic field. The instability is due to the shearing nature of the fluid motion in the disk which is caused by differential rotation.

Fig.1.8 shows two neighbouring fluid elements rotating around a central mass, where m_i is the inner most fluid element, m_o is the outer most fluid element and M_c is the central mass. We assume

$$M_c \gg m_i m_o \tag{1.17}$$

We can therefore neglect the gravitational force that exists between m_o and m_i and only consider the gravitational attraction between the two fluid elements and the central mass.

In Fig.1.8 the springs between the fluid elements are representative of the magnetic tension that exists between them.

As dynamical evolution takes place, because the disk is differentially rotating, the inner most fluid element m_i will have a higher angular velocity than the outer most fluid element m_o and so the distance between the two elements will increase.

As the distance separating the two elements increases, the magnetic tension between m_o and m_i will increase. This tension tends to cause m_o to accelerate rotationally and m_i to decelerate in a similar manner. The outer element will therefore tend toward a higher orbit around the central mass. Likewise the inner element will tend to fall inwards radially to a lower orbit around the central mass.

As the two fluid masses move away from each other, the magnetic tension between the two fluid elements continues to increase and may lead to a run away process.

In this process angular momentum is transported from the inner element to the outer element continuously. If one imagines this on the global scale of the disk, this process has the potential of transporting large amounts of

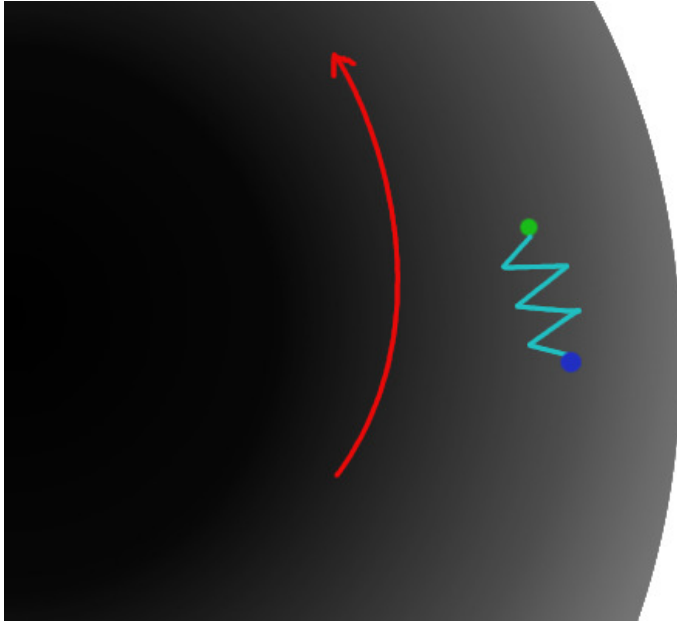


Figure 1.8: Diagram illustrating the MRI process. Red arrow describes direction of accretion disk rotation. The green and blue solid dots represent the inner and outer fluid elements respectively and the turquoise spring represents the magnetic tension between the fluid elements.

angular momentum radially outwards along the disk. For material to accrete inwards radially, it is necessary for angular momentum to be transported outwards.

1.4.2 Growth and Saturation of the instability.

In an accretion disk, the effect of the shear flow on an embedded magnetic field is to stretch and tangle the magnetic field which leads to dynamo amplification of the field. As the field strength increases, the strength of angular momentum transport increases proportionally. From a linear analysis performed by Balbus and Hawley (1991) the MRI may result in a factor of 10^4 amplification in the total energy per orbit (Balbus and Hawley, 1998).

However, the linear stage of the MRI where growth occurs must eventually transition to the non-linear stage where the MRI becomes saturated. It is believed that buoyancy and dissipation and the principal processes that lead to the eventual saturation of the MRI.

Once magnetic pressure becomes comparable to gas pressure, this can

lead to field expulsion through magnetic buoyancy effects. The vertical velocities associated with magnetic buoyancy are believed to be quite small and when these are compared to the height scale of the disk, it seems likely that the magnetic field losses will be small (Stone et al., 1996). It is likely that a balancing of magnetic field generation and dissipative losses is a determinant of the saturation level (Balbus and Hawley, 1998).

1.4.3 Channel Solutions

One strange and unexpected result from early simulations of the MRI was the appearance of counterflowing channel (streaming) solutions. In local 2D simulations, they are seen to be two exponentially growing inward flowing and outward flowing streams of matter on the largest available length scale. The presence of any mean vertical field, regardless of geometry will eventually lead to these solutions forming. However once the mean magnetic field taken over the grid nears zero, the channel solution breaks down into turbulence (Balbus and Hawley, 1998) This turbulence does not persist however due to the anti-dynamo theorem, this is due to the fact that any sort of sustained turbulence in an isolated dissipative system is impossible (Moffat 1979). In simulations, the turbulence does not die out completely however as simulated disks are typically not closed systems.

Channel solutions are considered to be exact, exponentially growing, solutions of the incompressible shearing box equations and are subject to parasitic instabilities. In local 3D simulations, the same conditions apply. The Channel solution is itself unstable to secondary parasitic instabilities such as the Kelvin-Helmholtz instability which can cause these solutions to break up. However the channel solutions may reform and break up periodically. It is ultimately large wavelength modes of these secondary instabilities that are much larger than the vertical wavelength of the channel solution that cause the breakup (Simon et al., 2009). It has been seen in simulations that if the aspect ratio of the box is made sufficiently large the channel solution no longer occurs. This was observed by Bodo et al. (2008). This is most likely because very large wavelength modes of these secondary instabilities are present and stop the channel solution from forming in the first place.

In fully global simulations with vertical gravity gradient, the consequence

of the channel solution is avalanche accretion as seen in Matsumoto and Shibata (1997). In this paper, a 3D accretion torus was initialised and a vertical gravity dependence was allowed. The surface of the disk underwent dramatic accretion while being fed more material from within the disk. This is the non-linear manifestation of the channel solution which is also known as the vertical field instability. What the results of Bodo et al. (2008) mean for the global manifestation of the channel solution is not certain. Formation of the channel solution in global disks has been found in the accretion tori simulations of Hawley (2000). It may be possible that the results of Bodo et al. (2008) may only be applicable to the shearing box model. No direct comparison between the local and global manifestation of the channel flow exists currently.

In the case without a vertical gravity gradient, if the right conditions exist, large Reynolds stress fluctuations and impulsive accretion is seen. A structured radial flow is seen upon non-linear saturation. This is the channel flow. The fastest growing modes have a finite vertical wavenumber and a vanishing radial wavenumber. These can easily be disrupted by turbulence however (Hawley, 2001).

Chapter 2

Magnetohydrodynamics

The laws of magnetism applied to electrically conducting fluids, known as magnetohydrodynamics (MHD), is a relatively new area of science. The interaction between fluids, such as plasmas and magnetic fields has been known and theorised about for almost as long as the laws of magnetism themselves. For example, in 1832, Michael Faraday tried to measure the potential difference between the two banks of the river Thames which was induced by the movement of the salty Thames water through the Earth's magnetic field. His measuring equipment was not sensitive enough however.

Later, geophysicists theorised about how the magnetic field of the Earth and the Sun was generated. It was thought that the earth's magnetic field was generated by dynamo action occurring through the movements of the liquid metal of the earth's core. This idea was first proposed by Joseph Larmor in the context of the Sun (Larmor, 1919).

Hannes Alfvén is credited with the first recorded use of the word magnetohydrodynamics and made many advances in the field of MHD such as the discovery of what became known as the Alfvén wave in 1942. This phenomenon is where a magnetic field line can transmit waves much like a string under tension (Alfvén, 1942).

Numerical simulations are widely used to study MHD in the context of astrophysics. A large number of astrophysical phenomena may be studied using numerical simulations over a wide range of time-scales and length scales. The detail with which such problems may be studied is rarely limited by the

algorithms available, but is rather limited by the computational resources available. Global simulations of large objects such as accretion disks, where the evolution may be heavily determined by processes with relatively small length scales can be very computationally intensive.

2.1 MHD models

The use of certain MHD regimes to model various astrophysical phenomena also depends largely upon the length and time scales involved. Each regime has a region of applicability, assumptions, and various pros and cons. Although there may be some overlap with regards to the region of applicability, it is important to choose the most suitable regime for the problem at hand. The common models along with their implicit assumptions will now be described briefly.

The equations of MHD consist of the hydrodynamical transport equations and an induction equation describing the magnetic field. This induction equation is a combination of the Maxwell equations, the four fundamental equations governing electromagnetism (Eq.2.1 - Eq.2.4), and the generalised Ohm's law. Depending on the assumptions made during the derivation, one may end up with various models each with an applicability to different situations.

The following equations are Maxwell's equations in *cgs* units and defined in terms of total charge and current,

$$\nabla \cdot \mathbf{E} = \frac{\rho}{\epsilon_0} \quad (2.1)$$

$$\nabla \cdot \mathbf{B} = 0 \quad (2.2)$$

$$\nabla \times \mathbf{E} = -\frac{\partial \mathbf{B}}{\partial t} \quad (2.3)$$

$$\nabla \times \mathbf{B} = \mathbf{J} + \frac{\partial \mathbf{E}}{\partial t} \quad (2.4)$$

where ρ is total charge density and ϵ_0 is the permeability of free space. The symbols \mathbf{E} and \mathbf{B} represent the electric and magnetic flux density respectively and \mathbf{J} represents the total current density. The equations are individually known as Gauss' law for electricity, Gauss' law for magnetism, Faraday's law of induction and Ampere's law respectively.

In early numerical studies of accretion disk evolution, **ideal MHD** was commonly used. This is the simplest MHD model, where the ionised fluid is approximated by a single fluid. Ideal MHD is only applicable under certain conditions which are assumed in the derivation. It is assumed that the plasma is non-relativistic (i.e. $\mathbf{u} \ll c$) and so the displacement current in Ampere's law (Eq.2.4) may be ignored so that:

$$\nabla \times \mathbf{B} = \mathbf{J} \quad (2.5)$$

It is also assumed that quasi-neutrality holds.

$$\sum_{i=2}^n \alpha_i \rho_i = 0 \quad (2.6)$$

where α_i is the charge to mass ratio of the charged fluid i .

The single fluid approximation leads to a single set of evolution equations that are used to describe the neutral and ionised fluids together and represent them as one bulk fluid. This assumption is only valid where the plasma is strongly collisional. The length scale of interest must be much longer than the mean free path of any particle. The ideal MHD approximation is valid when the resistivity of the plasma is negligible.

The magnetic Reynolds number (R_m) is a dimensionless number that is analogous to the Reynolds number of hydrodynamics. It is given by

$$R_m = \frac{\mu_0 V L}{\nu} \quad (2.7)$$

where μ_0 is the magnetic permeability of free space, V is the plasma velocity, L is a characteristic length scale of the plasma structure and ν is the resistivity of the fluid.

When $R_m \gg 1$ the magnetic field lines are effectively tied to the fluid and when $R_m \ll 1$ diffusion of the magnetic field becomes important. In ideal MHD, the magnetic Reynolds number become infinite as the resistivity becomes negligible. This is achieved when the length scales being studied are much larger than any diffusive length scales. The ideal MHD equations will now be derived.

Ohm's law is given by

$$\mathbf{J} = \frac{1}{\eta} \mathbf{E}' = \frac{1}{\eta} (\mathbf{E} + \mathbf{v} \times \mathbf{B}) \quad (2.8)$$

where \mathbf{E}' is the electric field in the frame of a fluid element moving with velocity \mathbf{v} , and η is the scalar resistivity which assumes that $\nabla \eta = 0$.

By substituting (Eq.2.5) for the current in (Eq.2.8), the following equation for the electric field may be obtained:

$$\mathbf{E} = \eta \nabla \times \mathbf{B} - \mathbf{v} \times \mathbf{B} \quad (2.9)$$

This expression for the electric field may be substituted into Faraday's law of induction to give the induction equation

$$\frac{\partial \mathbf{B}}{\partial t} = -\eta \nabla \times (\nabla \times \mathbf{B}) + \nabla \times (\mathbf{v} \times \mathbf{B}) \quad (2.10)$$

Using the vector identity $\nabla^2 \mathbf{B} = \nabla(\nabla \cdot \mathbf{B}) - \nabla \times (\nabla \times \mathbf{B})$ and using the fact that the divergence of the magnetic field is assumed to be zero then (Eq.2.10) may be written as

$$\frac{\partial \mathbf{B}}{\partial t} = \eta \nabla^2 \mathbf{B} + \nabla \times (\mathbf{v} \times \mathbf{B}) \quad (2.11)$$

Finally, the ideal induction equation may be obtained by using the assumption that the fluid is perfectly conducting to give

$$\frac{\partial \mathbf{B}}{\partial t} = \nabla \times (\mathbf{v} \times \mathbf{B}) \quad (2.12)$$

The evolution of the magnetic field is determined by this equation along

with Gauss' law for magnetism (Eq.2.2). Notice that in the above induction equation, the right hand side only contains an advective term. There is no diffusion allowed for in this equation. The magnetic field is effectively tied to the fluid as described by the '*frozen in theorem*' also known as Alfvén's theorem. Alfvén's theorem states that in a perfectly conducting fluid, the magnetic field is frozen into the plasma and is transported with the flow (Alfvén, 1942). To show this, it is first necessary to define Gauss's divergence theorem:

$$\int_V \nabla \cdot \mathbf{A} dV = \int_S \mathbf{A} \cdot \hat{\mathbf{n}} dS \quad (2.13)$$

where \mathbf{n} is the outward normal vector to the closed surface S . By applying this to (Eq.2.2) to get,

$$\int_V \nabla \cdot \mathbf{B} dV = \int_S \mathbf{B} \cdot \mathbf{n} dS = 0 \quad (2.14)$$

it can be seen that the magnetic flux through any *closed* surface S must be zero. The magnetic flux through any *open* surface may vary with time.

The magnetic flux through a closed loop of fluid elements, l , is given by $\Phi = \int_l \mathbf{B} \cdot \mathbf{n} dS$. The closed loop is shown in Fig.2.1 at two instants in time, $l(t)$ and $l(t + dt)$. This defines three surfaces that make up the closed surface S , the bottom surface (S_1), the top surface (S_2), and a quasi-cylindrical surface (S_3) defined by the loop (l) as the contained fluid elements move through space over the time interval defined by dt .

Using (Eq.2.14), the magnetic flux through the close surface S is written as

$$\int_S \mathbf{B}(t+dt) \cdot \mathbf{n} dS = - \int_{S_1} \mathbf{B}(t+dt) \cdot \mathbf{n} dS + \int_{S_2} \mathbf{B}(t+dt) \cdot \mathbf{n} dS + \int_{S_3} \mathbf{B}(t+dt) \cdot \mathbf{n} dS = 0 \quad (2.15)$$

where the minus sign comes from the inward flux through surface S_1 .

Consider the quasi-cylindrical surface, S_3 . The flux through this surface at time $t + dt$ is given by $\int_{S_3} \mathbf{B} \cdot \mathbf{n} dS$. Notice that $\mathbf{n} dS \approx dl \times \mathbf{v} dt$ so that

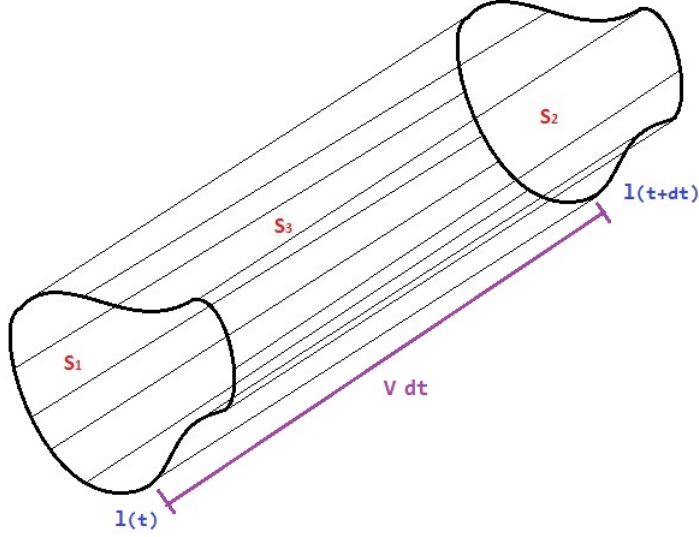


Figure 2.1: Illustration accompanying flux-freezing description in text.

$$\begin{aligned}
 \int_{S_3} \mathbf{B}(t + dt) \cdot \mathbf{n} dS &= \oint_l \mathbf{B}(t + dt) \cdot (dl \times v dt). \\
 &= dt \oint_l \mathbf{B}(t + dt) \cdot (dl \times v). \\
 &= dt \oint_l (\mathbf{v} \times \mathbf{B}(t + dt)) \cdot dl
 \end{aligned} \tag{2.16}$$

How the magnetic flux changes in time is given by the difference in Φ at $t + dt$ and t ,

$$d\Phi = \int_{S_2} \mathbf{B}(t + dt) \cdot \mathbf{n} dS - \int_{S_1} \mathbf{B}(t) \cdot \mathbf{n} dS \tag{2.17}$$

Then using (Eq.2.15) the following expression for $d\Phi$ can be obtained by substitution

$$\begin{aligned}
d\Phi &= \int_{S_1} \mathbf{B}(t+dt) \cdot \mathbf{ndS} - \int_{S_1} \mathbf{B}(t) \cdot \mathbf{ndS} \\
&\quad - dt \oint_l (\mathbf{v} \times \mathbf{B}(t+dt)) \cdot d\mathbf{l}
\end{aligned} \tag{2.18}$$

The first two terms may be grouped together to give

$$\begin{aligned}
d\Phi &= \int_{S_1} [\mathbf{B}(t+dt) - \mathbf{B}(t)] \cdot \mathbf{ndS} \\
&\quad - dt \oint_l (\mathbf{v} \times \mathbf{B}(t+dt)) \cdot d\mathbf{l}
\end{aligned} \tag{2.19}$$

As long as dt is small so that the magnetic flux does not change appreciably during that period then $d\Phi$ may be written as

$$\frac{d\Phi}{dt} = \int_{S_1} \frac{\partial \mathbf{B}}{\partial t} \cdot \mathbf{ndS} - \oint_l (\mathbf{v} \times \mathbf{B}) \cdot d\mathbf{l} \tag{2.20}$$

Stokes theorem is now applied to the second term RHS of (Eq.2.20) so that

$$\oint_l (\mathbf{v} \times \mathbf{B}) \cdot d\mathbf{l} = \int_{S_1} \nabla \times (\mathbf{v} \times \mathbf{B}) \cdot \mathbf{ndS} \tag{2.21}$$

Finally by substituting this back into (Eq.2.20) we get

$$\begin{aligned}
\frac{d\Phi}{dt} &= \int_{S_1} \frac{\partial \mathbf{B}}{\partial t} \cdot \mathbf{ndS} - \int_{S_1} \nabla \times (\mathbf{v} \times \mathbf{B}) \cdot \mathbf{ndS} \\
&= \int_{S_1} \left[\frac{\partial \mathbf{B}}{\partial t} - \nabla \times (\mathbf{v} \times \mathbf{B}) \right] \cdot \mathbf{ndS} \\
&= 0
\end{aligned} \tag{2.22}$$

Physically, this means that any fluid contained within a flux tube remains within it even as the fluid is deformed by motion.

The remaining equations of ideal MHD are the hydrodynamic fluid equa-

tions with additional terms to take into account of the effect of the magnetic field on the plasma. Now that the evolution of the magnetic field is known, the evolution of the plasma itself will be examined. The following equation is the equation of an ideal neutral fluid for momentum conservation:

$$\rho \left(\frac{\partial \mathbf{v}}{\partial t} + \mathbf{v} \cdot \nabla \right) = -\nabla P \quad (2.23)$$

The only source term in the momentum equation is given by the pressure gradient. A plasma in the presence of a magnetic field cannot be described by this equation as is. It is known that magnetic and electric fields affect the motions of a plasma through a force known as the Lorentz force. The force on a single charged particle with charge q moving through a magnetic field \mathbf{B} with a velocity \mathbf{v} is given by

$$\mathbf{F} = q(\mathbf{E} + \mathbf{v} \times \mathbf{B}) \quad (2.24)$$

The electric force may be safely ignored as the electric force is much smaller than the magnetic force for quasi-neutral plasmas. This gives

$$\mathbf{F}_m = q\mathbf{v} \times \mathbf{B} = \mathbf{J} \times \mathbf{B} \quad (2.25)$$

By substituting Ampere's law (Eq.2.4) into the above equation, the Lorentz force may be written in terms of conserved quantities.

$$\mathbf{F}_m = (\nabla \times \mathbf{B}) \times \mathbf{B} \quad (2.26)$$

This now becomes a source term for the momentum equation (Eq.2.23) to give the ideal MHD equation for momentum conservation:

$$\rho \left(\frac{\partial \mathbf{v}}{\partial t} + \mathbf{v} \cdot \nabla \right) = -\nabla P + (\nabla \times \mathbf{B}) \times \mathbf{B} \quad (2.27)$$

Mass conservation must now be considered. Mass conservation of a plasma is not affected by an applied magnetic field so this equation is identical to the hydrodynamic case and is given by:

$$\frac{\partial \rho}{\partial t} + \nabla \cdot (\rho \mathbf{v}) = 0 \quad (2.28)$$

Finally, the total energy of the system must be conserved. Assuming an ideal gas law, the energy equation is of the form

$$\frac{\partial \rho \epsilon}{\partial t} + \nabla \cdot (\rho \epsilon \mathbf{v}) + (\gamma \rho \epsilon \nabla \cdot \mathbf{v}) = -S \quad (2.29)$$

where ϵ is the internal energy, γ is the adiabatic index, and the S on the RHS is the sum of all the sinks and sources for energy such as radiative losses and magnetic energy losses for example.

If the model required is needed to study a plasma at length scales at which magnetic diffusion may become an important process and thus a finite magnetic Reynolds number may be considered important. In this case a scalar resistivity or a variable resistivity determined by some simplified model may be used. The consequence of this is that an extra term must be added to the induction equation to take into account this diffusion. This model is known as **resistive MHD**.

By substituting the unmodified Ohm's law (Eq.2.3) into Faraday's law, the following equation is obtained:

$$\frac{\partial \mathbf{B}}{\partial t} = -\nabla \times (\eta \mathbf{J} - (\mathbf{v} \times \mathbf{B})) \quad (2.30)$$

where μ is the magnetic permeability of the fluid.

Equation 2.30 may be simplified with the assumption that $\nabla \eta = 0$ to give

$$\frac{\partial \mathbf{B}}{\partial t} = -\eta \nabla \times \mathbf{J} + \nabla \times (\mathbf{v} \times \mathbf{B}) \quad (2.31)$$

and by substituting for the current density using equation Eq.2.5 and after some simplification, the following induction equation may be obtained:

$$\frac{\partial \mathbf{B}}{\partial t} = \nabla \times (\mathbf{v} \times \mathbf{B}) + \eta \nabla^2 \mathbf{B} \quad (2.32)$$

It may be observed when comparing the above equation to the ideal induction equation that the same advective term is present but now with an additional diffusive term. This diffusion term describes the effect of magnetic diffusion due to collisions. The magnetic Reynolds number is now finite which means that the magnetic field is no longer frozen into the plasma. The resistivity is no longer negligible, and it is determined by a number of physical processes. Note also that, a term should be included in the energy equation to take into account heating due to the resistivity.

The next model, which introduces some extra detail of ion and electron interactions with the neutrals is the **Hall MHD** regime. With ideal MHD, the magnetic field is effectively frozen into the plasma and is advected with the plasma with no diffusion. The situation with Hall MHD is similar in the sense that field freezing is present but now the magnetic field is frozen to the electron fluid. The motions of the ions and electrons are not modeled independently in the Hall MHD model. The hall term disappears when $v_e = v_i$. So to find the relative velocities of the ions and electrons, or current, the curl of the magnetic field must be taken.

The Hall term becomes quite important if the characteristic length scale of the modeled system is greater than or comparable to the electron inertial length scale $L \gtrsim c/\omega_{pe}$ or smaller than the ion inertial length scale (the ion inertial region) where ω_{pe} and ω_{pi} are the electron and ion plasma frequencies (Chacón et al., 2002). The plasma frequencies result from small, rapid density oscillations in the plasma. Consider a cloud of electrons and ions. The electrons are much lighter than ions and may be displaced more easily, the Coulomb force acts as the restoring force leading to oscillation. The electron plasma frequency is given by $\omega_{pe} = \sqrt{\frac{4\pi n_e e^2}{m_e}}$. The ion plasma frequency is much smaller as they are much heavier and is given by $\omega_{pi} = \sqrt{\frac{4\pi n_i Z^2 e^2}{m_i}}$.

The Hall scale, the scale at which the ions decouple from the electrons is inversely proportional to the ionisation fraction. So, in weakly ionised plasmas the ion inertial length scale may be quite large. On length scales shorter than the ion inertial length scale, the ions can decouple from the magnetic field due to collisions with the neutrals, so Hall MHD may be appropriate for the study of large scale cold, weakly ionised accretion disks (Pandey and Wardle, 2008).

The induction equation must now include a Hall term to account for these effects:

$$\mathbf{E} + \mathbf{v} \times \mathbf{B} = \frac{1}{ne} \mathbf{J} \times \mathbf{B} \quad (2.33)$$

where n is the total ion number density and e is the electron charge.

Using a similar approach as in the ideal and resistive cases, one can obtain the following induction equation:

$$\frac{\partial \mathbf{B}}{\partial t} = \nabla \times \left((\mathbf{v} \times \mathbf{B}) - \frac{1}{ne} \mathbf{J} \times \mathbf{B} \right) \quad (2.34)$$

The next natural step is to consider the treatment of multiple fluids separately.

2.2 The Multi-fluid Model

Multi-fluid MHD is arrived at through a general relaxation of the assumptions that lead to ideal MHD. The progression of this relaxation can be followed from earlier in this chapter to arrive at this point. Thus far, the physics have been restricted to that of a single fluid. The next step in that progression leads to the treatment of multiple fluids. That is, a neutral fluid and possibly many charged fluids like the electron fluid and ion fluid and charged dust grains. The interaction of the species with one another through collisions is also modeled.

This leads to a very detailed and rich picture of the underlying physics involved in the context being studied. Each species has its own continuity equation, momentum equation and energy equation. Approximations based on the masses of charged species and whether or not mass or energy transfer exists between species may simplify such a model and make it less computationally expensive.

When considering non-ideal MHD such as the multi-fluid regime, the following effects are found due to the relative motions and collisions between the neutral and charged species and these effects should be included in the

dynamics to ensure the validity of the model.

Hall effect: Moving charged particles which are in the presence of a magnetic field are affected by the Lorentz force, which causes the particles to deviate from their path. Electrons are negatively charged and ions and dust grains may be negatively or positively charged. The force experienced by these particles acts in opposite directions depending on their charges, which causes a separation of these charges. This is the Hall effect. The Hall effect contributes to the breakdown of flux freezing (Wardle 2004a).

Ohmic resistivity: Ohmic resistivity is caused by the collision of charged particles, travelling along field lines, and other particles that are travelling at different velocities. These collisions cause resistance to the current of charged particles, this is seen as an electrical resistivity. The current, in the presence of a magnetic field can be decomposed into one component parallel and one component perpendicular to the magnetic field. Ohmic resistivity when used in this text refers only to the component parallel to the magnetic field. The component perpendicular to the magnetic field is taken into account with the ambipolar resistivity, discussed next.

Ambipolar diffusion: As in the case of Ohmic dissipation, ambipolar diffusion is due to collisions between charged and neutral particles. The charged species are affected by the Lorentz force and the neutral component is not directly affected. However the charged and neutral species are coupled to some degree by collisions. The ions and electrons which are tied to the magnetic field, diffuse together through the neutral fluid.

How important each of these terms become depends on the properties of the plasma in question. Astrophysical fluids vary greatly in terms of how much ionisation is present and in terms of how dense and dynamic they are. For example in accretion disks around young stars, the surface of the disk may be highly ionised due to radiation from the central object, whereas the midplane of the disk may possess quite a low ionisation fraction. High degrees of ionisation may also be present at the inner radii of the disk due to radiation emitted from the central star. Overall, it is typical to treat the gas present in an accretion disk around a young star as a cold, weakly ionised plasma (Wardle, 2004a) By making this assumption it greatly simplifies the derivation of the generalised Ohm's law where the Hall, ambipolar and Ohmic

contributions can be represented as separate terms.

If the plasma is assumed to be weakly ionised, then the neutral fluid is the dominant species of the plasma. As the ions and electrons will have similarly small number densities, it can easily be assumed that the majority of collisions will take place between the charged species and the neutral fluid and that collisions between the charged species will be negligible. In this case the pressure gradients of the charged species may also be ignored along with their inertial effects. This leads to a simplified momentum equation for the charged species,

$$\alpha_i \rho_i (\mathbf{E} + \mathbf{v}_i \times \mathbf{B}) + \rho_i \rho_1 K_{i1} (\mathbf{v}_1 - \mathbf{v}_i) = 0 \quad (2.35)$$

where, the subscripts 1 and i refer to the species in question, neutral and charged respectively, K_{i1} is the collisional coefficient which represents how common collisions between species i and the neutrals are, and α_i is the charge to mass ratio of species i . Mass transfer between species is neglected here for simplicity. Furthermore, if the assumption is made that the plasma is isothermal, then the energy equations for the neutrals and charged species may be disregarded and instead the closure relation $P_1 = \rho_1 c_s^2$ is used.

The induction equation is quite detailed, given that collisional effects are being taken into account and is given by

$$\frac{\partial \mathbf{B}}{\partial t} + \nabla \cdot (\mathbf{v}_1 \mathbf{B} - \mathbf{B} \mathbf{v}_1) = -\nabla \times \mathbf{E}' \quad (2.36)$$

where \mathbf{E}' is the electric field in the rest frame of the neutrals, and is taken from the local rest frame of the plasma. \mathbf{E}' may be found using the relation $\mathbf{E}' = \mathbf{E} + \mathbf{v} \times \mathbf{B}$ (Falle, 2003). In the weakly ionised approximation, the generalised Ohm's law, which takes multifluid effects into account, can be simplified. The derivation of the generalised Ohm's law for the weakly ionised case will be outlined in the next section (see section 2.3).

Each species has its own continuity equation of the form,

$$\frac{\partial \rho_i}{\partial t} + \nabla \cdot \rho_i \mathbf{v}_i = 0 \quad (2.37)$$

Note that conversions between species is neglected here. The momentum equation for the neutrals follows the above assumptions that the charged species are inertia-less as so have very little effect on the neutral fluid itself. The momentum equation for the neutrals is given by

$$\frac{\partial \rho_1 \mathbf{v}_1}{\partial t} + \nabla \cdot (\rho_1 \mathbf{v}_1 \mathbf{v}_1 + c_s^2 \rho_0 \mathbf{I}) = \mathbf{J} \times \mathbf{B} \quad (2.38)$$

The term $\mathbf{J} \times \mathbf{B}$ appears in the momentum equation for the neutrals, which may seem unexpected at first. It is important to note that this term appears due to the ion-neutral drag force.

The solenoidal condition $\nabla \cdot \mathbf{B} = 0$ applies as usual. The current density is given by $\mathbf{J} = \nabla \times \mathbf{B}$.

Charge neutrality is assumed as long as the length scale in question is larger than the Debye length which is guaranteed when considering accretion disk systems.

$$\sum_{i=2}^n \alpha_i \rho_i = 0 \quad (2.39)$$

Certain non-ideal properties, which may be modelled by the multi-fluid regime have been shown to have significant consequences for astrophysical processes such as accretion and the long term evolution of accretion disks (Bai, 2011; Bai and Stone, 2011; Sano and Stone, 2002a,b).

2.3 Generalised Ohm's Law

In plasma physics, Ohm's Law relates the current density in a plasma to the electric field acting on it. This relationship can be quite a complicated one. In an idealised situation, much like the one seen in resistive MHD, the classical Ohm's law, $\mathbf{J} = \eta^{-1} \mathbf{E}$ is typically used which states that the current is parallel and proportional to the electric field.

As discussed before, it is not hard to find situations where the classical Ohm's law breaks down and no longer accurately represents the current-electric field relationship such as when Hall or ambipolar processes begin to

be significant. When non-ideal effects are considered, a generalised Ohm's law must be considered.

Assuming that the plasma being studied is weakly ionised is a valid approximation for the inner regions of accretion disks around young stars (Salmeron and Wardle, 2003) and using the assumptions outlined in section 2.2, the weakly ionised generalised Ohm's law will now be derived.

In the weakly ionised case, the neutral species makes up the bulk of the plasma ($\rho_i \ll \rho_1$), so the bulk velocity can be assumed to be equation to the velocity of the neutral species.

$$\mathbf{v} = \mathbf{v}_1 \quad (2.40)$$

The charged species are approximated as inertia-less and the effects of pressure gradients in the charged species are negligible.

The momentum equation for the charged species (i) is given by Eq. 2.35 which is repeated here for convenience

$$\alpha_i \rho_i (\mathbf{E} + \mathbf{v}_i \times \mathbf{B}) + \rho_i \rho_1 K_{i1} (\mathbf{v}_1 - \mathbf{v}_i) = 0 \quad (2.41)$$

The current density is given by

$$\mathbf{J} = \sum_{i=2}^n \alpha_i \rho_i \mathbf{v}_i \quad (2.42)$$

where α_i , ρ_i and \mathbf{v}_i are the charge to mass ratio, density and velocity of species i respectively.

The charged momentum equation may be written in the frame of the bulk fluid to give

$$\alpha_i \rho_i (\mathbf{E}' + \mathbf{v}'_i \times \mathbf{B}) + \rho_i \rho_1 K_{i1} (-\mathbf{v}'_i) = 0 \quad (2.43)$$

where $\mathbf{v}'_i = \mathbf{v}_i - \mathbf{v}$ is the velocity of charged fluid i in the frame of the bulk fluid.

This equation is dependent on the collisional frequency K_{i1} but may be rewritten in terms of the magnetic flux and Hall parameter to give

$$\alpha_i \rho_i (\mathbf{E}' + \mathbf{v}'_i \times \mathbf{B}) - \frac{\mathbf{B}}{\beta_i} (\alpha_i \rho_i \mathbf{v}'_i) = 0 \quad (2.44)$$

where β_i is the Hall parameter. The Hall parameter is a measure of the relative importance between magnetic forces on the charged species and collisional drag of the charged species with the neutral species. It is given by the ratio between the collisional length scale and the Larmor radius of a particle of species i :

$$\beta_i = \frac{\alpha_i B}{\rho_1 K_{i1}} \quad (2.45)$$

where B is the magnitude of the magnetic field vector.

By writing the simplified charged momentum equation 2.44 separately by dimension, and assuming the magnetic field to be aligned in the z -direction and the electric field in the x -direction to be set to zero i.e. that the electric field is contained in the yz -plane only, then following set of equations for the x, y and z charged momenta are obtained:

$$\alpha_i \rho_i v'_{i,y} B_z - \frac{B}{\beta_i} \alpha_i \rho_i v'_{i,x} = 0 \quad (2.46)$$

$$\alpha_i \rho_i (E'_y - v'_{i,x} B_z) - \frac{B}{\beta_i} \alpha_i \rho_i v'_{i,y} = 0 \quad (2.47)$$

$$\alpha_i \rho_i E'_z - \frac{B}{\beta_i} \alpha_i \rho_i v'_{i,z} = 0 \quad (2.48)$$

where E'_y and E'_z are the electric fields perpendicular and parallel to the magnetic field respectively. For convenience the notation is changed so that $E'_y = E'_\perp$, $E'_z = E'_\parallel$. The electric field in the x -direction is given by $E' \times \mathbf{b}$, where \mathbf{b} is the unit vector in the direction of \mathbf{B} . The above set of equations may now be simplified before deriving the components of the current density.

$$\alpha_i \rho_i v'_{i,x} = \beta_i \alpha_i \rho_i v'_{i,y} \quad (2.49)$$

$$\alpha_i \rho_i v'_{i,y} = \frac{\beta_i}{B} \alpha_i \rho_i E'_\perp - \alpha_i \rho_i v'_{i,x} \beta_i \quad (2.50)$$

$$\alpha_i \rho_i v'_{i,z} = \frac{\beta_i}{B} \alpha_i \rho_i E'_\parallel \quad (2.51)$$

From the definition of current density (Eq. 2.42), it is now possible to write the current density in terms of its x , y and z components. The component parallel to the magnetic field is straightforward to find. To find the components perpendicular to the magnetic field, equations 2.49 and 2.50 must be solved simultaneously.

$$J_x = \sum_{i=2}^n \alpha_i \rho_i v'_{i,x} = \frac{1}{B} \sum_{i=2}^n \frac{\alpha_i \rho_i \beta_i^2}{1 + \beta_i^2} E'_\perp = \sigma_H E'_\perp \quad (2.52)$$

$$J_y = \sum_{i=2}^n \alpha_i \rho_i v'_{i,y} = \frac{1}{B} \sum_{i=2}^n \frac{\alpha_i \rho_i \beta_i}{1 + \beta_i^2} E'_\perp = \sigma_\perp E'_\perp \quad (2.53)$$

$$J_z = \sum_{i=2}^n \alpha_i \rho_i v'_{i,z} = \frac{1}{B} \sum_{i=2}^n \alpha_i \rho_i \beta_i E'_\parallel = \sigma_\parallel E'_\parallel \quad (2.54)$$

where σ_\parallel , σ_\perp and σ_H are the parallel, Pedersen and Hall conductivities respectively which are given by

$$\sigma_\parallel = \frac{1}{B} \sum_{i=2}^n \alpha_i \rho_i \beta_i \quad (2.55)$$

$$\sigma_\perp = \frac{1}{B} \sum_{i=2}^n \frac{\alpha_i \rho_i \beta_i}{1 + \beta_i^2} \quad (2.56)$$

$$\sigma_H = \frac{1}{B} \sum_{i=2}^n \frac{\alpha_i \rho_i \beta_i^2}{1 + \beta_i^2} \quad (2.57)$$

The current density can then be defined in terms of the electric field in

the frame of the bulk fluid in the form $\mathbf{J} = \sigma \cdot \mathbf{E}'$:

$$\mathbf{J} = \sigma_{\parallel} \mathbf{E}'_{\parallel} + \sigma_{\perp} \mathbf{E}'_{\perp} + \sigma_H (\mathbf{E}'_{\perp} \times \mathbf{b}) \quad (2.58)$$

The next step in the derivation is to express the electric field \mathbf{E}' in terms of the current density by inverting Eq.2.58. To do this, it is necessary to define the conductivity tensor (σ) formally (Norman and Hayvaerts, 1985).

$$\sigma = \begin{bmatrix} \sigma_{\perp} & \sigma_H & 0 \\ -\sigma_H & \sigma_{\perp} & 0 \\ 0 & 0 & \sigma_{\parallel} \end{bmatrix} \quad (2.59)$$

The inverse of σ is found to be

$$\sigma^{-1} = \begin{bmatrix} \frac{\sigma_{\perp}}{\sigma_{\perp}^2 + \sigma_H^2} & \frac{-\sigma_H}{\sigma_{\perp}^2 + \sigma_H^2} & 0 \\ \frac{\sigma_H}{\sigma_{\perp}^2 + \sigma_H^2} & \frac{\sigma_{\perp}}{\sigma_{\perp}^2 + \sigma_H^2} & 0 \\ 0 & 0 & \frac{1}{\sigma_{\parallel}} \end{bmatrix} = \begin{bmatrix} r_{\perp} & -r_H & 0 \\ r_H & r_{\perp} & 0 \\ 0 & 0 & r_{\parallel} \end{bmatrix} \quad (2.60)$$

where r_{\parallel} , r_H , and r_{\perp} are the Ohmic (field-parallel), Hall, and ambipolar resistivities respectively. The electric field (E') can now be written in terms of the current density to give $\mathbf{E}' = \sigma^{-1} \cdot \mathbf{J}$.

The electric field (\mathbf{E}') may be written as follows:

$$\begin{aligned} \mathbf{E}' &= r_{\parallel} \mathbf{J}_{\parallel} + r_H \mathbf{J}_{\perp} \times \mathbf{b} - r_{\perp} \mathbf{J}_{\perp} \\ &= r_{\parallel} \frac{(\mathbf{J} \cdot \mathbf{B}) \mathbf{B}}{B^2} + r_H \frac{(\mathbf{J} \times \mathbf{B})}{B} - r_{\perp} \frac{(\mathbf{J} \times \mathbf{B}) \times \mathbf{B}}{B^2} \end{aligned} \quad (2.61)$$

where \mathbf{J}_{\parallel} and \mathbf{J}_{\perp} are the currents parallel and perpendicular to the magnetic field. The generalised Ohm's law for a weakly ionised plasma may finally be written in the rest frame (Ciolek and Roberge, 2002; Falle, 2003)

$$\mathbf{E} = -\mathbf{v} \times \mathbf{B} + r_{\parallel} \frac{(\mathbf{J} \cdot \mathbf{B}) \mathbf{B}}{B^2} + r_H \frac{(\mathbf{J} \times \mathbf{B})}{B} - r_{\perp} \frac{(\mathbf{J} \times \mathbf{B}) \times \mathbf{B}}{B^2} \quad (2.62)$$

The full set of multifluid MHD equations are presented in section 3.1 for the weakly ionised approximation.

2.4 Multifluid MRI

Protostellar disks can be quite cold and dense and may be badly coupled to the magnetic field in some regions. This low level of coupling may make ideal MHD studies of the MRI questionable depending on the parameter space. In weakly ionised accretion disks, the assumptions behind ideal MHD may breakdown and non-ideal processes cannot be ignored. The non-ideal processes that are modelled with the multi-fluid approach, namely Ohmic dissipation, ambipolar diffusion and the Hall effect, may have different importance depending on what location of the disk is being studied.

Currently, no global multifluid numerical studies exist for accretion disks around young stars which look at the influence of the MRI on angular momentum transport. However, several studies that specifically look at the effect of Ohmic, ambipolar and/or Hall diffusion on the anomalous viscosity using analytic methods or local simulations exist. The consequences of the various non-ideal effects on the evolution of the MRI will now be discussed.

Ohmic dissipation is known to weaken turbulence caused by the MRI and can change the saturation level of the MRI. The importance of Ohmic dissipation is easily measured by the magnetic Reynolds number, which is a measure of the relative importance of advection and diffusion and is given by $R_M = VL/\eta_o$, where η_o is the Ohmic resistivity. Given that the characteristic length scale of the MRI is given by $\lambda_{mri} = 2\pi v_a/\Omega$, then $R_M \approx 2\pi V v_a/\Omega \eta_o$ and therefore it is reasonable to expect that the growth of the MRI will be severely hampered if R_m is of order of unity or below. Effectively diffusion is outrunning growth when this condition is met. A study by Fleming et al. (2000) actually found that this limit is potentially much higher and that turbulence may be killed off completely if $R_m \leq 10^4$.

In the study of Sano and Stone (2002a,b), the MRI was studied using local simulations in Hall-Ohm regime where Ohmic resistivity is large enough to have a damping effect on the MRI. Although the Hall effect was believed to allow the MRI to grow in situations where Ohmic and ambipolar diffu-

sion would normally suppress the MRI entirely (Wardle and Ng, 1999), the simulations of Sano & Stone did not illustrate this. However, the parameter space studied in this case is also narrow and had not adequately addressed the Hall dominated regime which would be common in protostellar disks where the Hall dominated region constitutes a large extent of the disk (Pandey and Wardle, 2012; Wardle and Salmeron, 2012). Ohmic diffusion is only the dominant in regions of relatively very high densities which are typically seen in the mid-plane of the disk within 1 AU.

Ambipolar diffusion arises from an imperfect coupling between the ions and the neutral fluids. In a weakly ionised plasma, this coupling may be weak and therefore allows the ions and magnetic field to which they are tied to diffuse through the neutral fluid. In the context of accretion disk physics, ambipolar diffusion is considered important once the frequency of ion-neutral collisions is similar or smaller to the orbital frequency of the disk. Once this situation occurs, ambipolar diffusion is known to have important consequences for the MRI. The reason for this is as the frequency of ion-neutral collisions fall when compared to the orbital frequency, the neutral fluid is influenced less and less by these collisions, and likewise the magnetic field is not dragged around and twisted as much by the neutral particles colliding with ions which are tied to the field lines. The consequence is that the neutrals are no longer influenced by any MRI-like effect at all and the instability will be damped. Ambipolar diffusion tends to dominate in regions where the densities are low and the magnetic field strength is high.

In the linear analysis of Blaes and Balbus (1994) where a two-fluid model was used, it was seen that when the ion-neutral collision frequency dropped below the orbital frequency, the MRI was indeed suppressed and that weaker fields were then required for the MRI to again become active and grow. This study considered only vertical wavenumbers. These results were later confirmed by Kunz and Balbus (2004) in a much more general case. In this study, axial and radial wavenumbers were allowed along with magnetic field geometries allowing axial and radial components.

The non-linear regime has been studied in the presence of ambipolar diffusion using 2 and 3-dimensional simulations and the local (shearing box) approach. Initial studies by Mac-Low et al. (1995) and Brandenburg et al. (1995) used the strong-coupling approximation. This means that rather than

treat the plasma as a two fluid model, where both the neutrals and ions are evolved separately and only interacting through collisions, the plasma may instead be considered a single fluid (Shu, 1991). This approximation is considered valid by these authors because the electron-ion recombination time is much smaller than the orbital frequency so that the ion density is only determined by the ionisation-recombination equilibrium with the neutrals. This is generally the case in weakly ionised disks like protoplanetary disks. The results of the linear analysis of Blaes and Balbus (1994) were again confirmed.

The two fluid model was again considered by Hawley and Stone (1998). It was found that when the ion-neutral collision frequency dropped below 0.01Ω , the ions and neutrals behave independently of each other and that when the ion-neutral collision frequency rose above 100Ω then the behavior of the disk approaches that seen in the ideal MHD regime.

It is typical in the literature to parameterise the importance of ambipolar diffusion using the dimensionless parameter Am which is defined as the ratio of the ion-neutral collision frequency to the orbital frequency and is given by

$$Am = \frac{\gamma\rho_i}{\Omega} \quad (2.63)$$

where γ is the ion-neutral collisional coefficient, ρ_i is the ion number density and Ω is the angular frequency. The numerator is therefore the ion-neutral collisional frequency and Am is dimensionless.

Most recently in the work of Bai and Stone (2011), an effort was made to study the non-linear evolution of the MRI in the presence of ambipolar diffusion using 3-dimensional simulations in the strong-coupling limit for constant values of Am . It was seen that when Am drops below unity, turbulence is seen to die away and the MRI is suppressed. As Am is increased, the saturation level of the magnetic stresses and the alpha parameter is seen to increase and so as a result the efficiency of angular momentum transport increases also leading to enhanced accretion. Once Am increases and goes beyond a value of 100, then the saturation amplitude of the stresses asymptotically approach those of the ideal MHD case. In the zero-net flux case the above result hold, however if a net field is applied it is actually possible to maintain turbulence as long as the magnetic flux is weak enough. The geometry of

the magnetic field is also seen to affect the saturation levels of the stress and alpha parameter in the presence of ambipolar diffusion. It is important to note this as the field geometry in local shearing box simulations is applied arbitrarily, whereas the actual field geometry is strongly related to the global evolution of the disk and therefore global simulations are required to fully understand the effect of ambipolar diffusion on the saturation of the MRI. It has also been shown in Simon et al. (2013) that density stratification has a negligible effect on the results obtained in Hawley and Stone (1998) and that the conclusions reached in this work in the case of vertical gravity component are very similar.

Ambipolar diffusion may have an important effect on the saturation level in the global evolution of accretion disks. Local simulations have been carried out to understand the role of ambipolar diffusion in accretion disks where the MRI is active. One such study presented in Bai and Stone (2011) and Bai (2011) has shown that the effect of ambipolar diffusion on the saturation of the MRI depends heavily on the field geometry. Field geometry is applied arbitrarily in local simulations so without going to global simulations, where field geometry is governed by the global evolution of the disk, it is difficult to determine exactly what effect ambipolar diffusion would have on the final saturation state of the disk. In the paper of Bai and Stone (2011) it is proposed that in a model similar to the one presented here, the initial growth of the MRI is probably governed by the Ohmic resistivity and/or Hall effect. However, once significant amplification of the magnetic field occurs ambipolar diffusion becomes important and may govern the properties of the MRI at saturation.

The Hall effect is very interesting as it can have both a stabilising and de-stabilising effect depending on the orientation of the magnetic field. The scenario where the Hall term dominates both the ambipolar term and Ohmic term has not been studied in much detail and no numerical results exist. As long as the Ohmic term remains small relative to the Hall term, the Hall effect may be important for the saturation of the MRI. A linear analysis was carried out by Salmeron and Wardle (2003) which suggests that the Hall effect does have important consequences for the growth and saturation of the MRI but this has not been confirmed by numerical studies.

Fig.2.2 is a schematic that describes the physical consequence of the

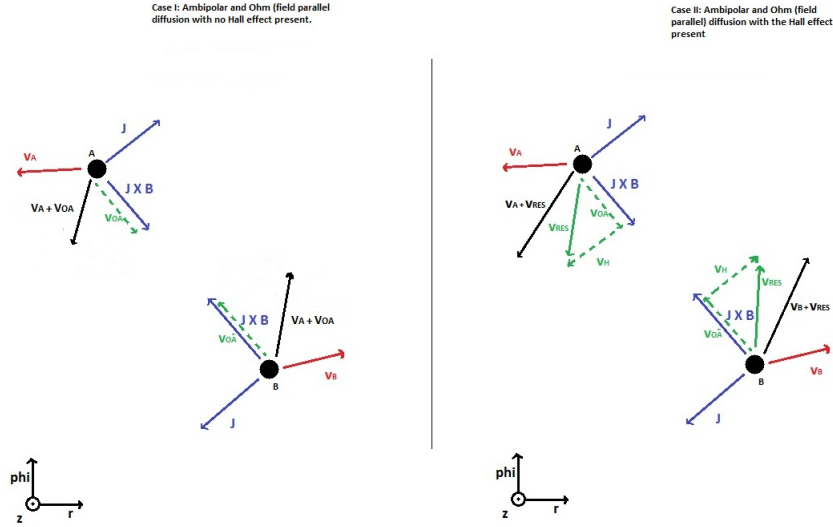


Figure 2.2: Vector diagram illustrating the influence of the Hall effect compared to just the diffusive terms alone. A and B are fluid elements which are separated radially and azimuthally due to rotation and the observer is in the frame of reference of the fluid. The MRI process has had time to act upon them and some angular momentum transfer has occurred from the inner element to the outer element (Wardle and Salmeron, 2012).

non-ideal effects on the development of the MRI. A description of the MRI in the ideal MHD regime has been presented in section 1.4.1. Both panes of Fig.2.2 show two fluid elements in the disk which are separated slightly radially and azimuthally due to the differential rotation. The observer is in the frame of reference of the fluid (corotating with the fluid elements). Both panes represent the fluid elements after the MRI process has had time to act upon them. The fluid elements have moved apart azimuthally, and some angular momentum transfer has occurred from element A to element B and a radial separation has resulted from this as the elements try to maintain angular momentum. The left pane describes the effect of Ohm and ambipolar diffusion and the right pane describes the effect when the Hall effect is present. When diffusion is present it has the effect of stabilising the disk by allowing the magnetic field to slip through the neutral fluid. In the left pane the Lorentz force acts to bring the elements closer together. The velocity of the elements resulting from this radial separation is represented by v_A and v_B for the inner and outer elements respectively. The field lines drift outwards and inwards for the field lines on which element A and B are situated upon

respectively and the MRI will develop more slowly as would be expected in the ideal MHD case where no diffusion of the magnetic field through the bulk fluid is allowed.

When the Hall effect is present it is believed to have a detabilising effect. The right pane of Fig.2.2 represents the physical situation here. The red vector v_a represents the magnitude and direction of travel for fluid element A and v_b represents the same for fluid element B . Some drift will occur due to both ambipolar and Ohmic diffusion which will occur in the direction of the Lorentz force which is orthogonal to the current \mathbf{J} and is represented by v_{OA} . The Hall effect also induces a drift (v_H) which is antiparallel with the current. The resultant drift vector v_{res} has a direction which is inwards radially for element A and outwards radially for element B which further destabilises the disk (Wardle and Salmeron, 2012). The drift velocity (v_{res}) may be found by writing the induction equation in a form such that the drift of the magnetic field through the fluid is made explicit, and is given by

$$\mathbf{v}_{res} = (r_o + r_H) \frac{(\nabla \times \mathbf{B})_{\perp} \times \hat{\mathbf{B}}}{B} - r_H \frac{(\nabla \times \mathbf{B})_{\perp}}{B} \quad (2.64)$$

Much work has been done in studying what effect the Hall term has on the growth phase of the MRI using linear analysis. In the study of Wardle and Ng (1999), vertical stratification is ignored. The linear analysis performed showed that the growth rate is dependent upon whether the magnetic field is parallel (enhanced growth rate) or anti-parallel (reduced growth rate) to the angular momentum vector of the disk i.e. the sign of $\boldsymbol{\Omega} \cdot \mathbf{B}$. This effect is due to the intrinsic handedness introduced by the Hall effect which arises from the difference in drifts between positively and negatively charged species. In weakly ionised disks such as protostellar disks, the coupling between the neutral and ions is poor. When this coupling is poor, the Hall effect causes the MRI to be active in regions where the disk normally would not be when $\boldsymbol{\Omega} \cdot \mathbf{B} > 0$, but when $\boldsymbol{\Omega} \cdot \mathbf{B} < 0$ there will be no instability when the coupling is poor (Wardle and Ng, 1999). The Ohmic and ambipolar diffusivities do not depend on the sign of $\boldsymbol{\Omega} \cdot \mathbf{B}$ and depend solely on the frequency of neutral-ion collisions. When coupling between the ions and neutrals are very poor there will be very little communication between the magnetic field and the neutrals through these collisions. The growth rate in the aligned case in a

weakly ionised disk remains finite and does not get entirely suppressed like in the Ohmic and ambipolar cases (Blaes and Balbus, 1994).

The linear analysis of Balbus and Tarquem (2001) confirmed this understanding and made the interesting observation that the Hall effect may cause instability in disks with both increasing and decreasing angular velocity profiles whereas the MRI in the ideal regime requires a decreasing profile. It was also observed that the inclusion of the Hall effect allowed MHD turbulence to be present in regions which were previously understood to be dead-zones in the disk where ionisation is so low that the neutral-ion collision frequency falls well below the orbital frequency where the MRI would be inactive and the disk would be non-turbulent (Fleming et al., 2000).

Recently, the linear analysis of Wardle and Salmeron (2012) included all diffusive effects. It was suspected from the results obtained that the depth of magnetically active layers in accretion disks may be wildly inaccurate due to the destabilising effect of the Hall effect and that protostellar and protoplanetary disks may be affected by MHD turbulence much closer to the mid plane than previously thought.

Simulations are required to understand what effect the Hall effect has upon the saturation level of the MRI. Currently no numerical simulations of accretion disks, local or global, exist in the literature where the Hall term dominates. In the study of Sano and Stone (2002a,b), the results of the above linear analysis regarding the dependence of the stability of the disk on the sign of $\boldsymbol{\Omega} \cdot \mathbf{B}$ are confirmed. For the first time the development of the MRI after saturation was studied. This study looked at the Hall-Ohm regime where both the Hall effect and Ohmic diffusion are important. From the linear analysis above it was expected that the Hall effect would destabilise disks in weakly ionised regions even where dissipation was severe. Hall diffusion may drastically extend or restrict the reach of magnetic activity in protoplanetary discs and likely modifies the transport and dissipative properties of the resulting turbulence (Wardle, 2007). The results in the above work of Sano et al suggested however that Hall diffusion was unable to overcome the damping effect of Ohmic diffusion (Wardle and Salmeron, 2012). It was pointed out in Wardle and Salmeron (2012) that on closer inspection, the parametrisation of the diffusive effects adopted by Sano and Stone (2002a,b) reveals that their simulations did not look at the regimes where Hall diffu-

sion dominates over Ohm diffusion or where both dominate over inductive effects. This is important as Hall diffusion is expected to dominate in the region of 1-30AU (Wardle and Salmeron, 2012).

The handedness introduced by the Hall effect means that the initial configuration of the magnetic field becomes more important. Just how the initial orientation of the magnetic field becomes important can be seen in Fig.2.3. In the left pane, the magnetic field points outwards from the page and in the right pane the magnetic field points into the page, i.e. aligned and counter-aligned with the angular momentum vector respectively. Fluid element A is separated from fluid element B radially and azimuthally due to rotation and the observer is in the frame of the disk (corotating with the fluid elements). Both panes represent the fluid elements after the MRI process has had time to act upon them. They have moved apart azimuthally due to differential rotation of the disk, some transfer of angular momentum has occurred and a radial separation has then resulted.

The red vector v_a represents the magnitude and direction of travel for fluid element A and v_b represents the same for fluid element B . Some drift will occur due to both ambipolar and Ohmic diffusion which will occur in the direction of the Lorentz force which is orthogonal to the current \mathbf{J} and is represented by v_{OA} . The Hall effect also induces a drift (v_H) which is antiparallel with the current. The resultant drift vector v_{res} has a direction which is inwards radially for element A and outwards radially for element B which further destabilises the disk (Wardle and Salmeron, 2012).

When the orientation of the magnetic field is reversed as in the right pane of Fig.2.3 the current now points in the opposite direction and the drift due to the Hall effect points is outwards radially for element A and inwards radially for element B giving a resultant velocity vector v_{res} which has the effect of stabilising the disk by straightening the field lines.

In the study of Sano and Stone (2002a,b), local 2-dimensional and 3-dimensional were carried out in the presence of the Hall effect. Sano and Stone (2002b) found that when the magnetic field was aligned or counter-aligned with the angular momentum vector that the MRI was enhanced or suppressed respectively. When the field was aligned, turbulence could be sustained for smaller values of the magnetic Reynolds number than in the

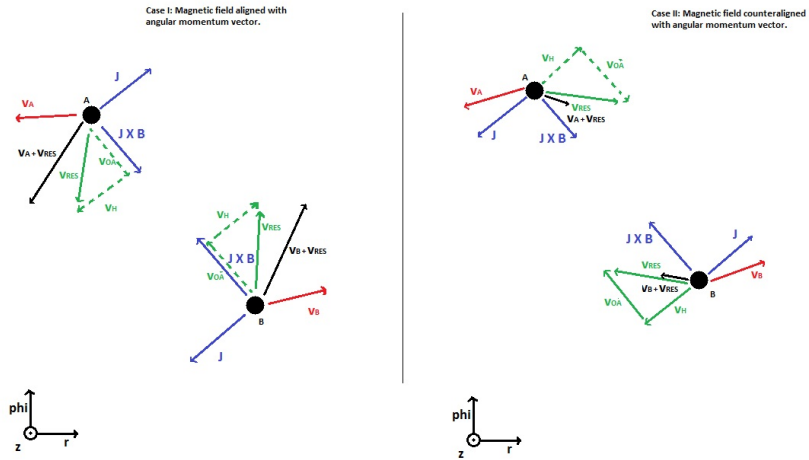


Figure 2.3: Vector diagram illustrating the influence of the magnetic field orientation relative to the angular momentum vector of the accretion disk. A and B are fluid elements which are separated radially and azimuthally due to rotation and the observer is in the frame of reference of the fluid. The MRI process has had time to act upon them and some angular momentum transfer has occurred from the inner element to the outer element (Wardle and Salmeron, 2012).

counteraligned case. These simulations were carried out in the Hall-Ohm regime. No simulations exist for the case where Hall diffusion is a dominant process. This is believed to be the situation in the radial range 1-30AU (Wardle and Salmeron, 2012).

Chapter 3

Numerical Methods

Typically, one can only get so far with analytic and semi-analytic methods when studying MHD before it becomes necessary to turn to numerical studies. Numerical models are used when the system of equations governing a model are simply too complicated to be solved analytically. The equations describing a particular model can be discretised and solved by using various numerical methods and then used to create simulations of specific physical situations of interest.

In the study of magnetised fluids, the governing equations are represented by a set of partial differential equations which are obtained by making some basic assumptions about the fluid, or fluids being studied. These equations may then be solved numerically. Typically the initial state of the fluid is represented by values of flow variables at specific points in space and then by the use of a numerical algorithm, this initial state may be advanced in time to produce qualitative and quantitative predictions about the flow in question.

Simulations of this type are invaluable in the study of astrophysics and allow astrophysicists to gain a greater understanding as to the origin of various astrophysical objects and enable them to make predictions as to the future evolutions of these objects.

Numerical studies are limited by the computational expenditure of their code and the computational resources available. This may put a limit on the detail with which a particular problem can be studied, either by putting a

limitation on the resolution of the simulations or on the detail of the model.

Simulations using parallel computing are becoming very common, and highly efficient algorithms are used to make the best use of the computational resources available. Advantages may be gained by exploiting the symmetry of the subjects of the simulation, which may also speed up code run times. Adaptive mesh refinement methods may also be used where finer subgrids are superimposed on the original grid which can be useful to track features such as shocks (Berger and Colella, 1989).

In this chapter, the numerical methods used in this work, along with details of the code used and information regarding what changes had to be made to make the accretion disk simulations possible are outlined and explained.

3.1 The multifluid Equations

The following set of equations model the evolution of a neutral fluid and $N-1$ charged fluids in the presence of a magnetic field. These equations govern a weakly ionised plasma. In the case of a weakly ionised plasma, the pressure and inertial terms of the evolutions equations for the ionised species may be ignored. This is because the mass density of the plasma is dominated by the neutral component (subscript of 1). In such a plasma the mean free path of the ionised species and the associated Larmor radii are much smaller than the mean free path of the neutrals and so the inertia and pressure gradients in the charged components (i) have a negligible effect on the neutral component (Ciolek and Roberge, 2002; Falle, 2003). An isothermal closure relation is used, therefore allowing the energy equations for the neutrals and ionised species to be ignored.

$$\frac{\partial \rho_i}{\partial t} + \nabla \cdot (\rho_i \mathbf{v}_i) = 0 \quad (3.1)$$

$$\frac{\partial \rho_1 \mathbf{v}_1}{\partial t} + \nabla \cdot (\rho_1 \mathbf{v}_1 \mathbf{v}_1 + p_1 I) = \mathbf{J} \times \mathbf{B} \quad (3.2)$$

$$\frac{\partial \mathbf{B}}{\partial t} + \nabla \cdot (\mathbf{v}_1 \mathbf{B} - \mathbf{B} \mathbf{v}_1) = -\nabla \times \mathbf{E}' \quad (3.3)$$

$$\alpha_i \rho_i (\mathbf{E} + \mathbf{v}_i \times \mathbf{B}) + \rho_i \rho_1 K_{i1} (\mathbf{v}_1 - \mathbf{v}_i) = 0 \quad (3.4)$$

$$\nabla \cdot \mathbf{B} = 0 \quad (3.5)$$

$$\nabla \times \mathbf{B} = \mathbf{J} \quad (3.6)$$

$$\sum_{i=2}^n \alpha_i \rho_i = 0 \quad (3.7)$$

$$\sum_{i=2}^n \alpha_i \rho_i \mathbf{v}_i = \mathbf{J} \quad (3.8)$$

The subscripts in the above equations denote the species in question. The neutral component is represented by a subscript of 1, and the charged species are denoted by subscript 2 to n . The variables ρ_i , \mathbf{v}_i , p_i represent the mass density, pressure and velocity of species i respectively. The collisional coefficient K_{i1} represents the collisional interaction between species i and the neutral fluid. The charge to mass ratio of the i^{th} species is represented by α_i . The identity matrix, current density, and magnetic flux density are represented by I , \mathbf{J} and \mathbf{B} respectively and finally the full electric field is given by $\mathbf{E} = -\mathbf{v}_1 \times \mathbf{B} + \mathbf{E}'$. One more equation is needed to close the set. An equation of state may be used. In this case the isothermal relation $c_s^2 = p_1/\rho_1$ is added to the set.

An expression for the electric field in the frame of the fluid may be obtained by comparing the above expression for the full electric field to Eq.2.61 and Eq.2.62:

$$\mathbf{E}' = r_o \frac{(\mathbf{J} \cdot \mathbf{B}) \mathbf{B}}{B^2} + r_H \frac{(\mathbf{J} \times \mathbf{B})}{B} + r_A \frac{(\mathbf{J} \times \mathbf{B}) \times \mathbf{B}}{B^2} \quad (3.9)$$

where

$$\mathbf{J}_{\parallel} = \frac{(\mathbf{J} \cdot \mathbf{B})\mathbf{B}}{B^2} \quad (3.10)$$

$$\mathbf{J}_{\Lambda} = \frac{(\mathbf{J} \times \mathbf{B})}{B} \quad (3.11)$$

$$\mathbf{J}_{\perp} = \frac{(\mathbf{J} \times \mathbf{B}) \times \mathbf{B}}{B^2} \quad (3.12)$$

and the Ohmic (field parallel), Hall and ambipolar resistivities are defined respectively by

$$r_o \equiv \frac{1}{\sigma_o} \quad (3.13)$$

$$r_H \equiv \frac{\sigma_H}{\sigma_H^2 + \sigma_A^2} \quad (3.14)$$

$$r_A \equiv \frac{\sigma_A}{\sigma_H^2 + \sigma_A^2} \quad (3.15)$$

The conductivities in Eqns 3.13 - 3.15 are defined for each charged species i by

$$\sigma_o = \frac{1}{B} \sum_{i=2}^n \alpha_i \rho_i \beta_i \quad (3.16)$$

$$\sigma_H = \frac{1}{B} \sum_{i=2}^n \frac{\alpha_i \rho_i}{1 + \beta_i^2} \quad (3.17)$$

$$\sigma_A = \frac{1}{B} \sum_{i=2}^n \frac{\alpha_i \rho_i \beta_i}{1 + \beta_i^2} \quad (3.18)$$

where (β_i) is the Hall parameter for the charged species and is a measure of how well tied to the magnetic field the charged species (i). This is given by

$$\beta_i = \frac{\alpha_i B}{K_{i1} \rho_1} \quad (3.19)$$

Equation 3.1 to 3.4 are the conservation equations for mass, neutral momentum, magnetic flux and charged species momentum respectively. Equation 3.5 is the solenoidal condition, the consequence of which is that no magnetic monopoles may exist in the solution. Divergence errors may be gradually introduced via discretisation error for example and this condition can be problematic to enforce numerically. A divergence free field may be enforced directly by the algorithm by writing the MHD equations in terms of the magnetic vector potential, or alternatively it may be maintained by using an additional method that is used to apply divergence cleaning to the solution. This is achieved by using correction terms within the scheme. In HYDRA, a parabolic correction term is used to dissipate divergence errors and effectively smooths out the errors. Also a hyperbolic correction term is used to advect any divergence errors towards the nearest boundary at a maximal speed (see section 3.2.2 for details). Equation 3.6 to 3.8 are Ampere's Law, charge neutrality condition and the charged current equation respectively.

These equations may then be solved numerically by choosing a method of discretisation. For this work, the numerical code HYDRA was used and subsequently modified to suit the specific needs of an accretion disk model. This code will be described in the next section (see section 3.2).

3.2 HYDRA: Multifluid MHD code

The code used for this study is HYDRA (O'Sullivan and Downes, 2006, 2007). The scheme used by this code to integrate the multifluid equations in the weakly ionised limit, described in the previous section, is fully explicit. It is a finite-volume shock-capturing code which is accurate up to 2^{nd} order in both space and time. The code is relatively easy to parallelise due to the fact it uses an explicit scheme. Parallelisation is achieved through a simple domain decomposition. The code may be run in an ideal MHD mode should this capability be desired. This is important to this work as many results regarding global simulations of accretion disks have been carried out in the

ideal framework. This makes it possible to check the model against existing results to ensure that no undesirable effect due to set-up errors are present.

The code has been utilised in a number of works modelling non-ideal MHD turbulent decay (Downes, 2012; Downes and O’Sullivan, 2009, 2011), and the Kelvin-Helmholtz instability in weakly and fully ionised plasmas (Jones and Downes, 2011, 2012).

The purpose of this thesis is to study the dynamics of an accretion disk around a young star utilising numerical simulations based on information gained from observations of known protostellar disks. Similar simulations have been carried out in the past and results regarding the anomalous viscosity, accretion rates and information about the physical processes at work have been published. However, many of these results were obtained using local (shearing-box type) simulations or were carried out in the ideal framework which may not capture all the physics involved.

This work is the first attempt at high resolution, multifluid MHD simulations of the development and influence of the MRI on accretion disk dynamics and will provide detailed information about the nature and structure of accretion disks around young stars when multifluid effects are taken into account.

3.2.1 Numerical Algorithm

The numerical code HYDRA is used to solve the multifluid evolution equations. The algorithm used to solve these equations numerically will be described in the following pages.

First, the solution of the equations is assumed to be piecewise constant at time t^r on a uniform mesh described by a Cartesian coordinate system with indices (i, j, k) describing the position in 3D space of a given cell within a computational domain of size $(n\Delta x, m\Delta y, l\Delta z)$ where Δx refers to the spacing in the x-direction and so on, and (n, m, l) are the number of cells in the x, y and z directions respectively. If a uniform spacing is assumed in all directions such that $\Delta x = \Delta y = \Delta z = h$, then the state in a given cell (i, j, k) represents the volume average over $(i - 1/2)h \leq x \leq (i + 1/2)h$, $(j - 1/2)h \leq y \leq (j + 1/2)h$, and $(k - 1/2)h \leq z \leq (k + 1/2)h$ and is defined

at the center of mass.

To obtain a solution at $t^{\tau+1}$ standard finite volume methods are used to evolve Eq. 3.1 - 3.3. The time integration of these equations is multiplicatively operator split into 3 separate operations which may be summarised as follows:

- (i) The neutral fluid is advanced. Equations 3.1, 3.2, and 3.3, with index $i = 1$ for equation 3.1 are solved using a standard finite volume integration method to 2nd order temporal and spatial accuracy. The diffusive term on the RHS of Equation 3.3 is not evaluated until a later step. The solenoidal condition described by equation 3.5 is also maintained using the method of Dedner (Dedner et al., 2002) which will be described in section 3.2.2. Second order accuracy in space and time is obtained by evaluating the fluxes from a piecewise-constant solution at t^τ for the primitive fluid variables ρ_1 , \mathbf{v}_1 and P_1 using a magnetohydrodynamic Riemann solver. A time-centered solution at $t^{\tau+1/2}$ is found using these fluxes, which is then reconstructed to a 2nd order piecewise-linear solution using non-linear averaging for the gradients. A new set of fluxes which are accurate to 2nd order, in space and time, may then be found. These fluxes may then be applied to the conserved variables.
- (ii) The diffusive term in equation 3.3 is now evaluated. By using standard discretisation, a restriction is imposed by the vanishing timestep associated with very high values of Hall resistivity (O’Sullivan and Downes, 2006, 2007). To overcome this problem, the induction equation is integrated by multiplicatively operator splitting the Hall and ambipolar terms. Special techniques are then used to advance the Hall and ambipolar terms efficiently while simultaneously relaxing the timestep restriction and maintaining 2nd order accuracy. These techniques, known as super-timestepping and Hall diffusion scheme will be discussed in sections 3.3.1 and 3.3.2 respectively.
- (iii) Finally, the densities and velocities of the various charged species are evaluated. The densities are evaluated using the mass conservation equation 3.1 for $1 \leq i \leq N - 1$, where N is the number of fluids.

The charged fluid velocities are determined analytically. First of all, the current density is evaluated using equation 3.6. The electric field

may then be determined by using the generalised Ohm's law,

$$\mathbf{E}' = r_o \frac{(\mathbf{J} \cdot \mathbf{B})\mathbf{B}}{B^2} + r_H \frac{(\mathbf{J} \times \mathbf{B})}{B} + r_A \frac{(\mathbf{J} \times \mathbf{B}) \times \mathbf{B}}{B^2} \quad (3.20)$$

Equation 3.4, the momentum equation for the charged species, may be written in a frame of reference co-moving with the neutral fluid to give

$$\mathbf{v}'_i \times \mathbf{B} - \frac{\rho_1 K_{i1} \mathbf{v}'_i}{\alpha_i} = \mathbf{E}' \quad (3.21)$$

The charged velocities, assuming the collisional coefficients are constant, may then be given by

$$\mathbf{v}'_i = -\mathbf{A}_i^{-1} \mathbf{E}' \quad (3.22)$$

where the matrix \mathbf{A} is given by

$$\mathbf{A}_i = \begin{pmatrix} -K_i & B_z & -B_y \\ -B_z & -K_i & B_x \\ B_y & -B_x & -K_i \end{pmatrix}$$

The charged velocities are then obtained using

$$\mathbf{v}_i = \mathbf{v}'_i + \mathbf{v} \quad (3.23)$$

The order of the above operations (*i-iii*) are permuted to maintain 2nd order accuracy by avoiding introducing errors caused by directional bias into the solution (Strang, 1968).

3.2.2 $\nabla \cdot \mathbf{B}$ control

The magnetic field is a solenoidal field and Gauss' law for magnetism must hold unless magnetic monopoles are to be admitted, that is

$$\nabla \cdot \mathbf{B} = 0 \quad (3.24)$$

Most numerical studies of MHD must include some form of control to maintain this condition. Some algorithms enforce a divergence free magnetic field such as those which utilise the method of constrained transport or those that evolve the magnetic vector potential.

Numerical codes use approximations to calculate the solutions to mathematical problems, where accuracy primarily depends on the numerical scheme used. Divergence errors are typically introduced by truncation error and also to a lesser extent by numerical precision.

Truncation error can be reduced by using higher order schemes but problems may be caused when low resolutions are used where there are steep gradients in the fluid variables. Typically a higher resolution is desirable to minimise truncation errors. Numerical precision can be improved by minimising the need for high precision arithmetic in the code. However, the precision available is hardware dependent and for the most part can't be helped.

The divergence restriction on the magnetic field is quite sensitive to numerical accuracy, the divergence is typically non-zero on grid with a dynamic fluid and divergence errors can grow quite rapidly over a relatively small number of timesteps. Once significant errors appear, they tend to grow and spread and introduce spurious forces to the grid. With long term calculations, this leads to quite inconsistent results and/or code crashes.

A divergence free field must therefore be enforced or maintained somehow. This may be done by solving for the magnetic vector potential rather than the magnetic field directly, this is typically undesirable as it is more computationally expensive and can admit more noise in the solution. The advantage is that the solenoidal condition is implicitly enforced (Lyra et al., 2008). The method introduces 2nd order derivatives of the vector potential in the Lorentz term of the momentum equation which requires extra measures to maintain 2nd order accuracy. Another popular method is the constrained transport procedure which introduces a zero-divergence preserving update step utilising a staggered mesh where some quantities are located at cell edges and others are located at cell centers (e.g. Hawley and Stone (1995) and Athena code).

Another group of methods which rely upon maintaining a very small

value $\nabla \cdot \mathbf{B}$ on the computational grid is that of divergence cleaners. One such method is that of Powell (Powell et al., 1999). This method explicitly adds source terms to the induction and momentum equation which has the effect of advecting divergence errors to other areas of the grid thereby halting the build-up of divergence errors locally. Another example of a divergence cleaning method, which is utilised by HYDRA, is the method of Dedner (Dedner et al., 2002). This method utilises a similar advection method as Powell but also adds a diffusive term to the induction equation that diffuses divergence errors. This is why the method of Powell is no longer used as the method of Dedner uses the same method of advecting divergence errors but also reduces the errors over time. The advection method has the disadvantage of not being effective if periodic boundary conditions are used as the errors will be advected through the boundary and will re-enter through the opposite boundary, therefore the addition of the diffusive term makes the method of Dedner quite superior.

3.3 Stability Analysis

There are some restrictions encountered when solving the induction equation (Eq.3.3). The stable timestep may become vanishingly small if the Hall resistivity becomes large. As mentioned in Section 3.2.1, the diffusive term is solved separately using the Hall diffusion scheme (O’Sullivan and Downes, 2006). To study the stability of the multifluid algorithm it is first assumed that the Ohmic resistivity is negligibly small on the basis that the collisional drag on the charged species is dominated by the magnetic forces. The hyperbolic term in the induction equation is split out and solved separately leaving the following induction equation

$$\frac{\partial \mathbf{B}}{\partial t} = -\nabla \times \mathbf{E}' = -\nabla \times (\mathbf{E}_O + \mathbf{E}_H + \mathbf{E}_A) \quad (3.25)$$

The following expansion of the term on the RHS is carried out

$$\nabla \times \mathbf{E}_X = \mathbf{F}_X^1 + \mathbf{F}_X^2 \quad (3.26)$$

where the subscript $X = O, H, A$ and \mathbf{F}^1 and \mathbf{F}^2 are the linear and second

order terms respectively. The Ohmic case can be ignored due to the assumption regarding collisional drag and so the first and second order terms can be found to be

$$\mathbf{F}_H^1 = (\mathbf{a}_H \cdot \nabla) \mathbf{J} \quad (3.27)$$

$$\mathbf{F}_H^2 = -(\mathbf{J} \cdot \nabla) \mathbf{a}_H + (\nabla \cdot \mathbf{a}_H) \mathbf{J} \quad (3.28)$$

and,

$$\mathbf{F}_A^1 = [\mathbf{a}_A \cdot (\nabla \times \mathbf{J})] \mathbf{a}_A - [(\mathbf{a}_A \cdot \nabla) \mathbf{J}] \times \mathbf{a}_A \quad (3.29)$$

$$\mathbf{F}_A^2 = [\mathbf{a}_A \cdot (\nabla \times \mathbf{a}_A)] \mathbf{J} - [(\mathbf{J} \cdot \nabla) \mathbf{a}_A] \times \mathbf{a}_A - 2(\mathbf{J} \cdot \mathbf{a}_A) (\nabla \times \mathbf{a}_A) + (\nabla a_A^2) \times \mathbf{J} \quad (3.30)$$

where $\mathbf{a}_A = \sqrt{r_A} \mathbf{b}$ and $\mathbf{a}_H = r_H \mathbf{b}$ where $\mathbf{b} = \mathbf{B}/B$. It is also assumed that only small perturbations about a mean field are present, this allows the 2nd order diffusion terms to be neglected, leaving just the linear terms. The reduced induction equation is then given by

$$\frac{\partial \mathbf{B}}{\partial t} \approx \mathbf{F}_A^1 + \mathbf{F}_H^1 \quad (3.31)$$

This may be rewritten in the following form

$$\frac{\partial \mathbf{B}}{\partial t} = -\mathbf{G} \mathbf{B} \quad (3.32)$$

where the matrix operator \mathbf{G} is given by the sum of the ambipolar and Hall components, $\mathbf{G} = \mathbf{G}_A + \mathbf{G}_H$. By using the unit vector $\mathbf{b} = \mathbf{B}/B$, \mathbf{G}_A and \mathbf{G}_H are given by

$$\mathbf{G}_A = -r_H (\mathbf{b} \cdot \nabla) (\nabla \times \cdot) \quad (3.33)$$

$$\mathbf{G}_H = r_A[\mathbf{b} \cdot (\nabla \times (\nabla \times \cdot))]\mathbf{b} - r_A[(\mathbf{b} \cdot \nabla)(\nabla \times \cdot)] \times \mathbf{b} \quad (3.34)$$

The operator \mathbf{G} can be written in discretised form as follows

$$\left(\frac{\partial^2 \mathbf{B}}{\partial x^2}\right)_i = \frac{B_{i+1} - 2B_i + B_{i-1}}{h^2} \quad (3.35)$$

$$\left(\frac{\partial^2 \mathbf{B}}{\partial x \partial y}\right)_{ij} = \frac{B_{i+1j+1} - B_{i+1j-1} - B_{i-1j+1} + B_{i-1j-1}}{4h^2} \quad (3.36)$$

and so on for the other terms. Next, to begin analysing the stability properties of the scheme, a numerical waveform is assumed for the magnetic field such that $\mathbf{B}_i^n = B_0 e^{i\omega \cdot \mathbf{i}}$, where $\mathbf{i} = (i, j, k)$, $\omega = (\omega_x, \omega_y, \omega_z)$ and $i = \sqrt{-1}$. Using the above discretisations, the derivatives may be calculated as follows

$$\frac{\partial^2 \mathbf{B}}{\partial x^2} \rightarrow \lambda_{xx} = -2(1 - \cos(\omega_x)) \quad (3.37)$$

$$\frac{\partial^2 \mathbf{B}}{\partial x \partial y} \rightarrow \lambda_{xy} = -\sin(\omega_x) \sin(\omega_y) \quad (3.38)$$

and so on for the remaining derivatives. At this point a matrix Λ may be defined whose (x,y) members are given by λ_{xy} . By applying the substitutions given by 3.37 and 3.38 to the discretised operators \mathbf{G}_A and \mathbf{G}_H , the following skew symmetric matrices may be found

$$\mathbf{A}_H = \begin{pmatrix} 0 & \zeta_z & -\zeta_y \\ -\zeta_z & 0 & \zeta_x \\ \zeta_y & -\zeta_x & 0 \end{pmatrix}$$

and

$$\mathbf{A}_A = \mathbf{b}\zeta + \zeta\mathbf{b} - \text{tr}(\Lambda)\mathbf{b}\mathbf{b} - \mathbf{b}^T \zeta \mathbf{I} \quad (3.39)$$

where $\zeta = \Lambda\mathbf{b}$, and $\mathbf{b}\zeta$ is a diadic formed from \mathbf{b} and ζ .

The standard discretisation may now be written as

$$\mathbf{B}^{n+1} = (\mathbf{I} - \tau \mathbf{G}_H^n - \tau \mathbf{G}_A^n) \mathbf{B}^n \quad (3.40)$$

or by substituting the numerical waveform $\mathbf{B}_i^n = B_0 e^{i\omega \cdot \mathbf{i}}$ the following standard discretisation may be found

$$\mathbf{B}^{n+1} = (\mathbf{I} - \alpha r_H \mathbf{A}_H - \alpha r_A \mathbf{A}_A) \mathbf{B}^n \quad (3.41)$$

where $\alpha = \tau/h^2$.

To study the stability of this discretisation, the following definitions are made; first the relative importance of the ambipolar and Hall resistivities is parameterised as $\eta = r_A/|r_H|$, and secondly the characteristic cell crossing time for diffusion perpendicular to the magnetic field is given by

$$\tau^\perp = \frac{h^2}{2\sqrt{r_A^2 + r_H^2}} \quad (3.42)$$

Time intervals are therefore normalised such that $\bar{\tau} = \tau/\tau^\perp$. Two cases are now studied where only ambipolar or Hall diffusion are present and the timestep stability limits are found.

In the case of dominant Hall diffusion, the ambipolar amplification matrix \mathbf{A}_A is neglected and so the evolution operator for the magnetic field (Eq.3.41) reduces to $(\mathbf{I} - \alpha r_H \mathbf{A}_H)$. The eigenvalues of the reduced evolution operator are then found to be

$$\mu_1 = 1 \quad (3.43)$$

$$\mu_{2,3} = 1 \pm i\alpha r_H \zeta \quad (3.44)$$

The spectral radius of the reduced evolution operator is greater than unity when $\tau > 0$. Therefore the time-step will become vanishingly small for

high values of Hall resistivity relative to ambipolar resistivity.

$$\bar{\tau}_H^{STD} \rightarrow 0 \text{ as } \eta \rightarrow 0 \quad (3.45)$$

This leads to significant problems when studying Hall diffusion dominated systems. In O’Sullivan and Downes (2006) a novel numerical method, the Hall diffusion scheme, designed to overcome this restriction is discussed for the 1-dimensional case and in a follow-up paper (O’Sullivan and Downes, 2007) the method is expanded for the 3-dimensional case.

Similarly, in the case of dominant ambipolar diffusion, the amplification matrix \mathbf{A}_H is neglected. The evolution operator for the magnetic field reduces to $(\mathbf{I} - \alpha r_A \mathbf{A}_A)$. The eigenvalues of this reduced evolution operator are found to be

$$\mu_1 = 1 + \alpha r_A \mathbf{b}^T \boldsymbol{\zeta} \quad (3.46)$$

$$\mu_{2,3} = 1 + \frac{1}{2} \alpha r_A [|\text{tr}(\Lambda) \pm |\text{tr}(\Lambda) \mathbf{b} - 2\boldsymbol{\zeta}|] \quad (3.47)$$

Looking at the magnitudes of the eigenvalues it may be seen that the largest magnitude is found for $\omega = \pi(1, 1, 1)$ for an arbitrary magnetic field orientation and the minimum normalised stable time-step is found to be

$$\bar{\tau}_A^{STD} \leq \frac{1}{2} \sqrt{\frac{1 + \eta^2}{\eta}} \quad (3.48)$$

This case is much less restrictive than the Hall domination case. The HYDRA code utilises methods such as the Hall diffusion scheme to weaken the timestep restrictions imposed by non-ideal effects. These methods will be discussed in the following section (O’Sullivan and Downes, 2006).

3.3.1 Super-time-stepping

As has been mentioned in section 3.2.1, part of the numerical algorithm involves integrating the induction equation in two parts by multiplicatively operator splitting the Hall and ambipolar terms. A little known method

known as super-time-stepping is utilised to accelerate the timestepping for the standard discretisation scheme outlined above for ambipolar diffusion only. The method works on linear or non-linear parabolic problems by utilising carefully chosen substeps which are combined into a composite timestep known as a superstep. The stability requirement at the end of a timestep is relaxed and is only required at the end of a cycle of N_{sts} substeps (Alexiades et al., 1996) such that

$$\tau^{STS} = \sum_{n=1}^{N_{STS}} d\tau_n \quad (3.49)$$

For a given stable timestep for the standard discretisation in the case of ambipolar diffusion ($\bar{\tau}^{STD}$) super-time-stepping will result in the following stability limit

$$\lim_{\nu \rightarrow 0} \bar{\tau}_A^{STS} = N_{STS}^2 \bar{\tau}_A^{STD} \quad (3.50)$$

where ν is a damping factor, which is user defined within HYDRA. Super-time-stepping is first order accurate in time. To extend the accuracy of this method to second order, Richardson extrapolation is utilised (Richardson, 1911).

3.3.2 Hall Diffusion Scheme

In the Hall dominated case where ambipolar diffusion is ignored, the evolution operator ($\mathbf{I} - \alpha r_H \mathbf{A}_H$) is unstable and therefore standard explicit schemes will not be practical in cases where r_H is large. A novel method known as the Hall diffusion scheme (HDS) (O’Sullivan and Downes, 2006) is used to avoid this instability without having to resort to implicit methods which may be computationally expensive. The discretised operator Eq.3.34 is the basis of the HDS. The discretised matrix operator G_H is skew-symmetric, this property is exploited by the HDS so that the reduced induction equation for Hall only, $\frac{\partial \mathbf{B}}{\partial t} = -\mathbf{G}_H \mathbf{B}$ may be written as a system of explicit equations which describe the evolution of the magnetic field. The HDS is therefore given by

$$\mathbf{B}_x^{n+1} = \mathbf{B}_x^n - \tau(\mathbf{G}_{xy}^n \mathbf{B}_y^n + \mathbf{G}_{xz}^n \mathbf{B}_z^n) \quad (3.51)$$

$$\mathbf{B}_y^{n+1} = \mathbf{B}_y^n - \tau(\mathbf{G}_{yz}^n \mathbf{B}_z^n + \mathbf{G}_{yx}^n \mathbf{B}_x^{n+1}) \quad (3.52)$$

$$\mathbf{B}_z^{n+1} = \mathbf{B}_z^n - \tau(\mathbf{G}_{zx}^n \mathbf{B}_x^{n+1} + \mathbf{G}_{zy}^n \mathbf{B}_y^{n+1}) \quad (3.53)$$

where \mathbf{G}^n is the discretised form of the matrix operator \mathbf{G}_H at time step n . In matrix form, the HDS may be written as follows

$$\mathbf{B}^{n+1} = (\mathbf{I} - \alpha r_H \hat{\mathbf{k}}\hat{\mathbf{k}}\mathbf{A}_H)(\mathbf{I} - \alpha r_H \hat{\mathbf{j}}\hat{\mathbf{j}}\mathbf{A}_H)(\mathbf{I} - \alpha r_H \hat{\mathbf{i}}\hat{\mathbf{i}}\mathbf{A}_H)\mathbf{B}^n \quad (3.54)$$

where $\hat{\mathbf{i}}\hat{\mathbf{i}}$, $\hat{\mathbf{j}}\hat{\mathbf{j}}$ and $\hat{\mathbf{k}}\hat{\mathbf{k}}$ are dyadics formed from the unit vectors $\hat{\mathbf{i}}$, $\hat{\mathbf{j}}$, and $\hat{\mathbf{k}}$.

The eigenvectors of the HDS evolution operator are given by

$$\mu_1 = 1 \quad (3.55)$$

$$\mu_{2,3} = 1 - \frac{1}{2}g \pm \frac{1}{2}\sqrt{g(g-4)} \quad (3.56)$$

where $g = (\alpha r_H)^2(\zeta^2 - \alpha r_H \zeta_x \zeta_y \zeta_z)$.

For this evolution operator to be stable it is required that

$$0 \leq g \leq 4 \quad (3.57)$$

The most restrictive condition is obtained from $\mathbf{b} = (1/\sqrt{3})(1, 1, 1)$ with $\omega = (2\pi/3)(1, 1, 1)$ and related points of symmetry. By using this condition and N_{HDS} substeps per full timestep, the following stability limit is found

$$\bar{\tau}_H^{HDS} \leq N_{HDS} \frac{4}{\sqrt{27}} \sqrt{1 + \eta^2} \quad (3.58)$$

Similar to the super-time-stepping method, the Hall diffusion scheme is first order accurate in time and must be extended using Richardson extrapolation to ensure second order temporal accuracy (O’Sullivan and Downes, 2007).

Thus far, cases in which either purely Hall or ambipolar diffusion dominates have been studied. For the integration of both ambipolar and Hall diffusion terms, the effective stable time limit may be calculated to be

$$\bar{\tau}^{HDS/STS} = \begin{cases} \bar{\tau}_H^{HDS}, & \text{if } \eta \leq \eta^* \\ \bar{\tau}_A^{STS}, & \text{Otherwise} \end{cases} \quad (3.59)$$

where η^* is the solution of $\bar{\tau}_H^{HDS} = \bar{\tau}_A^{STS}$ and depends on the user defined parameters ν , N_{STS} , and N_{HDS} .

3.4 Accretion Disk Model

HYDRA solves the multifluid MHD equation on a Cartesian computational grid. Cartesian grids have been used extensively in the study of the MRI using local shearing-box type simulations (Hawley et al., 1995a; Lees and Edwards, 1972), where curvature effects associated with the circular motion of disk material about the central object are ignored. This may be done as the computational domain is built around a fiducial point which is positioned far out in the disk and its size is very small compared to the radial distance of the fiducial point from the rotation axis. Shearing box models have been used extensively in the study of accretion disk physics, due to the low computational expenditure. It has been shown that the results obtained from such simulations may not be reliable and results obtained may not be directly applicable to physical accretion disks (Regev and Umurhan, 2008). For example, in global accretion disks the structure of the magnetic field is determined by the global disk dynamics but in local simulations the structure of the initial magnetic field is chosen arbitrarily. The dependence of the results upon the box size also raises concerns over some results obtained previously (Bodo et al., 2008).

The accretion disk models used in this work are global in the sense that

the computational domain covers a very large portion of the disk. The computational domain has cylindrical symmetry. The z -component of gravity and self-gravity are ignored. Implementing such models on Cartesian grids may seem impractical as radial boundary conditions can be non-trivial. An inner boundary must be implemented at the radial boundaries which means that a portion of the computational domain is redundant and inactive. The implementation of these boundaries means that conservation of angular momentum can be compromised unless any angular momentum lost or gained through these boundaries is tracked. Difficulties arise especially at the inner radii of the disk where the fluid velocities are quite high and higher accretion rates are present, however this is also true of cylindrical grids.

There are some advantages to this approach, not least of which is the efficiency with which parallelisation can be implemented. It may also be noted that Cartesian geometry does not suffer from the variability of resolution with radius that is sometimes seen with cylindrical and spherical grids.

3.4.1 Computational Domain

To save computation time, only a quarter of the accretion disk is simulated. The accretion tori simulations of Hawley (2001) showed that using a restricted azimuthal domain does not significantly change the properties of the accretion disk at saturation quantitatively. A maximum difference of 10% was seen in the magnetic and fluid stresses between global and quasi-global (quarter-disk) simulations. A similar analysis is carried out for the accretion disk model presented here to ensure that the reduced azimuthal domain has minimal influence on the quantitative results. This analysis is presented later in this section.

Fig.3.1 shows a schematic of the computational domain used to implement the quarter disk model. The upper right quadrant of the disk is the extent of the disk simulated. Mass which flows through one azimuthal boundary of this domain will re-enter through the opposite azimuthal boundary and vice-versa. This arrangement is similar to standard periodic boundaries, the difference is that the vector quantities must be rotated through 90° . See section 3.4.3 for a detailed explanation of the boundary conditions of the computation box along with the interior radial boundaries.

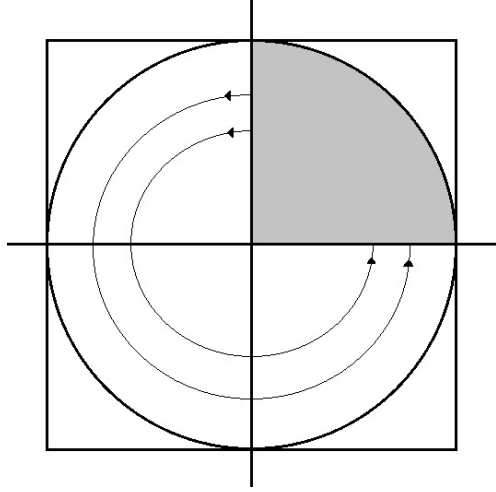


Figure 3.1: Illustration of computational domain and boundary conditions. The upper right hand quadrant is the actual computational domain. The box surrounding this quadrant represents the extent of the Cartesian grid with the accretion disk (circle) embedded within the box. The arrows represent the azimuthal periodic boundaries. Material which leaves through the low- x_1 boundary will re-enter through the low- x_2 boundary and vice-versa.

3.4.2 Gravity

A Newtonian gravitational potential is applied to the fluid within the computational domain

$$\Phi = -\frac{GM}{r} \quad (3.60)$$

where G is the universal constant of gravitation, M is the mass of the central object, and r is the distance from the central mass given by

$$r = \sqrt{x^2 + y^2} + c \quad (3.61)$$

where c is a softening parameter. Notice that this gives a cylindrical potential, where the fluid is attracted to a pole whose center is located at $x = y = 0$ rather than a single point. Thus, a density stratification is not seen in this work. The vertical extent of the disk model is small compared to the radial domain size but large enough that vertical structure in the densities and

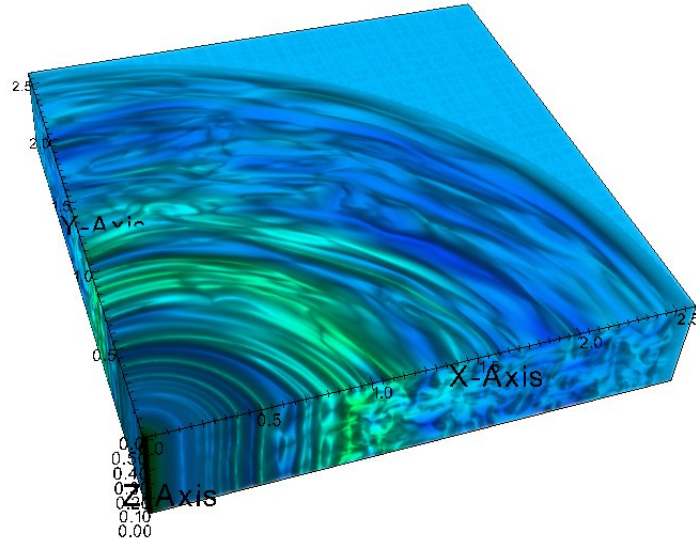


Figure 3.2: Colour plot of the neutral density using the quarter disk model. The direction of flow is in the anti-clockwise direction. Material that flows through the low- x_2 boundary flows back into the computational domain through the low- x_1 boundary.

magnetic field may develop without influence from the vertical boundaries.

3.4.3 Boundary Conditions

The choice of boundary conditions is non-trivial for the quarter disk model. Badly chosen boundaries can introduce spurious effects into the computational domain leading to unphysical results. Fig.3.2 shows a colour gradient plot of the computational domain used in the quarter disk model.

In the literature, there are two types of boundaries used in the cylindrical disk in a Cartesian box model, they are box-face and interior boundary conditions. The box-face boundaries are applied to the sides of the computational box in which the disk is situated. The interior boundaries are placed inside this box to take into account the cylindrical nature of the disk. Outside of the cylindrical disk, the fluid variables are not allowed to evolve and are essentially frozen. The fluid is allowed to flow in and out of these interior boundaries. These two types of boundaries will now be described in turn.

Box-face boundaries: The box-face boundaries are applied to the sides

of the computational box. The upper and lower z boundaries are simply periodic as there is no vertical gravity gradient. This ensures that no mass or energy is lost through the vertical boundaries. The upper x and y boundaries are unimportant as they are directly adjacent to the frozen zone. No fluid crosses these boundaries and they can simply be ignored. The lower x and y boundaries are periodic with each other. Fluid that flows out of one boundary is transported across the other. This allows and is consistent with the use of the quarter disk approximation mentioned at the beginning of this section.

Interior boundaries: The accretion disk itself is a quarter cylinder which is placed in a flattened square prism. This sets a limit to the radial extent of the disk i.e. $r \leq L_x$. This condition makes it necessary to introduce an interior radial boundary. As mentioned previously, a frozen region is introduced for $r \leq r_{int}$ and $r \geq r_{ext}$ where the dynamical equations are not evolved for the fluids or the magnetic field. In the models presented here $r_{int} = 0.5$, $r_{ext} = 2.58$ and $L_x = L_y = 2.6$ and $L_z = 0.075 \times L_x$. The inner bufferzone is positioned just outside the inner frozen zone at $0.5 < r < 0.6$, similarly the outer bufferzone is positioned at $2.48 < r < 2.58$. Fig.3.3 shows the position of these zones relative to the box boundaries. The purpose of the radial buffer zone is to smoothly transition the fluid parameters so that any numerical instabilities associated with the abrupt jump from free to frozen regions may be avoided (Lyra et al., 2008). There is a dual purpose to this type of inner boundary. It allows an escape route for undesirable waves at the beginning of the simulation. In the models presented here, spurious waves are seen to originate from the frozen region at the beginning of the simulations, these settle quite quickly. If the wavekilling boundaries were not present these waves could reflect back and forth throughout the computational domain.

The inner buffer zone needs to be able to kill waves faster as the fluid is much more dynamical here, the risk of introducing instabilities through this boundary is much more likely. It is worth noting that Lyra et al. (2008) performed some simulations without this inner boundary and models with and without inner radial boundaries behave similarly with little quantitative difference. A smaller timestep results as the fluid will be rotating at a much higher rate closer to the origin than at the inner radial edge of the bufferzone.

The bufferzone drives the fluid parameter X gradually and smoothly to its initial condition such that

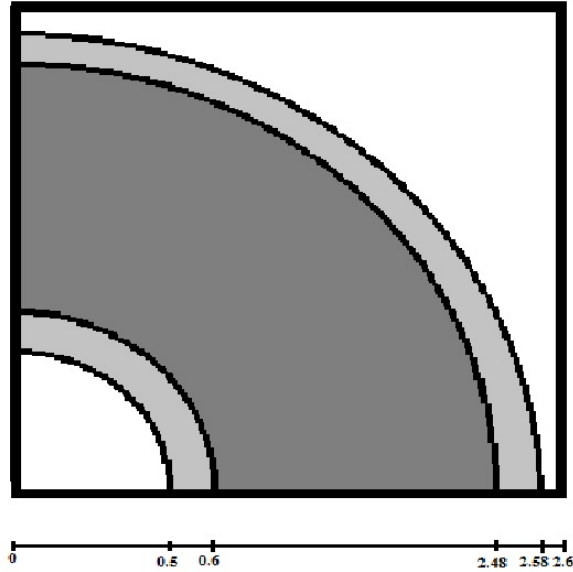


Figure 3.3: Schematic showing the x,y plane of the computational domain. The dark shaded area is the active computational domain. The white areas bounded by the black curves and the sides of the box are the frozen regions. The light shaded regions are the wavekilling interior boundaries.

$$\frac{dX}{dt} = \frac{X - X_0}{\tau} S(r) \quad (3.62)$$

where $S(r)$ is the driving function and τ is the orbital period at the boundary in question. Linear and non-linear functions were evaluated for the driving function. It was decided to use a linear driving function as no quantitative difference was found between the linear and non-linear functions. The function $S(r)$ has a range of $[0,1.0]$, it has a value of 1.0 at the boundary of the bufferzone and frozen zone and a value of 0 at the boundary of the bufferzone and the active computational domain.

3.4.4 Initial conditions

For the ideal MHD model the following initial conditions are used. The neutral density is uniform initially and is set to 1.0 in code units. The average mass of the neutral particles is taken to be $m_n = 2.33m_p$, where m_p is the mass of a proton. This corresponds to a fluid of 90% molecular hydrogen and

10% atomic helium by number, which is representative of molecular clouds. There is no pressure gradient initially. All models presented are isothermal and the neutral pressure is found using the isothermal relation $c = \sqrt{P/\rho}$.

The choice of an appropriate model for the study of the MRI is not trivial. From linear analysis (Balbus and Hawley, 1991) of the MRI it is found that only a weak magnetic field, and differential rotation is required for the MRI to be present. In numerical simulations, it is necessary that the processes involved in an instability be adequately resolved by the computational grid. In the case of the MRI, it is found from linear analysis that a critical vertical wavelength must be resolved (Balbus and Hawley, 1991, 1998), this was found to be

$$\lambda_c = \frac{2\pi v_A}{\sqrt{3} \Omega} \quad (3.63)$$

where v_A is the Alfvén speed which is given by

$$v_{Az} = \frac{B_z}{\sqrt{\mu_0 \rho}} \quad (3.64)$$

The critical wavelength of the MRI is approximately the distance an Alfvén wave would travel vertically in a single orbital period. The model must be constructed while considering the requirement that this critical wavelength be resolved either initially or become resolved through the use of perturbation at an appropriate time. An initial magnetic flux of 50mG is chosen. Magnetic fields are known to reach a strength of an order of a 1G in the region of interest in this work (Konigl and Ruden, 1993).

The critical wavelength of the MRI using this initial value of magnetic flux is resolved by 12 cells at the outer radii when using the finest resolution. At $r = 1.0$ the critical wavelength is marginally resolved but becomes resolved quite soon after the fluid perturbation is applied.

The densities for the charged species are much smaller than the neutral species as the plasma is weakly ionised. The ion fluid represents an average of ions produced from a number of metal atoms, including Na, Mg, Al, Ca, Fe and Ni. These metals have sufficiently similar ionisation and recombination rates, and so can be modelled collectively as ions of a single positive charge

$+e$ (Umebayashi and Nakano, 1990). The molecular ions, of which HCO^+ is the most numerous, are significantly less abundant than the metal ions, allowing us to neglect them. An average mass of $m_{ion} = 24m_p$ is assigned to the particles of the ion fluid, approximately equal to that of a magnesium ion.

An ionisation fraction of approximately 4×10^{-11} is expected in the radial range studied in this work. The number density of the neutral fluid is expected to be roughly $7 \times 10^{12} \text{cm}^{-3}$ (Salmeron and Wardle, 2003). The ionisation fraction (ζ) is given by $\zeta = n_e/n_H$ and so given the above information will give a number density for the electron fluid of approximately 300cm^{-3} .

The charge to mass ratio's are calculate as follows,

$$\alpha_{ion} = \frac{+e}{m_{ion}} = \frac{1.6 \times 10^{-19} \text{C}}{24m_p} = 4.0 \times 10^3 \text{g}^{-1} = 1.2 \times 10^{13} \text{statCg}^{-1} \quad (3.65)$$

$$\alpha_e = \frac{-e}{m_e} = \frac{1.6 \times 10^{-19} \text{C}}{m_e} = -5.27 \times 10^{17} \text{statCg}^{-1} \quad (3.66)$$

The number density of the ion fluid is then found using the charge neutrality condition

$$\alpha_{ion}\rho_{ion} + \alpha_e\rho_e = 0 \quad (3.67)$$

The ion density, ρ_{ion} , is then found to be $1.2 \times 10^{-20} \text{g cm}^{-3}$.

The importance of the multifluid effects are set through the collision coefficients. Collisions between the charged fluids are not considered. The rate coefficient for the ion fluid may be found in Wardle and Ng (1999). The collisional coefficients are found thus

$$K_{ion,n} = \frac{\langle \sigma \nu \rangle_{ion}}{m_{ion} + m_n} = \frac{1.6 \times 10^{-19} \text{cm}^3 \text{s}^{-1}}{24m_p + 2.33m_p} = 3.64 \times 10^{13} \text{cm}^3 \text{g}^{-1} \text{s}^{-1} \quad (3.68)$$

$$K_{e,n} = \frac{\langle \sigma \nu \rangle_e}{m_e + m_n} = \frac{1.15 \times 10^{-15} \left(\frac{128 K_B T_e}{9 \pi m_e} \right)}{m_e + 2.33 m_p} = 2.88 \times 10^{15} \text{cm}^3 \text{g}^{-1} \text{s}^{-1} \quad (3.69)$$

All simulations performed use a reduced azimuthal domain (see section 3.4.1) except for those that were used in the validation of this approach. A dimensionless unit system is used, similar to that used in the simulation of Lyra et al. (2008). The following section contain a derivation of the code units and the corresponding physical units for the fluid parameters.

3.4.5 Units

Dimensionless units are considered where

$$GM = \rho_0 = \mu_0 = 1 \quad (3.70)$$

The unit of time is then given by the inverse of the angular velocity at r_0 so that

$$t = \Omega^{-1} = \left(\frac{V_k}{r_0} \right)^{-1} = \left(\frac{GM}{r_0^3} \right)^{-1/2} \quad (3.71)$$

where V_k is the Keplerian velocity at a radius r_0 .

The unit of velocity is given by

$$|\mathbf{u}| = \frac{x}{t} = r_0 \Omega_0 \quad (3.72)$$

The unit of magnetic field is derived finally from the definition of the Alfvén speed to give

$$|\mathbf{B}| = \Omega_0 r_0 \sqrt{\mu_0 \rho_0} \quad (3.73)$$

The scale for this set of dimensionless units is then chosen by setting the lengthscale. As in Lyra et al. (2008) we set this to 5.2AU, which is the length

of the semi-major axis of jupiters orbit around the sun. The initial density is also chosen to be $\rho_0 \approx 1.0 \times 10^{-11} \text{ g/cm}^3$, which is what is expected in this region from observations. The central mass M is assumed to be a solar mass. This will allow direct comparison later to the quantitative results obtained in this study in the Ideal MHD framework. The soundspeed is chosen to be $8.04 \times 10^4 \text{ cm s}^{-1}$. This soundspeed corresponds to a disk temperature of 130K, which is typical in accretion disks of this size at a radius of 5AU (Salmeron and Wardle, 2003). This soundspeed is in the range of that used in Lyra et al. (2008). The remaining physical units associated with the dimensionless set can now be found.

If r_0 is chosen to be 1, the unit of time is found in code units to be 2π . The unit of velocity is the Keplarian velocity at r_0 and may be calculated as follows:

$$|\mathbf{u}| = \sqrt{\frac{(6.67259 \times 10^{-8}) (1.99 \times 10^{33})}{7.8 \times 10^{13}}} = 1.31 \times 10^6 \text{ cm s}^{-1} \quad (3.74)$$

The unit of time can now be found

$$t = \Omega^{-1} = \frac{r_0}{V_k} = \frac{7.8 \times 10^{13}}{1.31 \times 10^6} = 5.95 \times 10^7 \text{ s} \quad (3.75)$$

The units for magnetic field can be found to be

$$|\mathbf{B}| = \Omega_0 r_0 \sqrt{\rho_0} = 1.31 \times 10^6 \sqrt{1.0 \times 10^{-11}} = 5.8 \text{ G} \quad (3.76)$$

Typical length scales are associated with the non-ideal terms. Ohmic dissipation was determined to be unimportant compared to the Hall and ambipolar terms from initial studies as the Ohmic resistivity remains relatively small compared to the Hall and ambipolar resistivities.

From the initial conditions it is possible to get an estimate of the length scales for the Hall effect and ambipolar diffusion and compare these to the characteristic lengthscale of the system.

The Hall term becomes important when the ion inertial length becomes comparable to the characteristic length scale given by

$$L_H = \frac{c}{\omega_{pi}} \frac{v_A}{V_0} \quad (3.77)$$

where ω_{pi} is the ion plasma frequency, c is the speed of light, v_A is the Alfvén speed given by $v_A = B/\sqrt{4\pi n_i m_i}$, and V_0 is the characteristic speed of the flow which in this case is the orbital speed Mininni et al. (2003).

Using the initial conditions at $r=2.0$, the Hall scale (L_H) is calculated to be 8.89×10^8 cm. In comparison, the cell spacing in the simulations vary from approximately 0.1 to 0.03 AU or 1.62×10^{12} cm to 4.05×10^{11} cm. It is clear that the Hall scale is much less than the grid scale initially. However, once the MRI begins to become active the magnetic field strength will amplify, also turbulence in the ionised species causes the ion density to have a wide distribution about the mean ion density and so locally the Hall scale can and does reach the same order of magnitude of the grid scale.

In the case of ambipolar diffusion, typical length scales are approximately given by

$$L_{AD} = \frac{B^2}{4\pi \rho_i \rho_n K_{ion,n} V_0} \quad (3.78)$$

where ρ_i and ρ_n are the ion and neutral fluid densities respectively, $K_{ion,n}$ is the ion-neutral collisional frequency and V_0 is the characteristic velocity of the flow (Oishi and Mac Low, 2006). Initially, as in the Hall case, the length scale associated with ambipolar diffusion is much smaller than the grid scale. At $r=2.0$, L_{AD} is calculated to be 6.18×10^8 cm using the initial conditions. By examining the properties of regions of the disk at the same radius once the MRI has saturated, the ambipolar length scale is found to be in the range $0.01 \Delta x \leq L_{AD} \leq 10 \Delta x$.

Chapter 4

Resolution Study

To ensure that the physical processes involved with the MRI are well resolved and that the solution is well converged, a resolution study is carried out. It has been explained that the validity of the ideal MHD framework depends on a number of conditions, one of which is the length scales involved with diffusion are much smaller than the spatial resolution of the numerical model and that the time scales involved must be much longer than the typical timestep seen in any simulations. Once multifluid effects are included it is then important that these scales are resolved sufficiently to ensure that small scale effects are taken into account.

This resolution study involves running a series of simulations which are identical to each other except for the spatial resolution used. The timestep for each run is subject to a Courant condition and so the timestep will decrease as the resolution increases. Each simulation is then analysed by calculating a number of different parameters which describe certain aspects of the flow. These techniques will be described in section 4.1. Sections 4.3 and 4.4 contain the results for the ideal and multifluid resolution studies.

The robustness of the quarter disk model is also tested in section 4.2 where identical simulations are run differing only in the extent of the azimuthal domain.

4.1 Analysis techniques

A number of parameters are used in the resolution study to compare the solution of each resolution used in the resolution study. These will be used to ensure that convergence has occurred in both the ideal and multifluid cases, and more specifically in the multifluid case it should show if diffusive effects are being resolved.

4.1.1 Magnetic and Kinetic Stresses

The stresses associated with the differential rotation, that is typical in accretion disks, are commonly studied parameters. These are the Reynolds (fluid) and Maxwell (magnetic) stresses. The Maxwell stress is the most important in the study of the MRI as the magnetic stress mediates the MRI process. In accretion disks, both wavelike and turbulent disturbances can create tight radial-azimuthal correlations in the fluctuations in the velocity and magnetic fields (Balbus, 2003), the $r - \phi$ component of the stress is associated with the viscous torque that provides the angular momentum transport, therefore the $r - \phi$ component of the stresses is an important parameter to observe in both local and global simulations involving the MRI and give a good indication as to the magnitude of angular momentum transport present. The $r - \phi$ component of the stresses may be represented together as the sum of the Reynolds and Maxwell stresses

$$T_{r\phi} = \overline{\rho\delta V_r\delta V_\phi} - \overline{\delta B_r\delta B_\phi} \quad (4.1)$$

where $T_{r\phi}$ is the $r - \phi$ component of the total stress tensor, and δB denotes the fluctuating component of the magnetic field and is given by

$$\delta\mathbf{B}_x = \mathbf{B}_x - \overline{\mathbf{B}_x} \quad (4.2)$$

where x represents either the radial or azimuthal component of the magnetic field.

In the case of the fluctuating part of the velocities (δv), the Keplerian velocity field at the radius at which the sampled fluid element is found to be

$(\overline{v_k})$ is first subtracted and then the fluctuating component is found to give

$$\delta \mathbf{v}_x = \mathbf{v}_x - \overline{\mathbf{v}_k} \quad (4.3)$$

Another important quantity that is used in MRI studies is the anomalous viscosity which is parametrised by the α parameter (Shakura and Sunyaev, 1973) where

$$\alpha = \alpha_R + \alpha_M \quad (4.4)$$

where α_R and α_M are the kinetic and magnetic components of the anomalous viscosity and are given by

$$\alpha_R = \frac{\overline{\rho \delta V_r \delta V_\phi}}{\rho c_s^2} \quad (4.5)$$

$$\alpha_M = -\frac{\overline{\delta B_r \delta B_\phi}}{\rho c_s^2} \quad (4.6)$$

where c_s is the isothermal sound speed.

In this resolution study, only the Maxwell stress and the alpha parameter will be calculated for the purpose of showing convergence of the solution, the Reynolds stress will be neglected. In practice, the Reynolds stress can be problematic to calculate due to the very small mean radial component in the velocities and so in practice can be very noisy. Since both the Reynolds and Maxwell stresses are components of the total stress so one may be neglected in favour of the other.

When calculating the stresses, a small region adjacent to the inner and outer boundaries is ignored. The inner boundaries are seen to cause some undesirable effects close to their edges, the inner boundary was removed in one simulation and the evolution of the fluid was shown to be consistent with a simulation with the inner boundary included. The same could not be done with the outer boundary due to the fluid simply flowing out of the grid if the frozen zone is not present.

4.1.2 Magnetic and Kinetic Energies

Other parameters that are useful to compare are the temporal evolution of the magnetic and kinetic energies. The total kinetic energy itself is not particularly useful apart from showing that the total energy of the system does not change much over the time simulated. This is allowed due to the choice of boundary conditions which allow inflow (into the grid) of mass and kinetic and magnetic energy. In practice however, the flow on to the grid closely matches the outflow of mass and energy out of the grid and so the increase/decrease of mass and energy over the lifetime of these simulations is very small. Instead, the perturbed kinetic energy is used for comparison purposes and is given by

$$E_k = \int \int \int \frac{1}{2} \rho [\delta \mathbf{v}^2 - \mathbf{v}_k^2] dx dy dz \quad (4.7)$$

where \mathbf{v}_k is the Keplerian velocity.

The total magnetic energy is important to follow as it is expected to grow as the stretching and twisting of the magnetic field due to fluid motions extracts kinetic energy from the flow. The total magnetic energy is given by

$$E_M = \int \int \int \frac{1}{2} \mathbf{B}^2 dx dy dz \quad (4.8)$$

in cgs units.

For comparison, the mean of the Maxwell stress, α parameter, and energies is calculated for each of the resolutions studied. To be consistent, each simulation is allowed to reach saturation. The mean is then taken from this point for the same number of orbital periods at $r = 1.0$. This period is different for the ideal and multifluid resolution studies. Saturation does not occur at the same time (relative to the perturbation injection) for each resolution so this method is required. Convergence is assumed to have occurred if the mean of a given parameter at saturation for two resolutions differ by no more than 10%. This value is chosen because it is less than the standard deviation for any given run in the resolution study.

4.2 Comparison Between Global and Quarter disk approaches

To understand whether the use of a computational domain which contains only a quarter of the azimuthal range of the accretion disk is a viable approach, a direct comparison is run. Two simulations are ran, one simulating a quarter disk and another simulating a full accretion disk. To do this, a simple accretion disk is modelled with an initially vertical magnetic field threading the disk, with an initial field strength strong enough to lead to MRI driven turbulence and weak enough to ensure that the MRI is allowed to develop. No pressure gradient is present and the disk is rotationally supported. The extent of the disk is similar to that seen in the production runs. Refer to section 3.4.4 for details of the initial set-up. The total magnetic and perturbed kinetic energies are compared over a number of orbits.

The disk is allowed to evolve for a total of 10 orbits at a radius of 1.0 initially to allow the fluid to settle down. This settling down period ensures that any undesirable waves in the fluid parameters are given sufficient time to attenuate and/or leave the computational domain through the radial boundaries.

The disk was allowed to settle for 10 orbits, the disk fluid is perturbed with a maximum perturbation amplitude of 0.1% of the Keplarian velocity and allowed to evolve for a further 10 orbits to ensure that saturation of the magnetic field is reached. The same procedure is followed for the kinetic energies.

The mean total magnetic energy is calculated for both models. The total magnetic energy in the global model compares well to the quarter disk model showing a similar evolution over a time interval of 40 orbital periods at $r=1.0$ (See Fig.4.1). However, the total magnetic energy in the global disk case shows more variation over time compared to the quarter disk case, this is due to the extra modes of the MRI allowable in the full disk simulation. Both cases have quite similar profiles and don't diverge significantly during the first 30 orbits which were considered, the solution does seem to diverge slightly in the final 10 orbits. The time period studied here is very long compared to that used in production simulations. It is not necessary for

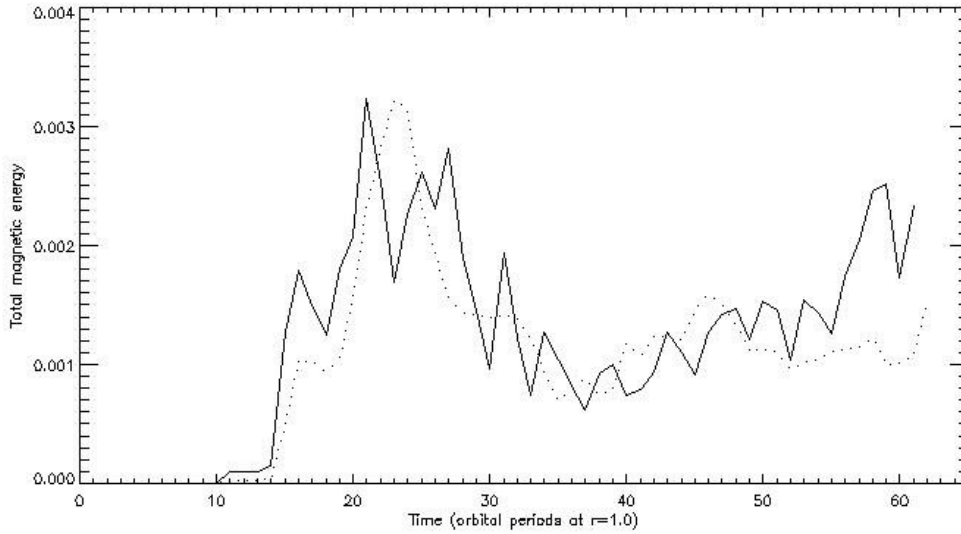


Figure 4.1: Comparison of total magnetic energy for the global disk (solid line) and quarter disk (dashed line).

production simulations to run for this length of time as they reach saturation very quickly after perturbation injection. The divergence of the Magnetic field was analysed in both cases to ensure that the radial boundary condition were not influencing the magnetic field evolution and was found to be very small.

The total perturbed kinetic energy profiles are very similar (see Fig.4.2), growth occurs at roughly the same time and they do not diverge very much throughout the duration of the simulation. The global kinetic energy is slightly higher through out the period studied. This is similar to the magnetic energy above. It is certain that the increase azimuthal domain in the global case is allowing higher saturation values but not significantly higher.

The Maxwell stress is also compared for the two models. The MHD turbulence that results from the MRI transports angular momentum through Maxwell stress. The global run shows growth earlier than the quarter disk model but they saturate at approximately the same level. The profiles are similar but show a lot of variation in time.

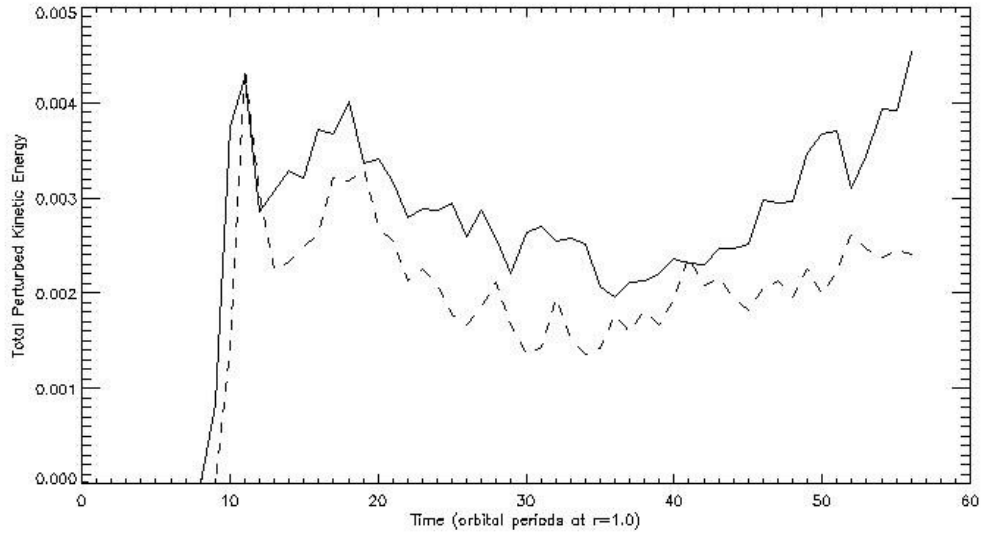


Figure 4.2: Comparison of total perturbed kinetic energy for the global disk (solid line) and quarter disk (dashed line).

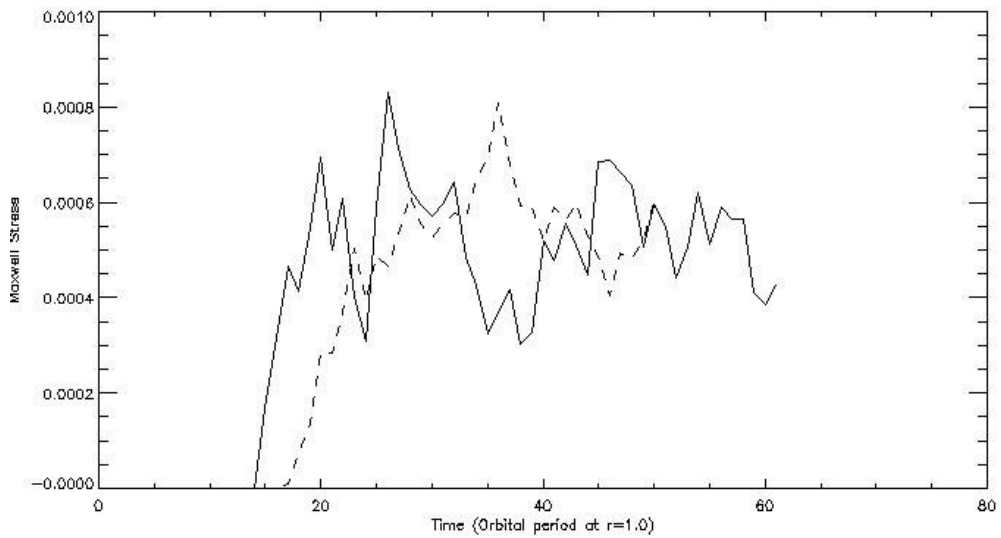


Figure 4.3: Comparison of Maxwell stress for the global disk (solid line) and quarter disk (dashed line).

Parameter	Mean	Standard Dev.
Total Magnetic Energy (global)	1.562×10^{-3}	6.493×10^{-4}
Total Magnetic Energy (quarter)	1.382×10^{-3}	5.896×10^{-4}
Total Kinetic Energy (global)	2.716×10^{-3}	5.182×10^{-4}
Total Kinetic Energy (quarter)	2.058×10^{-3}	5.331×10^{-4}
Maxwell Stress (global)	-5.422×10^{-4}	1.322×10^{-4}
Maxwell Stress (quarter)	-5.647×10^{-4}	8.312×10^{-5}

Table 4.1: Full disk Vs. quarter disk comparison.

4.3 Ideal MHD Resolution Study

The ideal MHD resolution study ensures convergence of the solution. As the resolution is increased, physical processes such as the MRI get more adequately resolved. The data obtained here may also be used to for comparison to current global MRI studies found in the literature.

The initial conditions used are outlined in section 3.4.4. The computational domain set-up along with the boundary conditions are explained in detail in sections 3.4.1 and 3.4.3 respectively. The resolutions to be examined are listed in table 4.2, starting with the coarsest resolution and ending with the finest resolution. At the finest resolution, the critical vertical wavelength of the MRI is resolved by 12 zones.

Run ID	N_x, N_y	N_z
Res1-ideal	120	9
Res2-ideal	240	18
Res3-ideal	360	27
Res4-ideal	480	36

Table 4.2: List of Resolutions Studied.

Many of the parameters used for comparison show a peak following the linear growth phase of the MRI and then typically settle down quickly about a mean value at saturation. All of the parameters show very little growth past this peak and so the mean values are calculated from a point in time that is 5 orbital periods (at $r = 1.0$) after this peak has occurred. All runs are seen to have settled about their final mean value by this time.

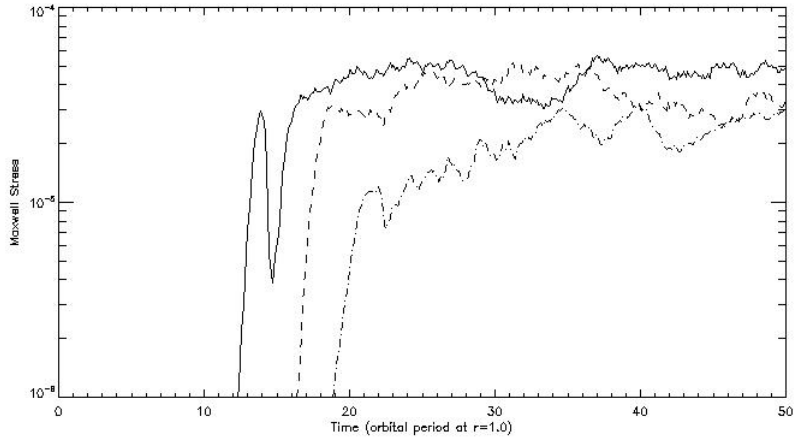


Figure 4.4: A log-linear plot of the Maxwell Stress against time (in orbital periods calculated at $r=1.0$) in the ideal case. The resolutions represented here are $N_x = 480$ (solid line), $N_x = 360$ (dashed line), and $N_x = 240$ (dotted-dashed line). The $N_x = 120$ run showed no significant growth in the Maxwell stress and is very small compared to the other cases.

4.3.1 Ideal Case: Maxwell Stress and Alpha Parameter

Once the series of runs were completed, some initial calculations were carried out to confirm the data set was complete and looked sensible in a qualitative sense. No undesirable numerical effects were seen in the radial region concerned with this study. Turbulence was seen to develop as expected in runs where the critical wavelength was resolved. All runs were examined visually to see if turbulence was maintained after the initial growth and to ensure that any divergence errors in the magnetic field were negligible. The mean Maxwell stress was then calculated for each run. The radial range of interest is from 0.8 to 2.38, the contribution to the Maxwell stress of fluid outside this region is neglected.

In Fig.4.4¹, the temporal evolution of the Maxwell stress for each of the finest three resolutions is shown on a log-linear scale. The coarsest resolution showed no significant growth and is very small compared to the finer resolutions. The initial peak mentioned previously may be seen once the linear phase ends. The time variability of the Maxwell stress is quite large

¹Note that the units of the above figure and all other figures describing the stresses and energies use the same unit system as described in section 3.4.5.

compared to the magnitude of the mean. The nature of turbulence generated by the MRI leads to quite violent fluid motions distributed throughout the height and the radial extent of the disk. Some periodicity is seen in the nature of the turbulence and the severity of the turbulence is seen to increase and decrease over time. This may be due to some secondary instability such as the the channel solution manifesting itself on the grid. There is some evidence of radial streaming near the inner boundary where regions of high magnetic energy which alternate from high to low throughout the height of the disk forces the fluid through channels where the magnetic energy is low, however the radial velocities here show very little difference from the mean values calculated.

It may be seen in Fig.4.5 and table 4.3 that the solution has converged sufficiently i.e. the difference in a certain parameter between the finer and next coarser resolution represented as a percentage of the value calculated for the finer resolution is less than 10%. The error bars represent one standard deviation about the mean. These error bars have considerable overlap for the $N_x = 360$ and $N_x = 480$ runs. The computational expenditure of the ideal runs is quite low and so it would be possible to use a finer resolution of $N_x = 640$, however, the multifluid case is much more computationally expensive and would be too computationally expensive given the resources currently available.

Run ID	Mean	Std. Dev.	% of diff. between means
Res1-ideal	-1.3510e-12	4.6926e-13	N/A
Res2-ideal	-2.5673e-5	4.3653e-6	~ 99%
Res3-ideal	-3.9488e-5	6.9339e-6	~ 35%
Res4-ideal	-4.3085e-5	7.5829e-6	~ 8%

Table 4.3: Maxwell stress results for the ideal resolution study.

A similar analysis is now performed for the alpha parameter. The alpha parameter is calculated for each of the resolutions studied using the same time intervals as for the Maxwell stress previously. The magnetic component of the alpha parameter dominates the kinetic component and therefore the profile of the evolution of the alpha parameter is similar. In Fig.4.6 the temporal evolution of the alpha parameter for the $N_x = 360$ run is plotted. The initial peak following the linear phase passes and the solution quickly

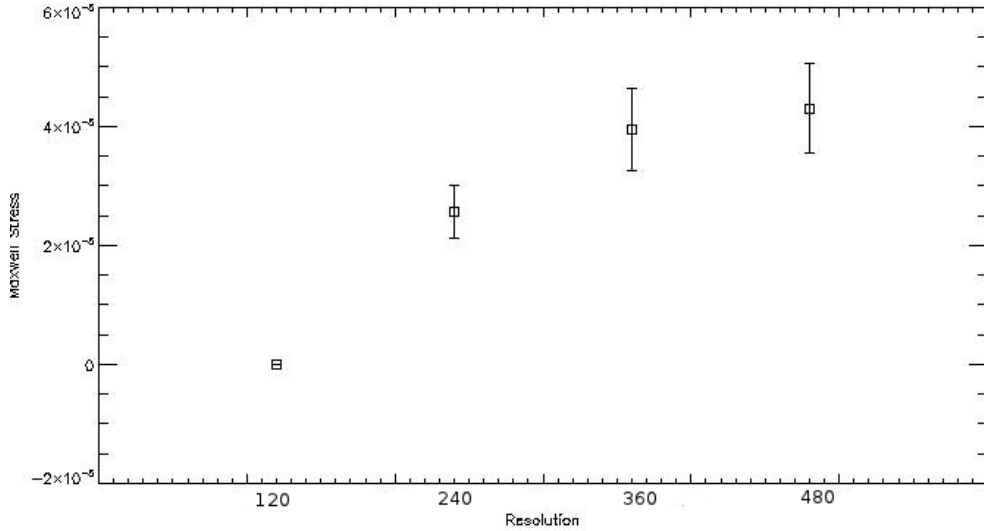


Figure 4.5: The Maxwell Stress plotted for each resolution studied. The error bars represent one standard deviation about the mean. Means were calculated from the point in time that saturation has occurred and for the same time interval in each case.

reaches saturation after the perturbation is injected. In Fig.4.7 convergence of the solution can be seen. There is considerable overlap of the error bars which represent one standard deviation. Table 4.4 contains the data from this analysis.

Run ID	Mean	Std. Dev.	% of diff. between means
Res1-ideal	-9.5455e-6	1.5584e-8	N/A
Res2-ideal	0.0118	0.0023	~ 99%
Res3-ideal	0.0254	0.0033	~ 53%
Res4-ideal	0.0280	0.0040	~ 9%

Table 4.4: Alpha parameter results for the ideal resolution study.

4.3.2 Ideal Case: Magnetic and Kinetic Energies

Convergence of the solution is now examined for the magnetic and perturbed kinetic energies. It is expected that the magnetic energy should grow as the magnetic field is stretched and twisted by the differential rotation of the accretion disk. The turbulence that develops due to the MRI leads to

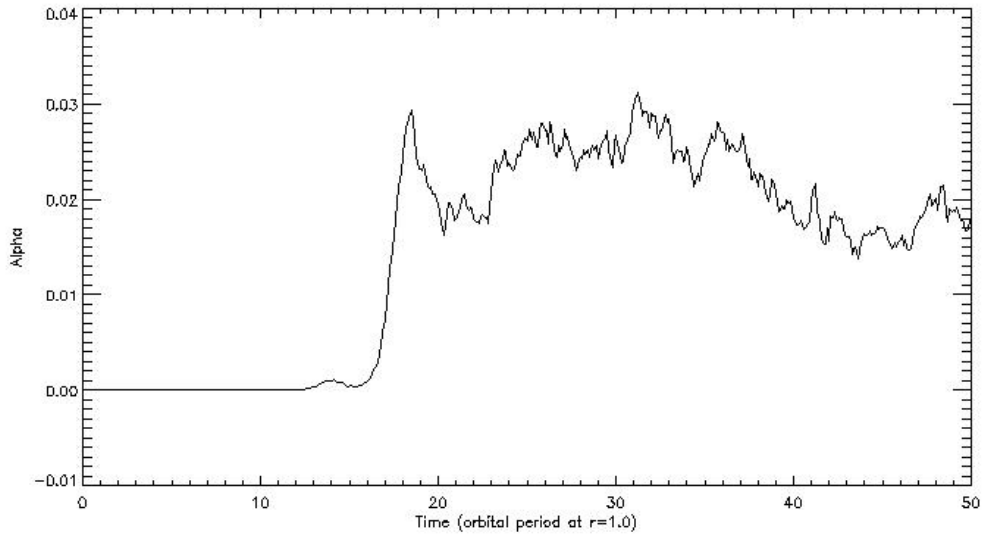


Figure 4.6: The alpha parameter for the ideal $N_x = 360$ run. There is an initial peak after the initial growth period, this is related to the structure of the perturbation causing an overshoot in the stresses. This is related to the way that the stresses are calculated.

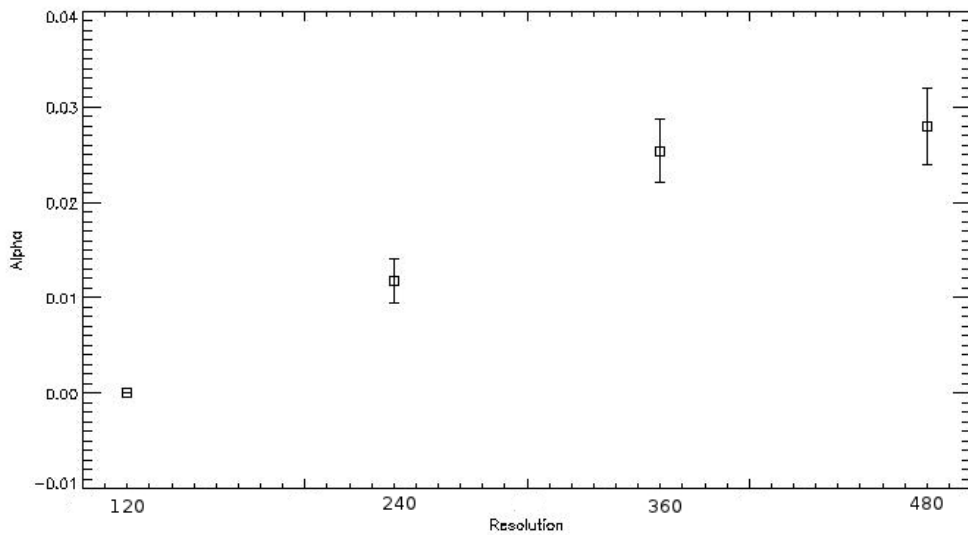


Figure 4.7: Alpha parameter plotted for each resolution studied. The error bars represent one standard deviation about the mean. Considerable overlap between the error bars can be seen for the finest resolution runs.

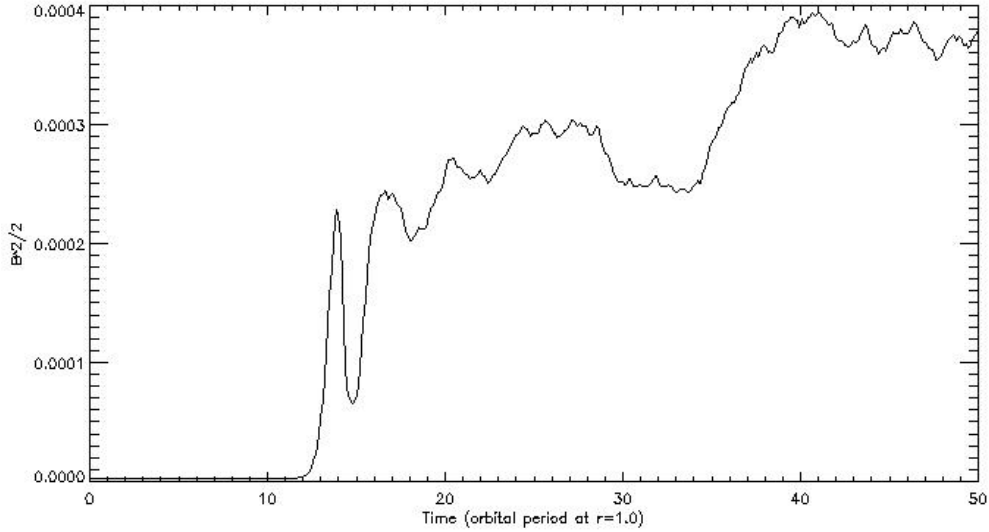


Figure 4.8: The total magnetic energy for the ideal $N_x = 480$ run. Some growth is seen after saturation is reached. This is because of the quasi-periodic profile seen in the Maxwell stress and the alpha parameter, which leads to more accretion which can cause magnetic energy to be transported onto the grid.

growth in the perturbed kinetic energy. Turbulence develops quickly on the grid (within a few orbits of perturbation injection) and increases in severity until saturation occurs. The same sample interval is used as in the stress and alpha parameter study.

Fig.4.8 shows the evolution of the total magnetic energy for the $N_x = 480$ run. It has saturated sufficiently but there is a period of extra growth approximately 20 orbits after saturation occurs. It is not clear whether these periods of growth continue after the simulation completes. The periods of growth and relaxation seen happen because of the quasi-periodic profile seen in the Maxwell stress and the alpha parameter, which leads to more accretion which can cause magnetic energy to be transported onto the grid. This is not related to the idea of bursty accretion mentioned in Romanova et al. (2011) where magnetic energy can build up in the inner disk which can halt accretion temporarily and lead to a significant build up of mass. This can then give way and lead to a burst of matter falling inwards onto the central object, no evidence is seen in the ideal MHD run of a significant buildup of magnetic energy at the inner boundary. The total magnetic energy data from this series of runs may be seen in table 4.5. Fig.4.9 shows the convergence of

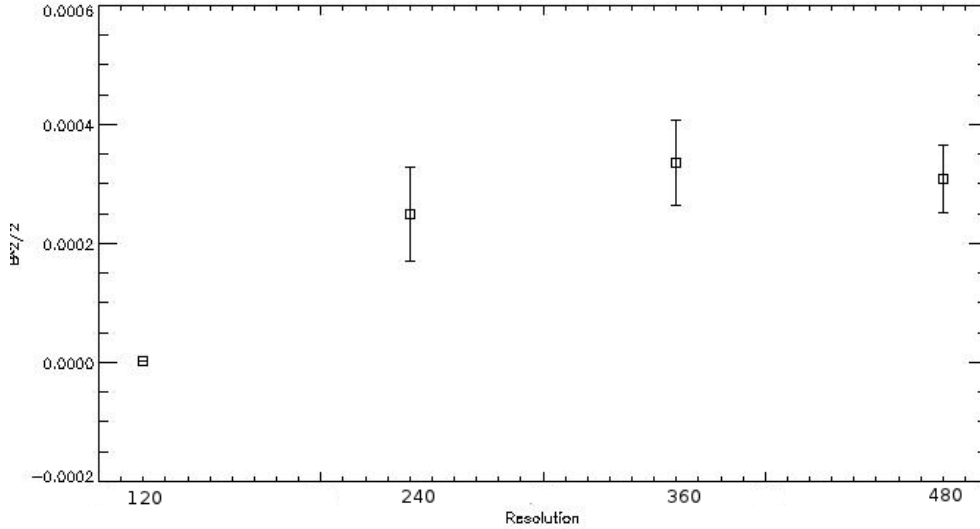


Figure 4.9: Total magnetic energy plotted for each resolution studied. The error bars represent one standard deviation about the mean.

the solution, the error bars refer to one standard deviation about the mean and again these show considerable overlap for the $N_x = 360$ and $N_x = 480$ runs. There is a slight decrease in the total magnetic energy with the finest resolution. The profiles of the total magnetic energy for these two runs follow each other closely but have a large amount of variability with time and so if a larger time interval were studied these two runs may overlap more closely.

Run ID	Mean	Std. Dev.	% of diff. between means
Res1-ideal	2.496e-6	1.443e-9	N/A
Res2-ideal	2.489e-4	7.976e-5	$\sim 99\%$
Res3-ideal	3.360e-4	7.121e-5	$\sim 26\%$
Res4-ideal	3.084e-4	5.719e-5	$\sim 9\%$

Table 4.5: Total magnetic energy results for the ideal resolution study.

The perturbed kinetic energy for the coarsest resolution showed no growth past the introduction of the perturbation so its value is not important and so is not included here. The remaining three runs show similar growth to the magnetic energy. This growth occurs due to the complex fluid motions associated with MHD turbulence generated by the MRI. Fig.4.10 show the growth and saturation of the perturbed kinetic energy for the $N_x = 480$ run. The solution has converged sufficiently as can be seen in Fig.4.11. The re-

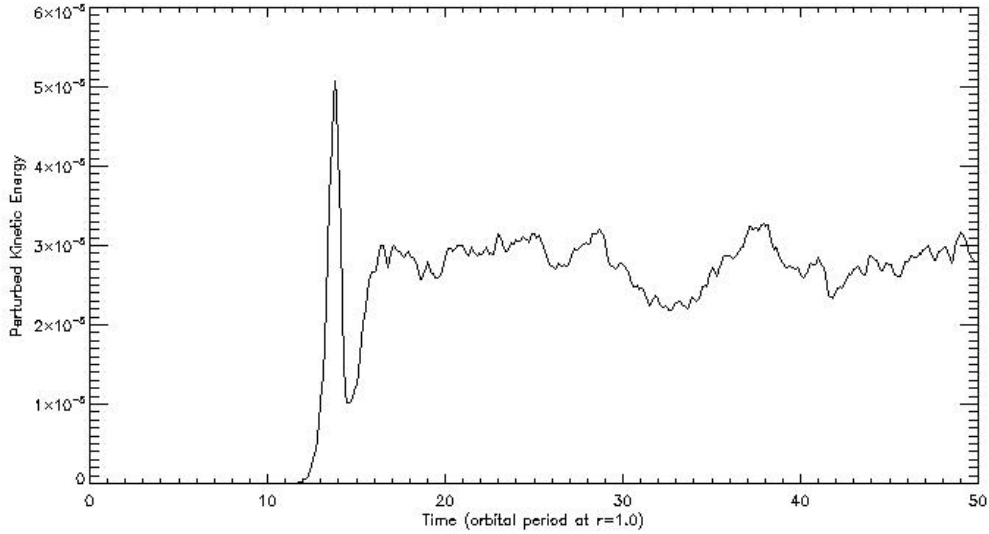


Figure 4.10: The perturbed kinetic energy for the ideal $N_x = 480$ run.

sults are summarised in table 4.6. Note that the results from the coarsest resolution are not included. The perturbed kinetic energy at this resolution is not seen to grow significantly past the point of perturbation injection.

Run ID	Mean	Std. Dev.	% of diff. between means
Res1-ideal	N/A	N/A	N/A
Res2-ideal	9.8695e-06	2.5313e-06	\sim N/A %
Res3-ideal	2.4471e-05	3.7224e-06	\sim 60%
Res4-ideal	2.7598e-05	2.7986e-06	\sim 11%

Table 4.6: Perturbed kinetic energy results for the ideal resolution study.

4.3.3 Comparisons of ideal MHD regime with previous numerical studies

The ideal model used in this study is designed to be similar to that of Lyra et al. (2008). In the model of Lyra et al, the full azimuthal range of the accretion disk is simulated and the disk model is implemented on a Cartesian grid. In some runs, non-cubic cells are used. This was done to make sure that the vertical characteristic wavelength of the MRI is adequately resolved. This step is not taken with the model used here. A number of magnetic field

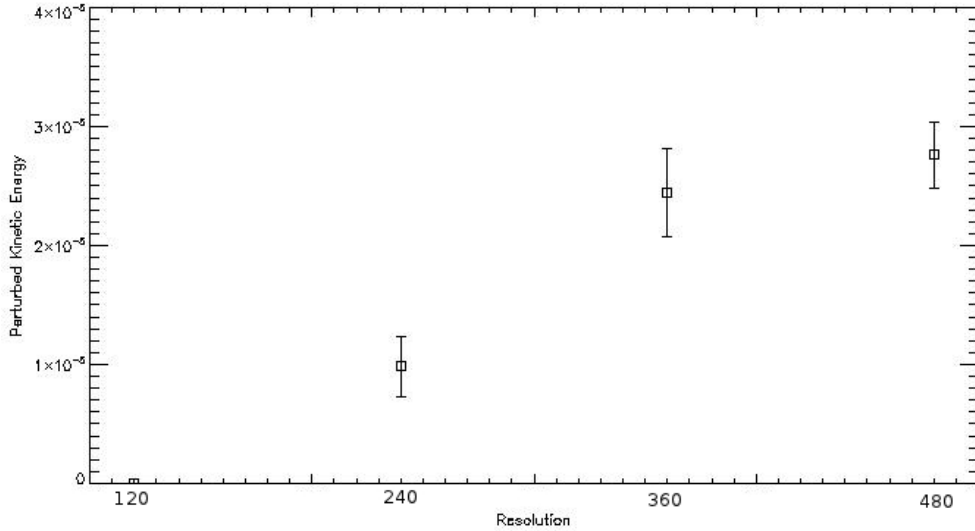


Figure 4.11: Perturbed kinetic energy plotted for each resolution studied. The error bars represent one standard deviation about the mean.

strengths and orientations are used in the above work. The initial magnetic field used in this work is within the range studied in Lyra et al. (2008) and is chosen to be 50mG. This value was chosen to ensure that the characteristic wavelength is initially well resolved in this work. The value of the soundspeed is closest to that of model A in the above paper. The boundary conditions used in the model presented here are very similar to those used by Lyra et al and are designed to behave in the same way and perform the same function such as killing spurious numerical waves and softening of the discontinuity in the solution at the edge of the frozen region.

The mean value of the Maxwell stress at saturation quoted in Lyra et al. (2008) is $-1.5 \times 10^{-5} \pm 0.3 \times 10^{-5}$. The value of the Maxwell stress averaged over 20 orbits (at $r=1.0$) post saturation for the $N_x = 480$ ideal model is $-4.3 \times 10^{-5} \pm 0.76 \times 10^{-5}$. It must be noted however that besides the differences between our model and that of Lyra et al quoted in the previous chapter, there is a large difference in resolution between the two studies. The resolution quoted for model A in Lyra et al. (2008) is $320 \times 320 \times 32$ which refer to the number of cells in the x , y , and z directions respectively. These cells cover the full azimuthal range of the disk so the equivalent resolution for our study which covers a quarter of the disk would be $160 \times 160 \times 32$. The use of non-cubic cells by the author would make a comparison here pointless without

also introducing this step. Note also that the vertical size of our disk model is $L_z = 0.075L_x$ which is smaller than that of Lyra et al where $L_z = 0.1L_x$. The closest resolution that has been run using our model is $240 \times 240 \times 18$. For this run, the mean Maxwell stress found over a time period of 20 orbits (at $r=1.0$) was $-2.6 \times 10^{-5} \pm 0.4 \times 10^{-5}$ which is more comparable but is still considerably higher. From the resolution study carried out in chapter 4 it can be seen that even with an initial magnetic field strength of 50mG, which was more than twice that of 'model A' presented in the above study, the saturation values of the stresses and energies were shown not to have yet converged. If a finer resolution was used by the authors, the mean magnetic and kinetic stresses at saturation may have been much higher, although the use of non-cubic cells in Lyra et al. (2008) may have helped to overcome this problem somewhat with the vertical modes of the MRI. Differences between the saturation magnitudes in the stresses in this work and that of Lyra et al can also be attributed to the increased magnitude of the net magnetic field used here.

Run ID	res2-ideal Mean	res2-ideal Std. Dev.	Lyra (2008) Model A Mean	Lyra (2008) Model A Std. Dev.
Maxwell Stress	-2.6e-5	0.4e-5	-1.5e-5	0.3e-5
Reynolds Stress	9.95e-06	3.3e-06	2.4e-6	0.4e-6
Alpha Parameter	1.18e-2	0.23e-2	6.9e-3	0.12e-3

Table 4.7: Comparison of the results of Lyra (2008) and the results obtained from run res2-ideal.

The Reynolds stress found using our model at a resolution of $240 \times 240 \times 18$ was calculated to be $9.95 \times 10^{-6} \pm 3.3 \times 10^{-6}$ over a similar time period as was used for the Maxwell stress. This is again larger than that reported by Lyra et al. (2008) which was quoted to be $2.4 \times 10^{-6} \pm 0.4 \times 10^{-6}$. The alpha parameter for model A in Lyra et al is reported to be approximately 0.0069 ± 0.00012 . For our $240 \times 240 \times 18$ model, the alpha parameter was calculated to be 0.0118 ± 0.0023 . It is likely that had Lyra et al performed a run with a higher resolution, in fact they would have seen stress and alpha parameter magnitudes increase correspondingly. See table 4.7 for a comparison of the results of Lyra et al. (2008) and the simulation res2-ideal from this resolution study.

In ideal studies, the alpha parameter is found to be within the range 0.1-0.001 (Hawley et al., 1995b, 1996). All values calculated here during the

resolution study and subsequent analysis of other ideal MHD simulations were within this range.

4.4 Multifluid Resolution Study

The multifluid resolution study is used to ensure that a resolution is used in production runs which adequately resolves any non-ideal effects. The initial conditions used are outlined in section 3.4.4. The computational domain set-up along with the boundary conditions are explained in detail in sections 3.4.1 and 3.4.3 respectively. The resolutions to be examined are listed in table 4.2, starting with the coarsest resolution and ending with the finest resolution. At the finest resolution, the critical vertical wavelength of the MRI is resolved by 12 zones.

This section follows the same layout and procedures as are seen in the ideal MHD resolution study in the previous section.

4.4.1 Multifluid Case: Maxwell Stress and Alpha Parameter

Here the data for the Maxwell Stress and Alpha parameter are presented for the multifluid case. These runs are the only multifluid global accretion disk simulations that are known to exist currently in the literature. Non-ideal studies such as those that use resistive and Hall MHD models have been carried out in the local shearing box framework and may be useful for comparison. Comparisons will not be made here between the ideal and multifluid cases but this will be examined later in chapter 5.

First, the mean Maxwell stress is calculated for each of the resolutions studied. Fig.4.12 and Fig.4.13 show the temporal evolutions of the Maxwell stress for the $N_x = 360$ and $N_x = 480$ cases respectively. It is interesting to see that in the $N_x = 480$ case, saturation occurs at a value that is almost an order of magnitude higher than is seen in the $N_x = 360$ case. Indeed $N_x = 480$ run shows an initial growth that closely matches the $N_x = 360$ case and shows signs of beginning to saturate but then continues to grow approximately linearly until final saturation occurs. This is an indication

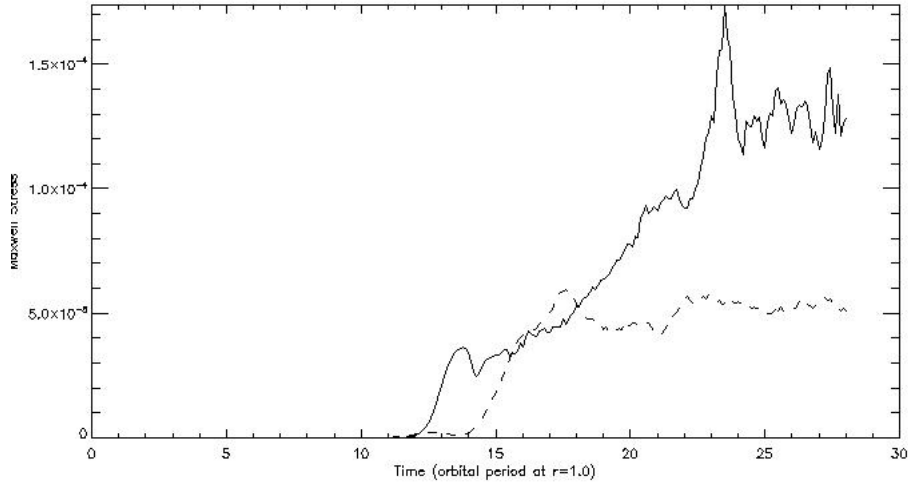


Figure 4.12: The Maxwell stress for the multifluid $N_x = 360$ (dashed line) and the multifluid $N_x = 480$ (solid line) runs.

that at this resolution, diffusive length scales are becoming important. If the convergence of the solution is followed from the lowest resolution to the highest one, it looks as if the series of simulations will converge as in the ideal case. However, the finest resolution shows a considerable jump in stress.

Run ID	Mean	Std. Dev.	% of diff. between means
Res1-mf	-3.1372e-11	1.1533e-11	N/A
Res2-mf	-3.1177e-5	1.2139e-5	~ 99%
Res3-mf	-4.9330e-5	4.6343e-6	~ 37%
Res4-mf	-1.2987e-4	7.5581e-6	~ 62%

Table 4.8: Maxwell stress results for the multifluid resolution study.

In the case of the alpha parameter, the evolution shows many of the same features of the Maxwell stress case. Fig.4.15 is a plot of the temporal evolution of the alpha parameter for the $N_x = 480$ and $N_x = 360$ cases. The $N_x = 480$ case shows an initial exponential growth phase followed by a period in which it looks like saturation may occur but the alpha parameter continues to grow linearly until saturation does finally occur towards the end of the simulation. The temporal evolution of the $N_x = 360$ case shows an evolution similar to the ideal case and with a saturation level that is similar to the ideal case at the same resolution. Multifluid effects certainly seem to have some influence on the anomalous viscosity and the stresses in general.

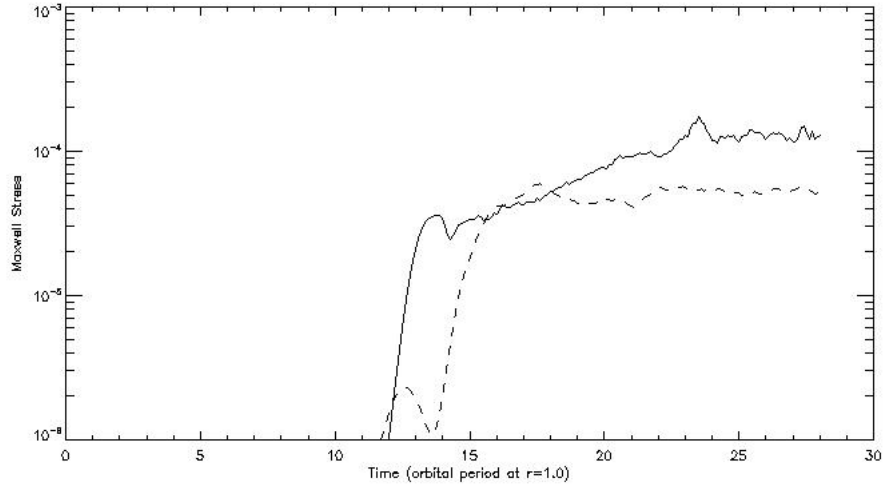


Figure 4.13: The Maxwell stress for the multifluid $N_x = 360$ (dashed line) and the multifluid $N_x = 480$ (solid line) run on a log-linear scale.

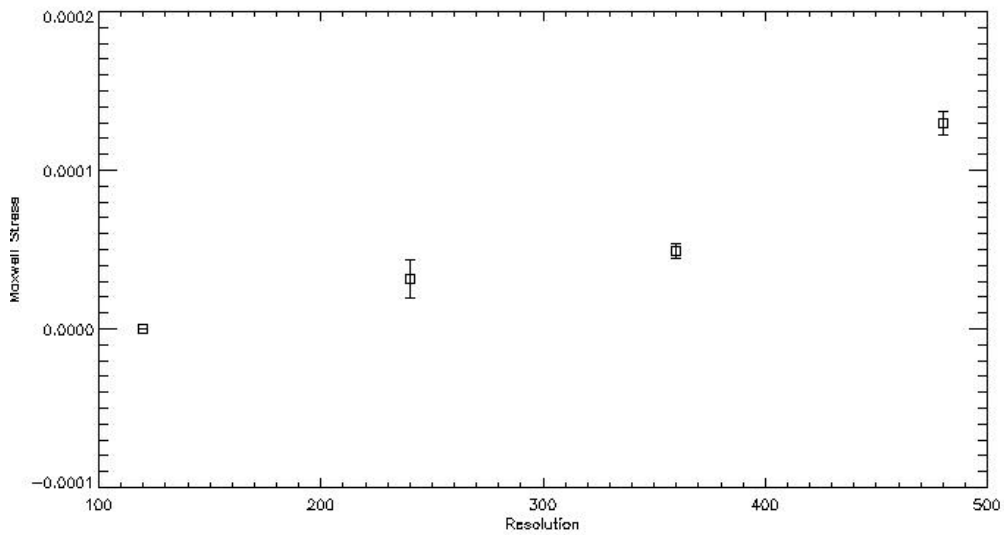


Figure 4.14: Maxwell Stress plotted for each resolution studied. The error bars represent one standard deviation about the mean.

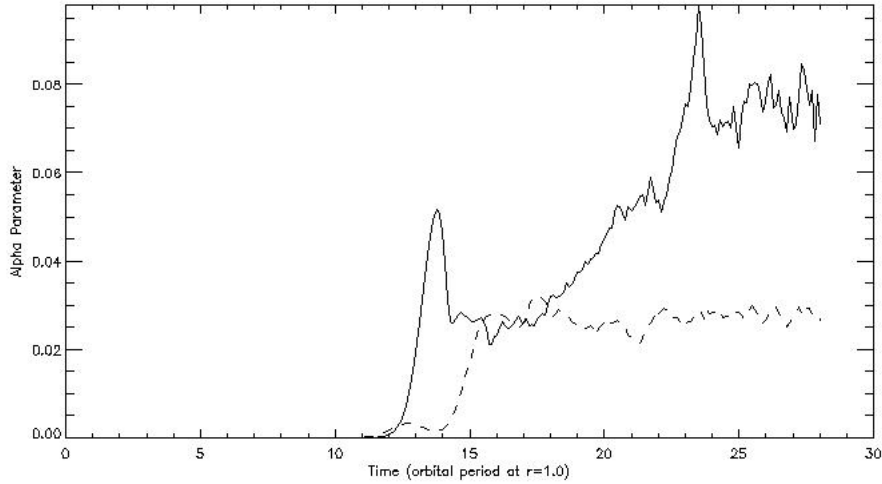


Figure 4.15: The alpha parameter for the multifluid $N_x = 480$ (solid line) and $N_x = 360$ (dashed line) runs.

The results from the alpha parameter analysis are summarised in table 4.9.

Run ID	Mean	Std. Dev.	% of diff. between means
Res1-mf	-9.4414e-5	2.3932e-7	N/A
Res2-mf	0.01562	0.0043	~ 99%
Res3-mf	0.02652	0.0022	~ 41%
Res4-mf	0.07516	0.0042	~ 65%

Table 4.9: Alpha parameter results for the multifluid resolution study.

4.4.2 Multifluid Case: Magnetic and Kinetic Energies

In the case of the magnetic energy, there is a considerable difference between the $N_x = 360$ and $N_x = 480$ case. In the former (see Fig.4.16), the growth and saturation of the total magnetic energy is seen to be similar in profile to the ideal case at the same resolution although with a slightly higher mean value at saturation in the multifluid case. In the $N_x = 480$ (see Fig.4.16) case no saturation is seen, the total magnetic energy is seen to increase exponentially without bound to the end of the simulation. As was the case with the stresses and alpha parameter this suggests that multifluid effects are becoming resolved at this resolution. The results are summarised in table 4.10

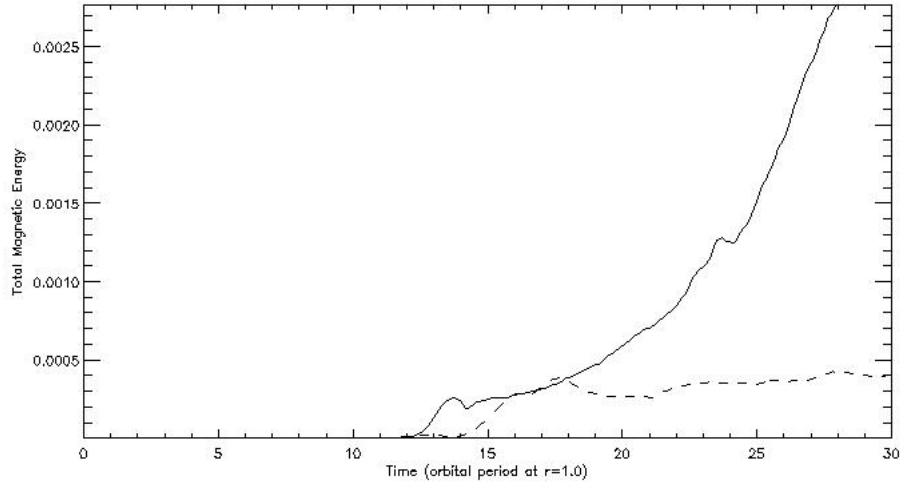


Figure 4.16: The total magnetic energy for the multifluid $N_x = 360$ (dashed line) and the multifluid $N_x = 480$ runs.

Run ID	Mean	Std. Dev.	% of diff. between means
Res1-mf	5.187e-6	3.129e-9	N/A
Res2-mf	4.660e-4	8.784e-5	$\sim 99\%$
Res3-mf	3.767e-4	6.756e-5	$\sim -23\%$
Res4-mf	Maximum 0.002764 (after 28 orbits)	N/A	$\sim 86\%$

Table 4.10: Total magnetic energy results for the multifluid resolution study.

Run ID	Mean	Std. Dev.	% of diff. between means
Res1-mf	N/A	N/A	N/A
Res2-mf	9.68436e-06	1.42766e-06	$\sim N/A\%$
Res3-mf	1.9608903e-05	8.7841183e-07	$\sim 50\%$
Res4-mf	6.8453818e-05	4.8377172e-06	$\sim 71\%$

Table 4.11: Perturbed kinetic energy results for the multifluid resolution study.

The perturbed kinetic energy (see Fig.4.17) shows a similar growth as is seen for the total magnetic energy for the finest resolution case. However, it does eventually saturate at a value considerably larger than the $N_x = 360$ case. As will be seen in chapter 7 the Hall effect is solely responsible for this rate of growth in the total magnetic energy. This unbounded growth does not transfer to the perturbed kinetic energy and is seen to saturate. The

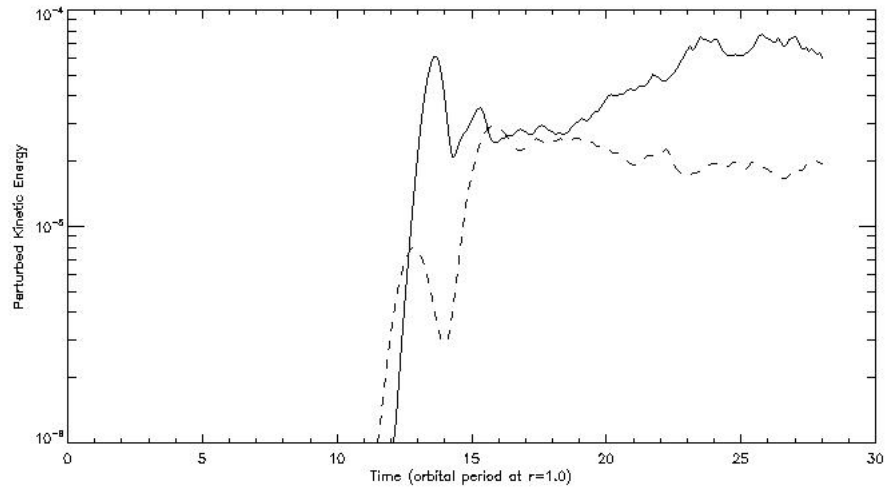


Figure 4.17: The perturbed kinetic energy for the multifluid $N_x = 360$ (dashed line) and $N_x = 480$ (solid line) runs.

turbulence seen in the neutral fluid is caused through interactions with the charged fluids. The severity of the turbulence seen in the neutral fluid will be limited by the magnetic field strength but will most likely also be limited by the frequency of neutral-ion collisions.

Chapter 5

Ideal MHD Versus Multifluid

It is understood that the majority of material in accretion disks is weakly ionised plasma (Salmeron and Wardle, 2003). In a weakly ionised plasma, only a small fraction of the particles making up the bulk material are charged and are directly affected by a magnetic field. The ideal MHD framework is not sufficient for describing regions of the disk where the fluid is weakly ionised and therefore to obtain a realistic picture of MRI generated turbulence in accretion disks and the effect that might have on the anomalous viscosity, it is necessary to move to a full multifluid treatment.

This chapter presents a direct comparison of ideal MHD and fully multifluid simulations which capture the magnetorotational instability. The aim is to show that the ideal MHD regime gives an unrealistic estimation of the net angular momentum transport in accretion disks in the parameter range outlined in section 3.4.4.

What follows is the first known study of the development and influence of the MRI using high resolution, global and fully multifluid simulations of accretion disks which will provide a value for the anomalous viscosity expected when multifluid effects are taken into account.

5.1 Comparison of Ideal MHD and Fully Multifluid Studies

The stresses show a considerable difference between the ideal MHD and multifluid cases (see Fig.5.2 and 5.4). In the ideal MHD regime, after the initial growth, the stresses show very little change post saturation. There is a gradual increase followed by a gradual decrease in the Maxwell stress towards the end of the simulation but this is small compared to the magnitude of the Maxwell stress. The Reynolds stress shows the same tight distribution about the mean value calculated for 20 orbits post saturation. The nature of the turbulence in the disk appears to not change appreciably over the period of time studied in the ideal case. This is confirmed in the perturbed kinetic energy plot (see Fig.5.8), which shows a very flat profile which suggests that the turbulence does not become any more severe and the greyscale plots of the neutral density confirm this (see Fig.5.1). The alpha parameter remains relatively constant for all time post saturation to the end of the simulation (see Fig.5.5). This suggests that the anomalous viscosity generated by the MRI is constant which would lead to a sustained rate of transport of angular momentum and a constant (with respect to time) rate of accretion. It is interesting to note that no accumulation of magnetic flux is seen at the inner boundary and the consequent bursty accretion seen in the work of Romanova et al. (2011) does not occur. Although the radial range studied in this work is quite close to the inner boundary, it does not include the region adjacent to the central object and so the same effect may not be seen.

In the multifluid case however, the nature of the turbulence changes significantly over the life of the simulation. Immediately after saturation the turbulence seems to have similar lengthscales to the ideal case but after a few orbits there is noticeably more accretion taking place and the turbulence in the multifluid simulation appears much more severe and possesses features on the grid that are larger in scale than in the ideal case. The power spectra of the neutral density is presented in Fig.5.3. There is considerably more power in all wavenumbers compared to the ideal MHD case. There is a concentration of power in the range $8 < k < 16$ in the full multifluid case whereas the opposite seems to be true in the ideal MHD case. At large length scales there is a significant difference in the power spectra showing that larger

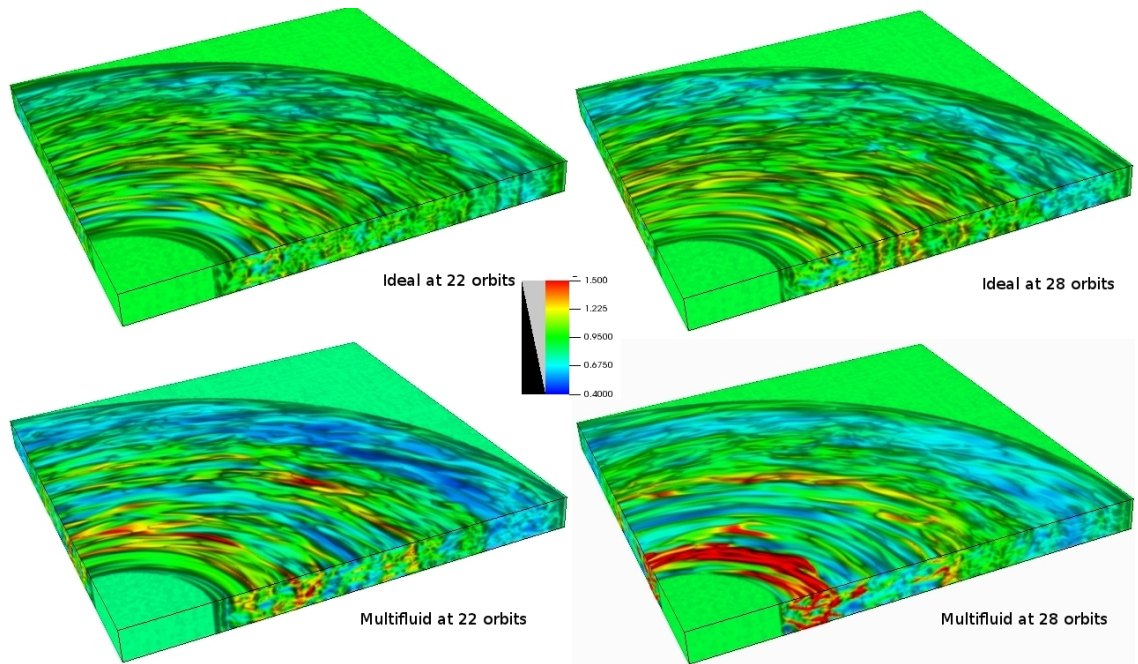


Figure 5.1: A comparison of the neutral density at different times for both the ideal MHD and multifluid cases. The top two panels show the ideal neutral density at 22 orbital periods and 28 orbital periods respectively from left to right. The bottom two panels show the neutral density in the multifluid case at the same points in time.

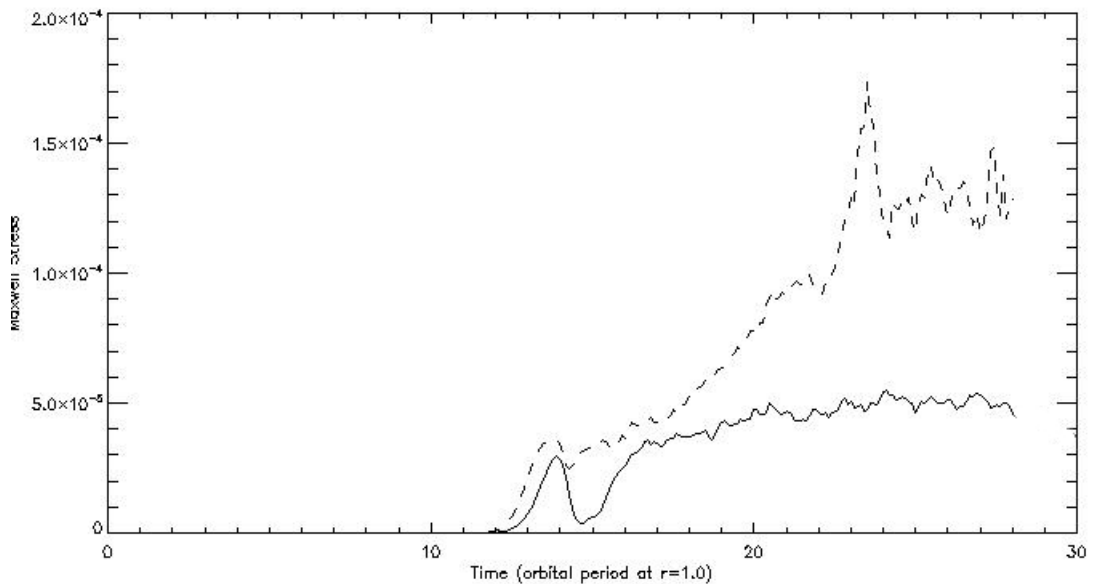


Figure 5.2: Plot of the ideal MHD (solid line) and multifluid (dashed line) Maxwell stresses. Note that the multifluid Maxwell stress looks as though it will saturate initially but continues growing roughly linearly and saturates at a level roughly 2.5 times that of the ideal MHD run.

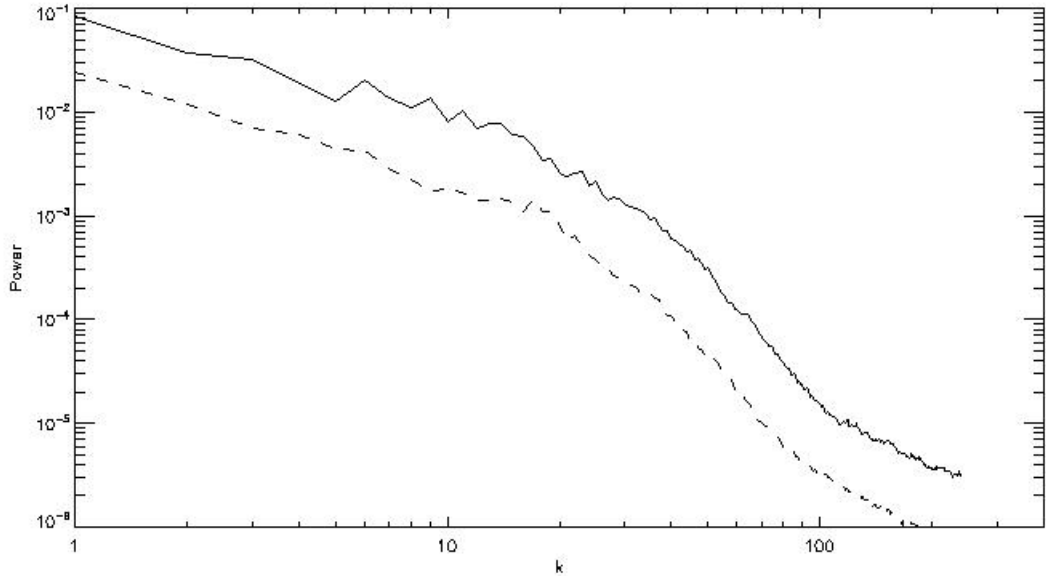


Figure 5.3: Plot of the neutral density power spectra for the res4-mf (solid line) and res4-ideal runs (dashed line). Considerably more power is present for all k in the full multifluid run.

scale structures are present in the full multifluid case.

The stresses in the multifluid regime saturate at a much later time than the ideal case (see Fig.5.2 and 5.4). The difference between the magnitude of the Maxwell stress in the ideal and multifluid case is large. The Reynolds stress shows a smaller difference. This is to be expected as the stretching and twisting of the magnetic field and the resultant stress would be much more severe than the fluid motions that result from the fluids interaction with the magnetic field.

In the Maxwell stress and alpha parameter (see Fig.5.5), it seems as though saturation may occur at approximately the same level as the ideal MHD case but then a renewed period of growth occurs that takes place over a larger timescale compared to the timescale of the initial growth related to the linear MRI occurs which eventually saturates. The alpha parameter for the multifluid simulation saturates at a level just over 2.5 times that of the ideal MHD simulation. This suggests that accretion is occurring at a much higher rate than in the ideal case.

The mean accretion rate is calculated for the ideal and multifluid cases over the first 5 orbits (at $r=1.0$) following saturation for each simulation,

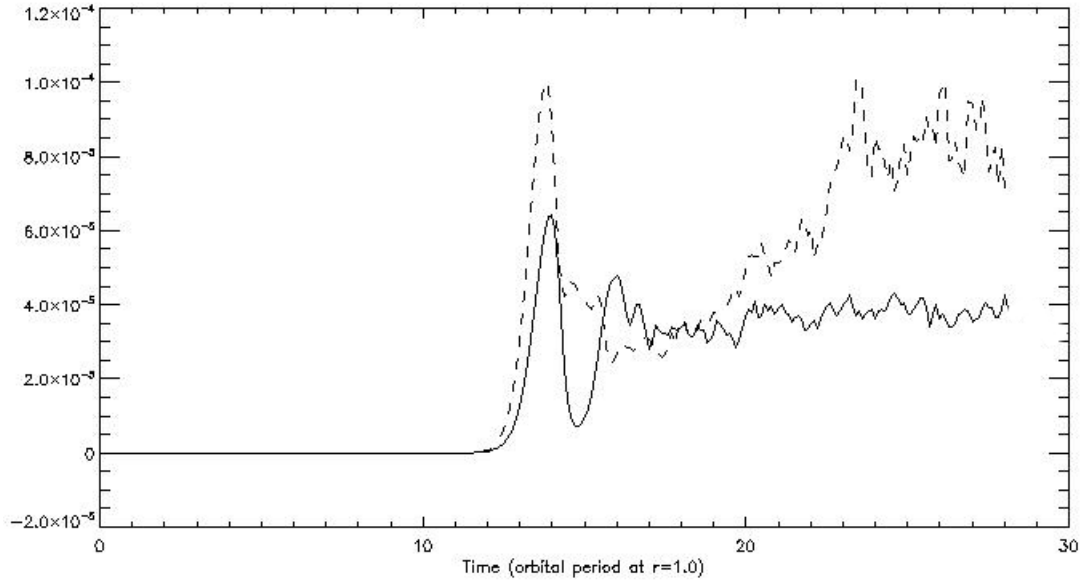


Figure 5.4: Plot of the ideal MHD (solid line) and multifluid (dashed line) Reynolds stresses. The difference between the Reynolds stresses at saturation is less than that of the Maxwell stress.

these are calculated to be 3.89×10^{-7} solar masses per year for the res4-ideal run and 1.04×10^{-6} solar masses per year for the res4-mf run. These accretion rates are high compared to what is estimated observationally, efforts have been taken to scale these calculations to take into account the geometry of the computational grid. However the values calculated here cannot readily be compared to observations due to the missing vertical structure of the disk.

The reason for this very high level of anomalous viscosity is related to the lack of saturation in the magnetic energy. The magnetic energy in the multifluid regime shows very strong exponential growth from shortly after the injection of the perturbation to the end of the simulation. These results suggest that the Hall effect may very likely be responsible for this unbounded growth in the total magnetic energy. The reason for this is the destabilising effect of the Hall effect which is outlined in section 2.4.

The perturbed kinetic energy does saturate (see Fig.5.8 although it does show a similar profile as the stresses and alpha parameter. The perturbed kinetic energy shows initial growth followed by a period in which it seems to have saturated, and then finally another period of growth and eventual saturation occurs at a level much higher than in the ideal case. The fluid

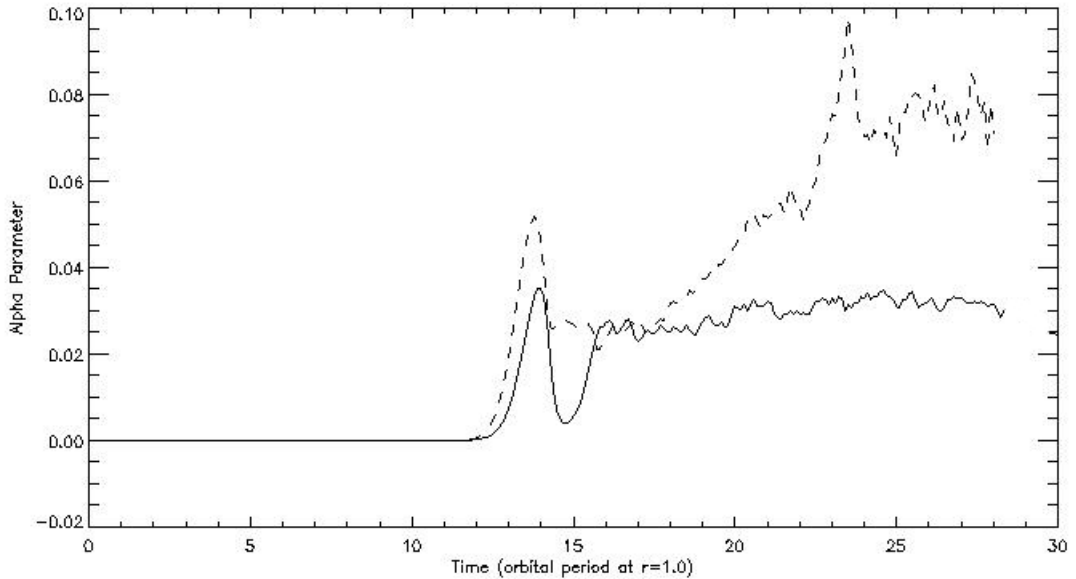


Figure 5.5: Plot of the ideal MHD (solid line) and multifluid (dashed line) alpha parameter.

motions in all 3 fluids visibly show quite violent turbulence.

The behavior seen in the multifluid total magnetic energies has precedence in the literature, in a 2-dimensional non-ideal local simulation (Sano and Stone, 2002a) which studied the Hall effect when the Ohmic term is not small. This growth without bound occurs in this case when the parameter which describes the importance of the Hall term has a non-negative value. A negative value is obtained by reversing the orientation of the initial magnetic field with respect to the direction of the angular momentum vector. Also this only seems to occur when a net-field is applied to the disk. Sano and Stone (2002a) attribute this to the channel solution which grows without bound. It is not confirmed if the unbounded growth of magnetic energy seen in our 3-dimensional global model may be because of a global analogue of the channel solution seen in local simulations. Evidence of this effect is not seen on the grid.

The unbounded growth in the magnetic field is certainly not a result of magnetic energy being introduced through the inner or outer boundaries. To ensure that this is the case, the total magnetic energy is simultaneously calculated for a number of annular regions throughout the disk and this is done throughout the life time of the simulation. The total magnetic energy

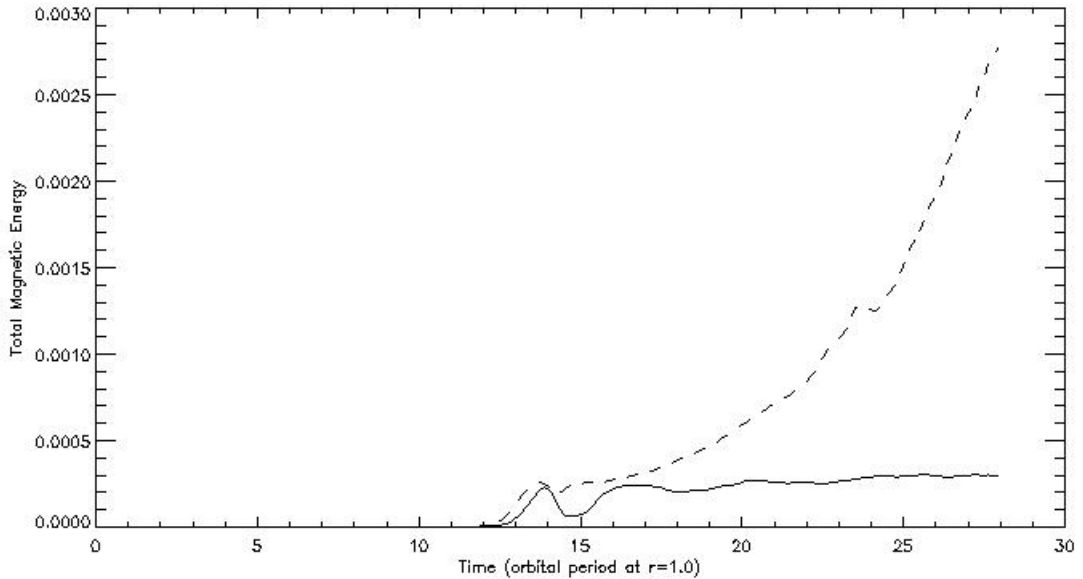


Figure 5.6: Plot of the ideal MHD (solid line) and multifluid (dashed line) total magnetic energies. Note that the multifluid total magnetic energy does not saturate and continues to grow exponentially without bound.

is seen to grow exponentially in each annular region. The motions of the electron and ion fluids do not show accretion that is significantly different from the neutral species flow either. There is some buildup of magnetic energy immediately adjacent to the inner boundary but it is not seen to affect the dynamics outside this small region.

The power spectra for the components of the magnetic field are calculated, using a similar method to the azimuthal decomposition seen in the power spectra of (Arlt and Rüdiger, 2001), to determine if the unbounded field growth is more evident at small or large scales (see Fig.5.7). As seen in the ideal MHD case, the magnetic field is dominated by large scale components. This is expected with a magnetic instability such as the MRI which produces a large scale azimuthal field. As the disk evolves and the total magnetic energy increases exponentially and continues to grow, the power contained in each component grows on all wavenumbers. The azimuthal component still dominates over the others in the range $k < 10$, and this corresponds to the large scale azimuthal component. Interestingly, the growth of the power contained in this range stops increasing once the Maxwell stress saturates but the power contained at the smaller scales continues to grow.

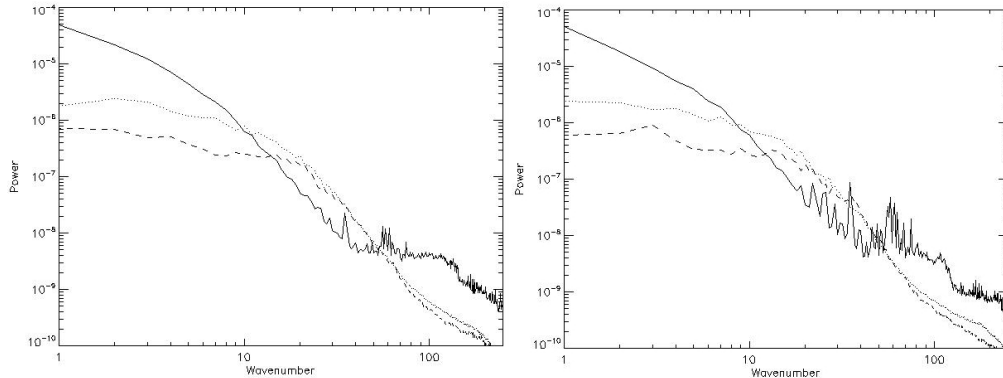


Figure 5.7: Plot of the power spectra for the azimuthal (solid line), radial (dotted line) and vertical (dashed line) magnetic field components for the disk at 14 orbits (left pane) and 17 orbits (right pane) past perturbation injection.

The difference between the components lessens at smaller scales and diverges at the smallest scales. An interesting effect is noted at the smallest scales ($20 < k < 100$), i.e. the region where the power seems to continue growing, especially in the azimuthal and radial components, where a very jagged profile is seen. However similar power spectra are calculated for the ideal MHD and ambipolar dominated runs and a similar feature are seen and so this is not specific to runs where the Hall effect is important. However, it is more pronounced in the multifluid MHD case.

It is likely that some small scale local process which is a consequence of the Hall effect is active. While the Hall effect is not a diffusive effect, it does reorient the magnetic field. This re-orientating of the magnetic field could give rise to a field configuration that compliments the local fluid flow so as to further destabilise the disk in addition to how it is already known to enhance the transport of angular momentum (see section 2.4). This effect leads to the continuing growth of the magnetic field at smaller scales.

It is clear from the results that multifluid effects have great importance in determining the properties of accretion disks in the parameter range studied here.

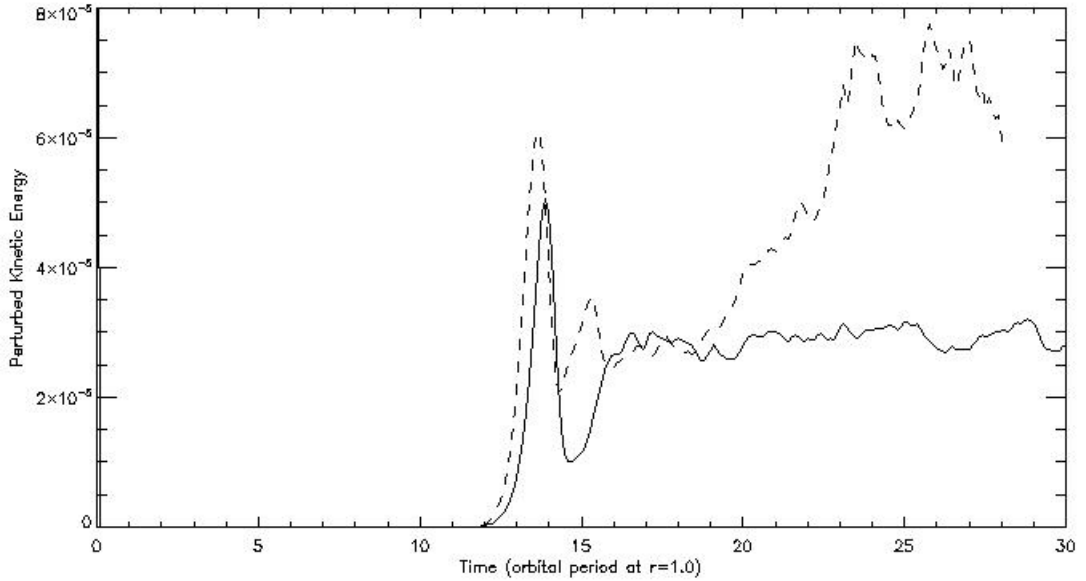


Figure 5.8: Plot of the ideal MHD (solid line) and multifluid (dashed line) perturbed kinetic energies.

Parameter	Resistivity in code units
Parallel (Ohmic) resistivity	1.044e-6
Hall resistivity	8.112e-6
Ambipolar resistivity	1.268e-6

Table 5.1: Initial resistivities given in code units before perturbation injection.

Initially, the resistivities are small and change accordingly as the disk evolves and the magnetic field amplifies. The initial values for the resistivities are given in table 5.1. They show that the disk is initially Hall dominated. Once the perturbation is injected and the disk is well into the period of growth the resistivities grow steadily due to the unbounded amplification of the magnetic field. This question will be explored in chapters 6 and 7 where non-ideal effects are isolated in turn and compared to the full multifluid case to determine if a single effect or more is responsible for this behaviour of the magnetic field and the elevated stresses associated with it.

Parameter	Resistivity in code units
Parallel (Ohmic) resistivity	1.0597e-6
Hall resistivity	1.4162e-4
Ambipolar resistivity	8.7209e-5

Table 5.2: Resistivities given in code units at 22 orbits.

Values for the resistivities which are averaged radially, excluding a small region just inside the radial boundaries to reduce their effect on the results are presented in tables 5.2 and 5.3 after 22 and 28 orbits respectively. The flow is Hall dominated up to 22 orbits and sometime between 22 orbits and 28 orbits it then becomes ambipolar dominated. It is likely that as the magnetic field strength grows due to the MRI process, the lengthscales associated with the Hall effect may become at least marginally resolved leading to enhanced growth in the magnetic field. This would lead to increased accretion as the magnetic stresses increase. In the study of Bai and Stone (2011), a strong correlation was shown to exist between the importance of ambipolar diffusion, characterised by the dimensionless number Am , and the saturation value of the alpha parameter. Ambipolar diffusion dominates in regions of low density and high magnetic field strength. The total density in the disk has been shown to decrease more quickly by accretion in the multifluid case than in the ideal case. This smaller disk density at the mid to outer radii combined with the enhanced growth in the magnetic field leads to ambipolar diffusion becoming dominant.

Parameter	Resistivity in code units
Parallel (Ohmic) resistivity	1.08873e-6
Hall resistivity	3.56284e-4
Ambipolar resistivity	7.43993e-4

Table 5.3: Resistivities given in code units at 28 orbits.

It will become necessary to isolate both the Hall effect and ambipolar diffusion, to be sure whether either or both are directly responsible for the unbounded growth in the magnetic field and in what way does the process works (see chapters 6 and 7).

Chapter 6

Ambipolar Diffusion Dominated Study of the MRI

In this chapter, the Hall effect is artificially removed from the dynamics so that the effect of ambipolar diffusion on the evolution of the accretion disk can be determined. The ambipolar dominated accretion disk is then compared to the ideal MHD and fully multifluid regimes. By doing this, it will also give a strong indication of the importance of the Hall term in producing the enhanced accretion and exponential growth of the total magnetic energy seen in chapter 5. Note that a similar study is not performed for Ohmic diffusion as it the Ohmic resistivity not seen to grow in the fully multifluid case and indeed remains small relative to ambipolar and Hall diffusion.

6.1 Numerical Set-up

To ensure that Hall diffusion plays no role in determining the evolution of the accretion disk and the MRI process over the lifetime of the simulation it is necessary to remove Hall diffusion from the system. To accomplish this, the Hall resistivity is hard coded to a uniform value such that $r_H \ll r_o$ and $r_H \ll r_A$ initially. The Hall resistivity is set to a value of 1×10^{-8} . The Hall resistivity is maintained at this value throughout the simulation so that it may not grow as the magnetic field grows due to the influence of the MRI. The ambipolar and Ohmic resistivities are however allowed to evolve normally through out the simulation and are determined solely by the properties of the

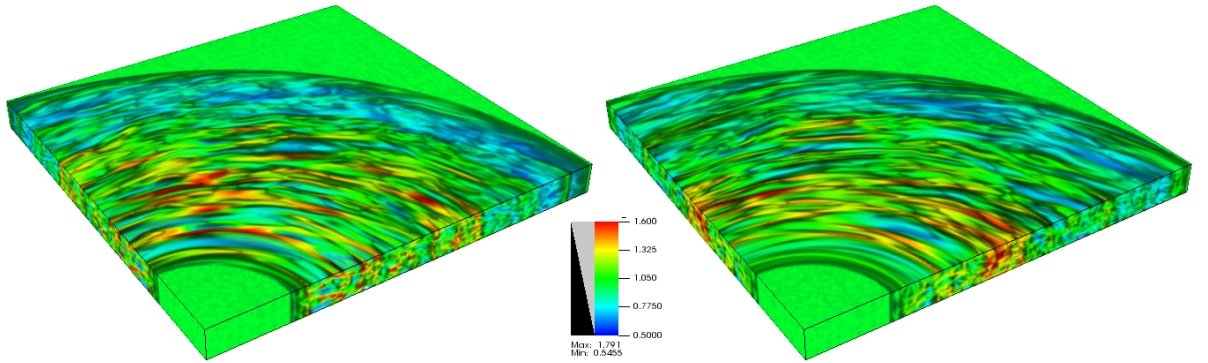


Figure 6.1: A volume plot of the neutral density for the res4-ideal (left frame) and 480-mf-ambidom (right frame) runs after the disk has evolved through 15 orbits at $r=1.0$. Although similar, turbulence is slightly more severe in the res4-ideal run.

flow and so it will become easier to see how ambipolar diffusion can alter the properties of the MRI compared to the ideal MHD and full multifluid MHD cases. The initial values of the Parallel (Ohmic) resistivity and ambipolar resistivity are 1.044×10^{-6} and 1.268×10^{-6} respectively. Refer to section 3.4 for full details of the numerical setup. The run ID for the ambipolar dominated run is 480-mf-ambidom.

6.2 Results of Ambipolar Dominated Study of the MRI Compared to the Ideal MHD case

The evolution of the Maxwell (see Fig.6.2) and Reynolds stresses (see Fig.6.3) for the ambipolar dominated (480-mf-ambidom) case mimic the results from the ideal MHD (res4-ideal) case quite closely. A very similar profile is seen for both cases, however, the saturation levels of the stresses differ by roughly 30-40%. The growth rate (obtained using linear fit) for the Maxwell stress in the ambipolar case is 0.153 per orbit compared to 0.186 for the res4-ideal run. The ideal MHD stresses are more variable. Qualitatively, the turbulence on the grid appears similar and appears to occur on similar lengthscales (see Fig.6.1) although the turbulence in the ideal MHD case seems to be slightly more severe.

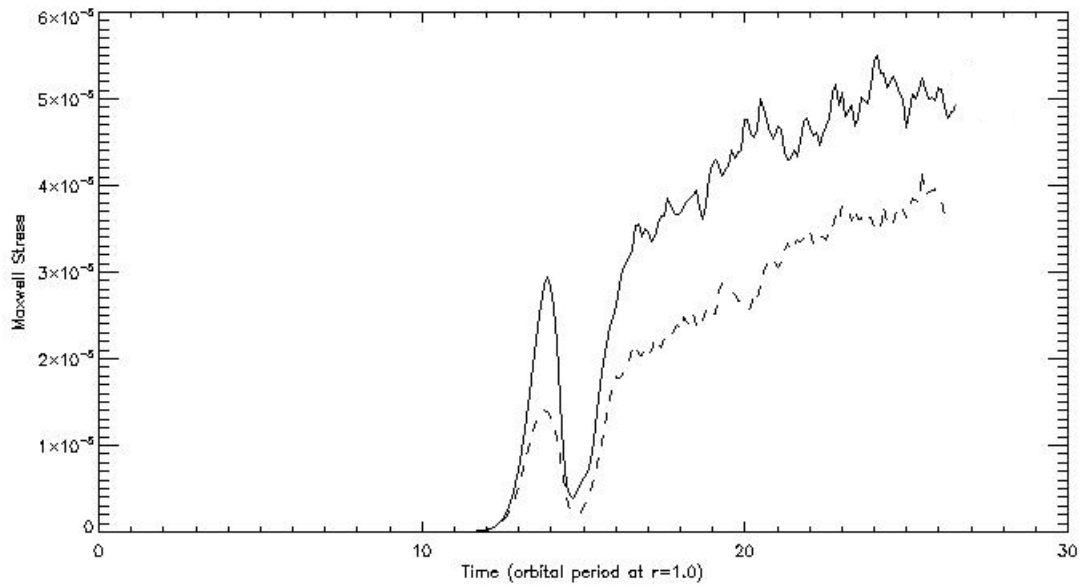


Figure 6.2: Plot of the Maxwell stresses for the res4-ideal (solid line) and 480-mf-ambidom (dashed line) runs. The growth rate of the Maxwell stress for both cases are very similar although the value of the Maxwell stress in the ambipolar dominated case is consistently 25-40% smaller and get closer together towards the end of the simulation.

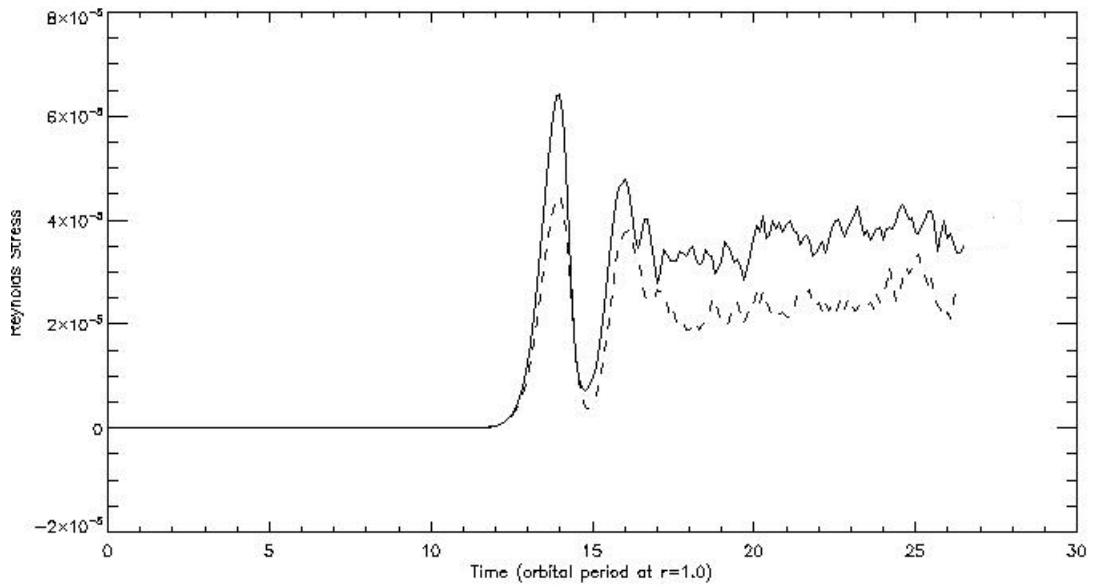


Figure 6.3: Plot of the Reynolds stresses for the res4-ideal (solid line) and 480-mf-ambidom (dashed line) runs. Once saturation occurs the Reynolds stresses in both cases remain constant.

As a result, the alpha parameter is decreased in the case where ambipolar diffusion is important (see Fig.6.4) when compared to the ideal MHD case. The mean value of the ambipolar resistivity increases from an initial value of 1.12×10^{-6} at the point of perturbation injection to a value of 3.679×10^{-5} after 13 orbits of the inner disk ($r=1.0$). This is a significant increase. The smaller the magnitude of the resistivity, the closer the disk model properties are to what would be expected in the ideal MHD regime. Therefore ambipolar diffusion is becoming more important allowing the field lines to slip through the neutral fluid with greater ease. This leads to a lower saturation value for the stresses and consequently the alpha parameter. This is expected from the linear analyses of Blaes and Balbus (1994) and results of the simulations of Simon et al. (2013) where ambipolar diffusion was an important process. The mean ambipolar Elsasser number, 13 orbits after perturbation injection is of the order of $Am \approx 100$ and this value will be a function of radius, so ambipolar diffusion would be more important at the outer radii of the disk where densities and magnetic field strength are low relative to the values at the inner disk. The global consequences of this is that non-uniform accretion rates are seen in the disk which may lead to gaps in the disk. Accretion may be very weak at outer radii and then as material moves into the Hall dominated region (1-30 AU) the MRI may be enhanced leading to high rates of accretion in this region.

Interestingly, the energies follow a profile that is very similar especially in the early stages of evolution, the results naturally diverge at later times. This occurs as the turbulence developed by the MRI is less severe in the ambipolar dominated case. The amplitude of the total magnetic energy at saturation is lower in the ambipolar diffusion dominated case by approximately 20-30% (see Fig.6.5). This is due to the fact that the magnetic field (and the charged fluids) may diffuse through the neutral fluid and may not in the ideal MHD case. The rates of growth are interestingly very similar over the period studied. The growth rate (using linear fit) of the total magnetic energy are 1.027×10^{-4} and 9.22×10^{-5} for the ideal MHD and ambipolar cases respectively. These growth rates are closer together than the growth rates of the Maxwell stress.

The perturbed kinetic energies saturate at different levels but at approximately the same time (see Fig.6.6). Due to the reduced severity of turbulence

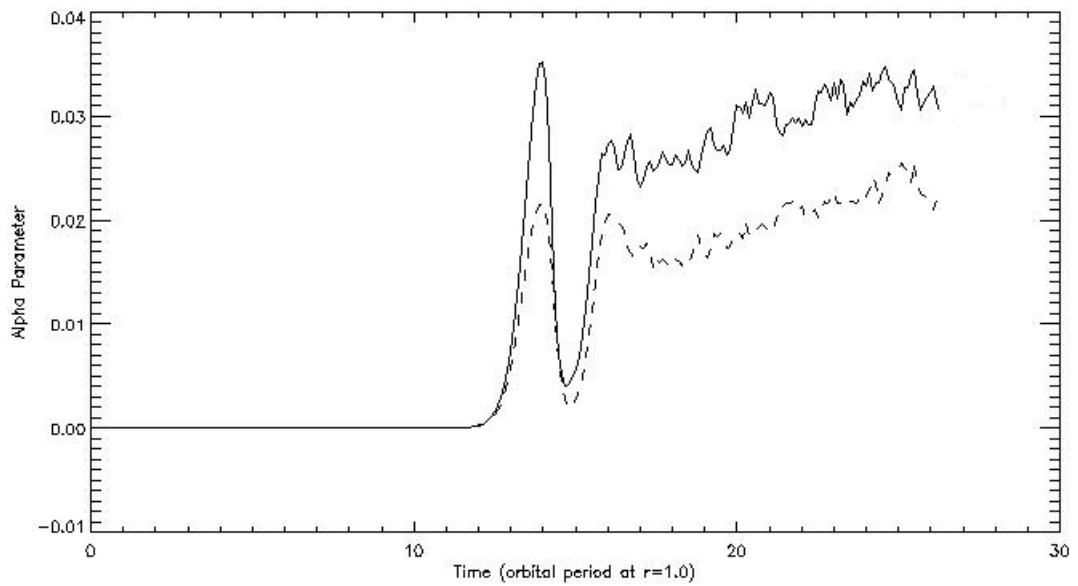


Figure 6.4: Plot of the alpha parameter for the res4-ideal (solid line) and 480-mf-ambidom (dashed line) runs. The alpha parameter is consistently higher in the ideal MHD regime. This means that the inclusion of ambipolar diffusion for this model results in less transport of angular momentum outwards in the disk and therefore less accretion inwards.

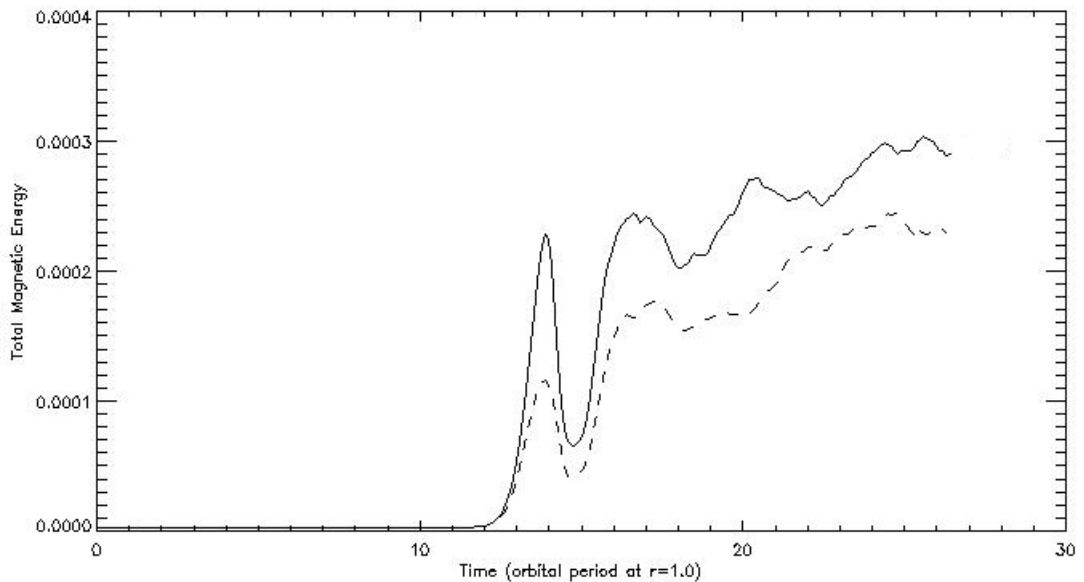


Figure 6.5: Plot of the res4-ideal (solid line) and 480-mf-ambidom (dashed line) total magnetic energies. The profiles are similar, however the values at saturation of the ideal MHD case are consistently higher by approximately 20-30%.

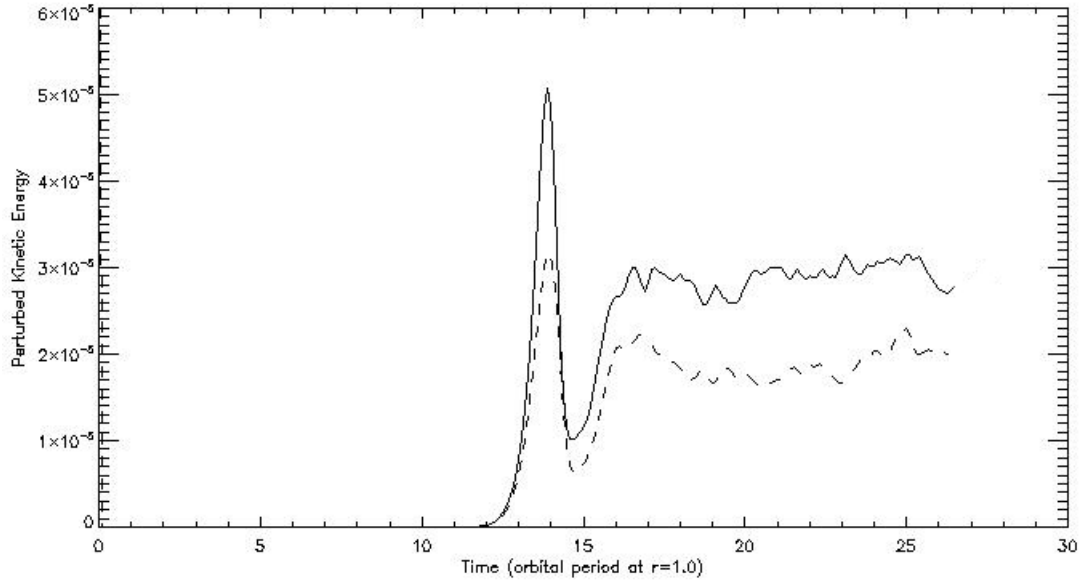


Figure 6.6: Plot of the res4-ideal (solid line) and 480-mf-ambidom (dashed line) perturbed kinetic energies. As with the total magnetic energy, the ideal MHD case shows higher perturbed kinetic energy through out the simulation suggesting the severity of the turbulence is greater.

in the ambipolar dominated case, the kinetic energy does not vary much about its mean value with time compared to the ideal MHD case.

6.3 Results of Ambipolar Dominated Study of the MRI Versus the full Multifluid MHD case

The parallel resistivity is always small compared to the ambipolar and Hall resistivities once the perturbation is injected and the disk is allowed to evolve and so is considered unimportant. It is not necessary to force the parallel resistivity to remain small compared to the other non-ideal terms in the same way as the Hall resistivity is artificially forced to remain small in the ambipolar dominated simulation. This artificial removal of the Hall term is the only difference between the full multifluid (res4-mf) case and the ambipolar dominated (480-mf-ambidom) case. This approach is designed to understand whether the Hall or Ambipolar term is responsible for the enhanced transport

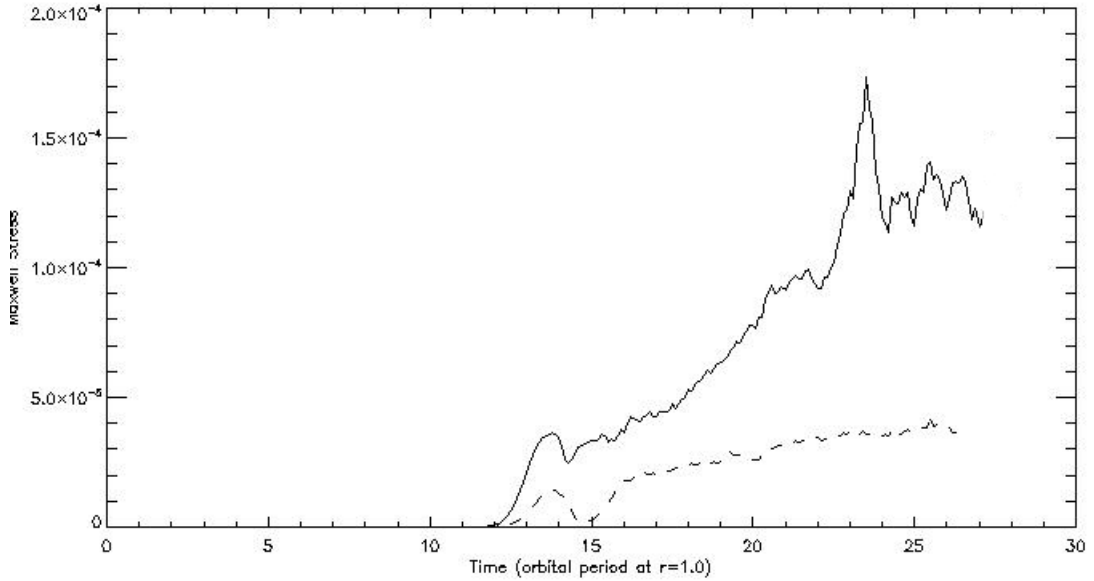


Figure 6.7: Plot of the Maxwell stresses for the res4-mf (solid line) and 480-mf-ambidom (dashed line) runs . When the Hall effect is included, the growth of the Maxwell stresses is significantly increased and saturates at a value four times larger in magnitude.

seen in the full multifluid case.

There are obvious differences in the stresses between the two cases (see Fig.6.7). In the full multifluid case where the Hall effect is allowed to play a significant role, there is a dramatic growth in both the Maxwell and Reynolds stresses as the accretion disk model evolves after the perturbation injection. In the case of the Maxwell stresses, the ambipolar dominated run saturates at a mean Maxwell stress of 3.084×10^{-5} , whereas in the full multifluid run with the Hall effect included, the Maxwell stress saturates at 1.2987×10^{-4} . The Reynolds stress also shows similar behavior but the relative magnitude of the Reynolds stresses is somewhat closer (see Fig.6.9).

Qualitatively the difference between the two simulations is very noticeable. Turbulence is very severe in the full multifluid case. In Fig.6.8 the left panel shows the full multifluid case at saturation while the right panel shows the ambipolar dominated run with the Hall effect removed. It is evident in the left panel that significant accretion has occurred at this point and there is a banded structure in the disk which shows that accretion is occurring at different rates at different radii. It is believed that planets are responsible

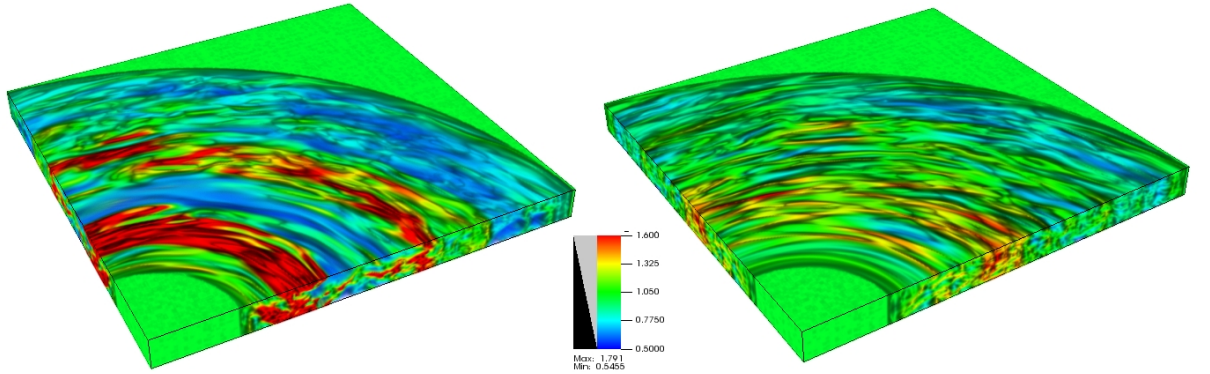


Figure 6.8: A volume plot of the neutral density for the res4-mf (left frame) and 4880-mf-ambidom (right frame) cases after the disk has evolved through 15 orbits at $r=1.0$. Turbulence is considerably more severe in the left panel. A significant amount of accretion has taken place compared to the ambipolar dominated case. In the left panel, evidence for a radial dependence on accretion rate can be seen with the banded appearance of the neutral density.

for creating gaps in accretion disks. The results presented here suggest that planets are not the only process which can create a gap in an accretion disk and that non-uniform rates of accretion may cause the same effect. At this point in the evolution of the disk significant magnetic braking is present due to the exponential growth of the magnetic field.

The saturation value of the alpha parameter when the Hall effect is removed is considerably reduced (see Fig.6.10). The mean of the alpha parameter at saturation was calculated to be 0.02 and 0.0752 for the ambipolar dominated and full multifluid runs respectively. This is a reduction of almost 75%. This suggests that the Hall effect strongly enhances the MRI and the transport of angular momentum leading to more mass accretion towards the central object (see Fig.2.2 and accompanying text for explanation).

The total magnetic energy when the Hall effect is included shows an exponential growth which increases without bound until the simulation ends (see Fig.6.11). Once the Hall effect is removed and ambipolar diffusion is the only important non-ideal process the total magnetic energy is seen to saturate at a value of 1.973×10^{-4} whereas if it is included the total magnetic energy continues to grow to a maximum value of 2.764×10^{-3} by the end of the simulation with no sign of saturating. In the study of Sano and Stone (2002a,b), the Hall effect was shown to enhance or suppress the MRI depending on the alignment of the net flux with the angular velocity vector. The

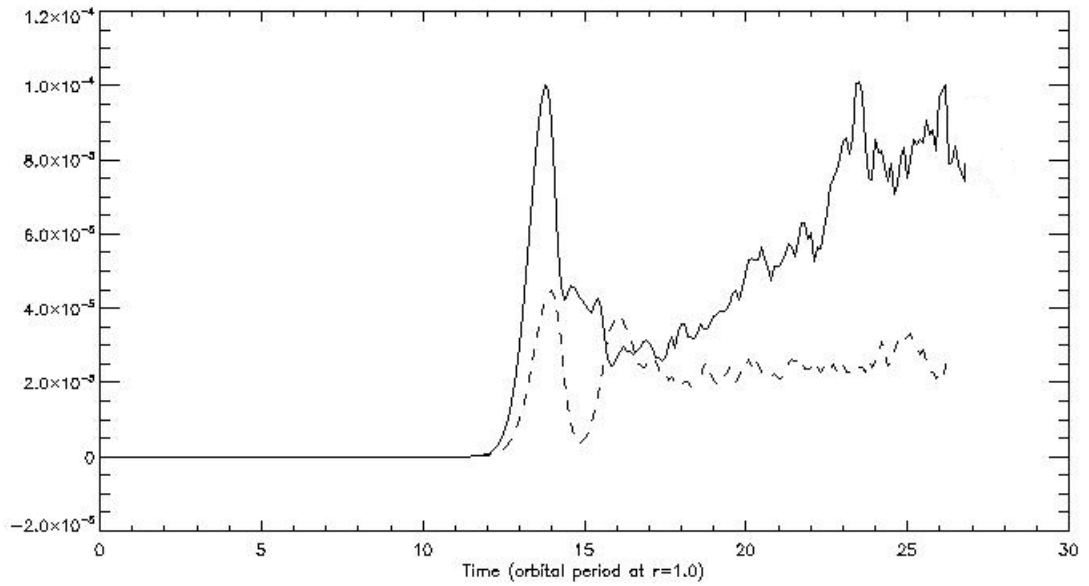


Figure 6.9: Plot of the Reynolds stresses for the res4-mf (solid line) and 480-mf-ambidom (dashed line) runs. The difference between the Reynolds stresses is not as large as with the Maxwell stresses.

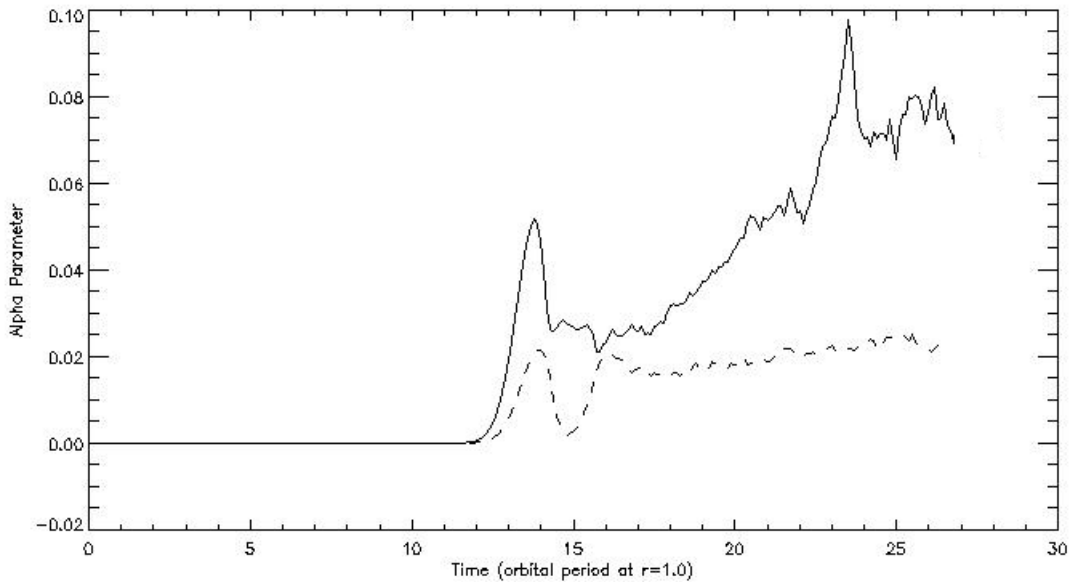


Figure 6.10: Plot of the alpha parameter for the res4-mf (solid line) and 480-mf-ambidom (dashed line) runs. A significant reduction in the alpha parameter is seen once the Hall effect is removed. This suggests that the Hall effect strongly enhances the MRI.

Hall effect introduces a handedness to the dynamics. Later it will be shown that by counter aligning the initial net flux will actually suppress the MRI and the unbounded exponential growth of the magnetic field will disappear. Indeed the removal of an initial net flux altogether will strongly affect the saturation amplitude of the MRI.

Parameter	res4-ideal	res4-mf	480-mf-ambidom
Maxwell Stress	-4.309e-5	-1.299e-4	-3.084e-5
Reynolds Stress	3.632e-05	8.319e-05	2.406e-05
Alpha parameter	0.028	0.0752	0.02
Total Magnetic Energy	3.084e-4	0.002764 (max)	1.973e-4
Perturbed Kinetic Energy	2.76e-05	6.845e-05	1.874e-05

Table 6.1: Results from the main parameters for the ideal MHD (res4-ideal), full multifluid (res4-mf) and ambipolar dominated (480-mf-ambidom) simulations at saturation (if saturation has occurred). Runs where saturation has not occurred will be indicated by (max) indicating the maximum value reached. These are time averaged values taken from the point of saturation to five orbital periods later.

The perturbed kinetic energy does not suffer from the same magnitude of reduction from the removal of the Hall effect which is seen with the total magnetic energy (see Fig.8.14). The saturation amplitude of the perturbed kinetic energy is still considerably less once the Hall effect is removed. Saturation does occur in the full multifluid case at a mean value of 6.85×10^{-5} compared to a mean value of 1.94×10^{-5} in the ambipolar dominated case. This shows that the Hall effect is important in determining the severity of the turbulence.

Once Ohmic diffusion is small (Sano and Stone, 2002a,b), the Hall effect may enhance the MRI and lead to an enhanced anomalous viscosity. It is also known from the above study that the presence of a net flux combined with the handedness that the Hall effect introduces, plays an important role

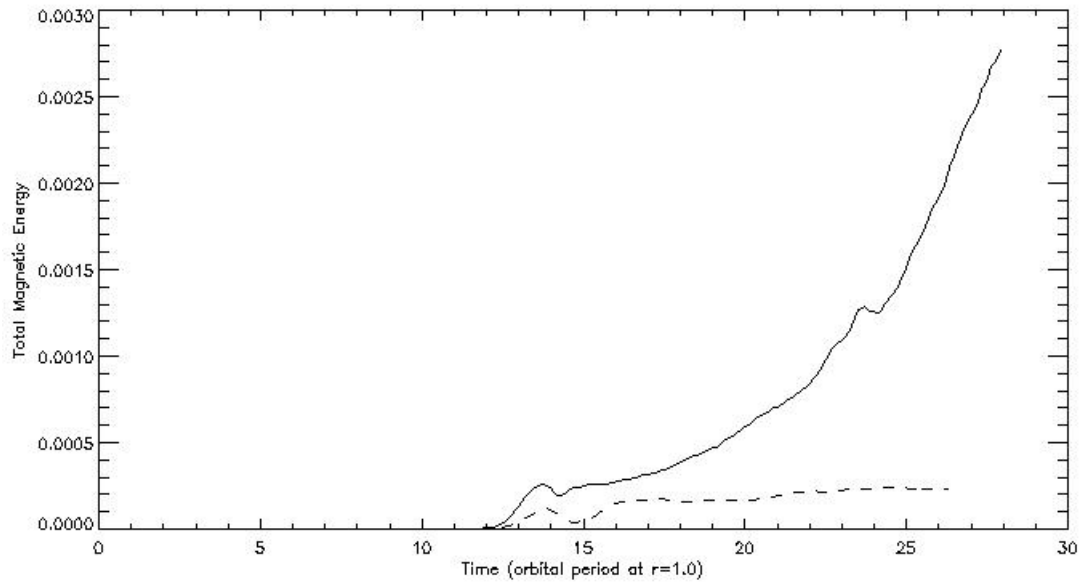


Figure 6.11: Plot of the total magnetic energy for the res4-mf (solid line) and 480-mf-ambidom (dashed line) runs. There is a dramatic growth in the total magnetic energy when the Hall effect is included.

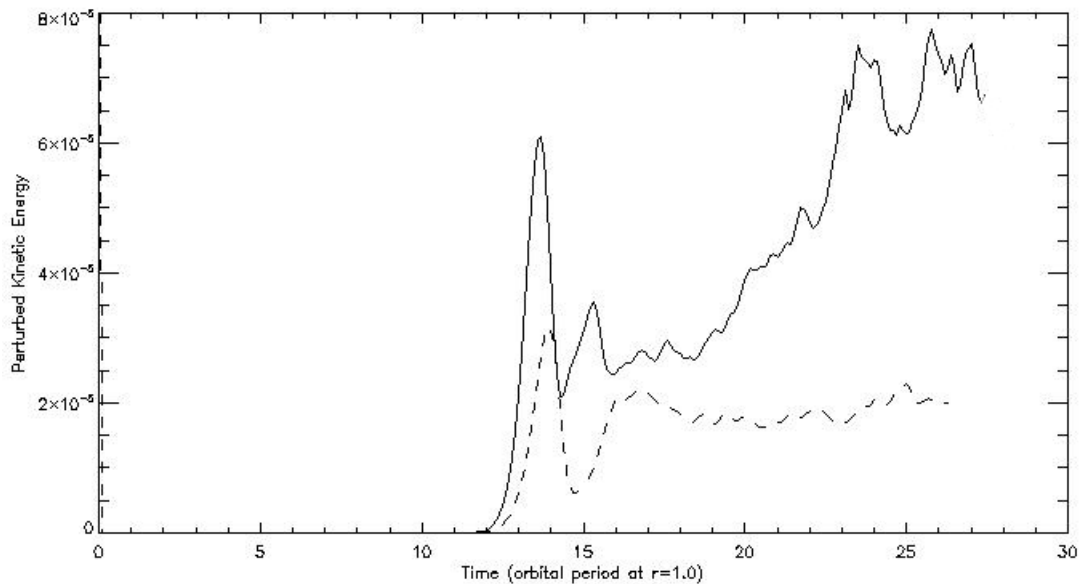


Figure 6.12: Plot of the perturbed kinetic energies res4-mf (solid line) and 480-mf-ambidom (dashed line) runs.

in determining the saturation level of the MRI. This result has never been explored using a fully multifluid code before. This effect of a net flux (or lack of) will be explored in chapter 8.

Chapter 7

Hall Diffusion Dominated Study of the MRI

In this chapter the results of a similar simulation to that seen in chapter 6 are presented except in this case the ambipolar diffusion is removed from the dynamics. The results obtained here will determine whether the Hall effect is solely responsible for the enhanced anomalous viscosity seen in the full multifluid case or whether a combination of ambipolar diffusion and Hall diffusion leads to this enhancement. This approach will also confirm if the Hall effect is responsible for the unbounded exponential growth in the total magnetic energy.

7.1 Numerical Set-up

To ensure that ambipolar diffusion plays no role in determining the evolution of the accretion disk and the MRI process over the lifetime of the simulation it is necessary to remove ambipolar diffusion from the system. To accomplish this, the ambipolar resistivity is hard coded to a uniform value such that $r_A \ll r_o$ and $r_A \ll r_H$ initially. The initial value of the Hall resistivity is 8.1×10^{-6} , and the Ohmic (field parallel) resistivity is 1.044×10^{-6} . Whereas the ambipolar resistivity is set to 1×10^{-8} . The ambipolar resistivity is maintained at this value throughout the simulation so that it may not grow as the field amplification due to the MRI cannot allow it to dominate or become important at a later time. The Hall and Ohmic (field parallel) resistivities

are however allowed to evolve normally throughout the simulation and are determined solely by the properties of the flow and so it will become easier to see how Hall diffusion can alter the properties of the MRI compared to the ideal MHD and full multifluid MHD cases. Refer to section 3.4 for full details of the numerical setup. The run ID for the Hall dominated run is 480-mf-halldom.

7.2 Results of Hall Dominated Study of the MRI Versus the Full Multifluid case

Presented here are the results for the case where ambipolar diffusion is removed from the model. In this model, the Maxwell stress shows a large jump as the perturbation is settling down and the stresses stay large compared to the ideal MHD and full multifluid cases (see Fig.7.2). The stresses in both the full multifluid (res4-mf) and Hall dominated (480-mf-halldom) cases continue growing due to the exponential growth of the magnetic field, which continues without bound in both cases. The effect of ambipolar diffusion on the saturation level is obvious. When ambipolar diffusion is included this has the effect of damping the MRI and lowering the saturation level of the stresses. This is expected if ambipolar diffusion is important enough so that the MRI cannot develop properly. However even when ambipolar diffusion dominates, as in the later stages of the full multifluid run, the stresses are seen to continue increasing for a long time after the ideal MHD (res4-ideal) run has saturated.

The Reynolds stresses show similar properties at saturation. The Hall dominated case saturates at a higher level than the other two cases (see Fig.7.4). The Reynolds stresses do not continue to grow much past the time at which saturation occurs. The severity of the turbulent motions may not increase past the saturation of the stresses as the stress is caused by the turbulence which is driven by the MRI. The magnetic energy is seen to grow as the magnetic field is still thrashed about and twisted by the influence of the neutrals on the charged species which are tied to the magnetic field.

The anomalous viscosity which is parameterised by the alpha parameter is much enhanced when ambipolar diffusion is removed. The effective removal of ambipolar diffusion means that the magnetic field has more influence on

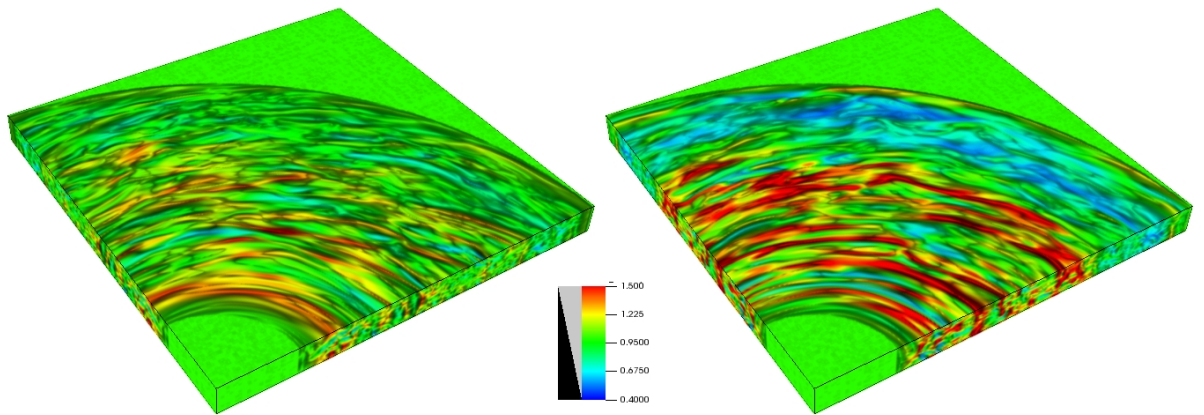


Figure 7.1: A volume plot of the neutral density for the res4-ideal (left frame) and 480-mf-halldom (right frame) cases after the disk has evolved through 8 orbits (after perturbation injection) at $r=1.0$. Turbulence appears significantly more severe in the Hall dominated case when compared to the ideal MHD case. The Hall effect combined with the net field enhances the MRI.

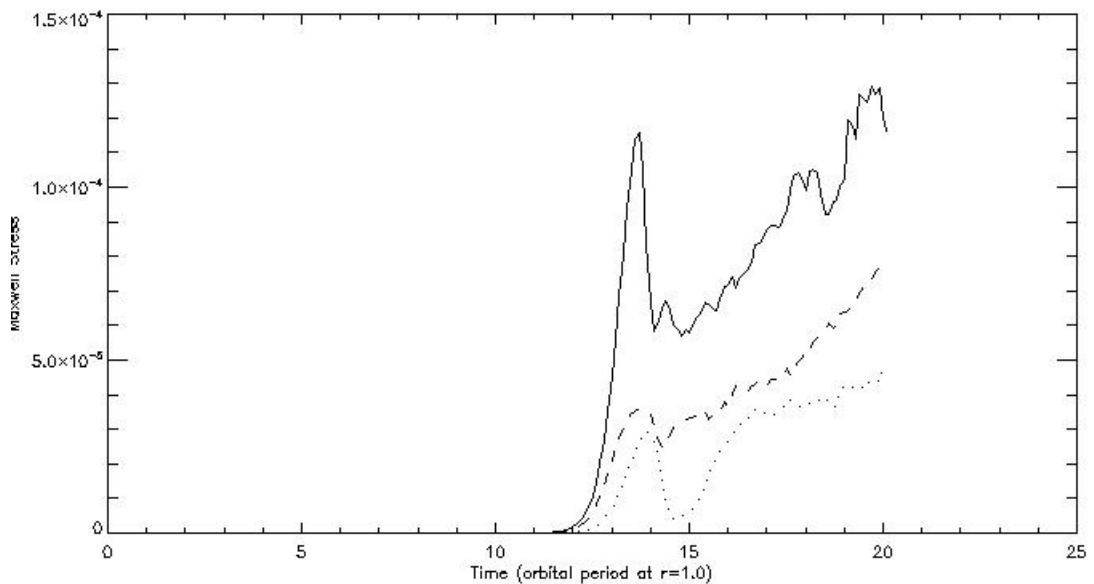


Figure 7.2: Plot of the Maxwell stresses for the 480-mf-halldom (solid line), res4-ideal (dotted line) and res4-mf (dashed line) runs. After the injection of the perturbation at 10 orbits, the Hall dominated case shows much larger Maxwell stresses than both the full multifluid and ideal MHD cases.

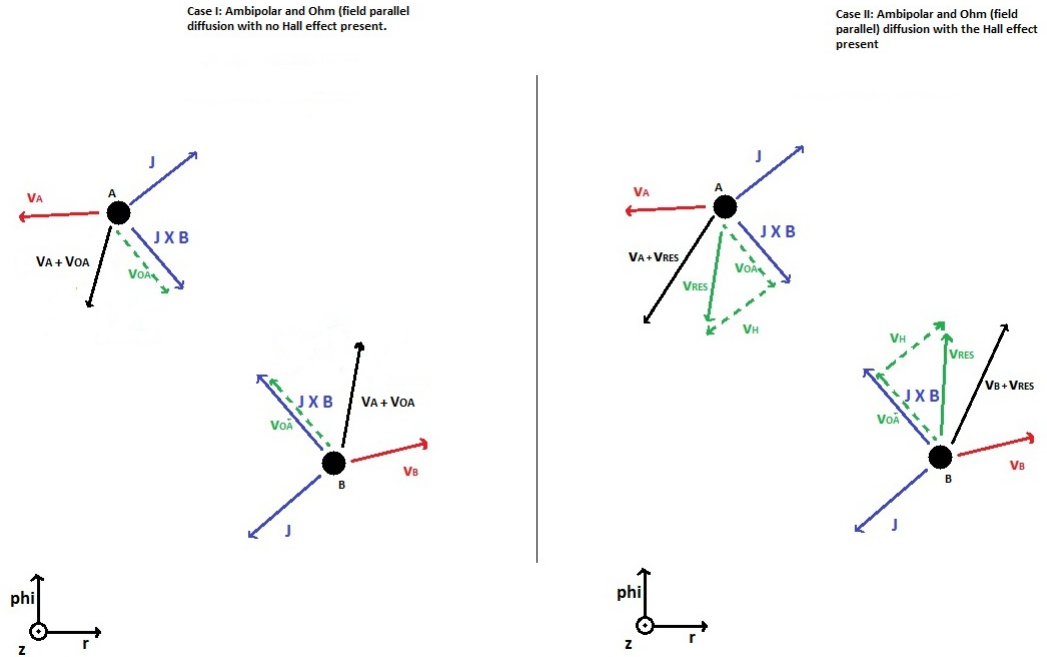


Figure 7.3: Vector diagram illustrating the influence of the Hall effect compared to just the diffusive terms alone. A and B are fluid elements which are separated radially and azimuthally due to rotation and the observer is in the frame of reference of the fluid. The MRI process has had time to act upon them and some angular momentum transfer has occurred from the inner element to the outer element (Wardle and Salmeron, 2012).

the neutral fluid through neutral-ion collisions than it would if ambipolar diffusion was present. The Ohmic (field parallel diffusion does not increase much over the lifetime of the simulation and the parallel resistivity remains small. Since the magnetic field cannot now diffuse through the neutral fluid as easily as in the full multifluid case or the ambipolar dominated case and so the MRI will be strong in this case.

The schematic presented in Fig.7.3 shows how the MRI process works locally in the presence of Ohmic and ambipolar diffusion. This schematic shows also shows how the MRI is affected should the Hall effect be important and what might happen should the purely diffusive terms be removed.

When the Hall effect and the purely diffusive terms are important, the picture outlined in the left pane of Fig.7.3 is changed somewhat and can be seen in the right pane where the Hall effect is present. When the net magnetic

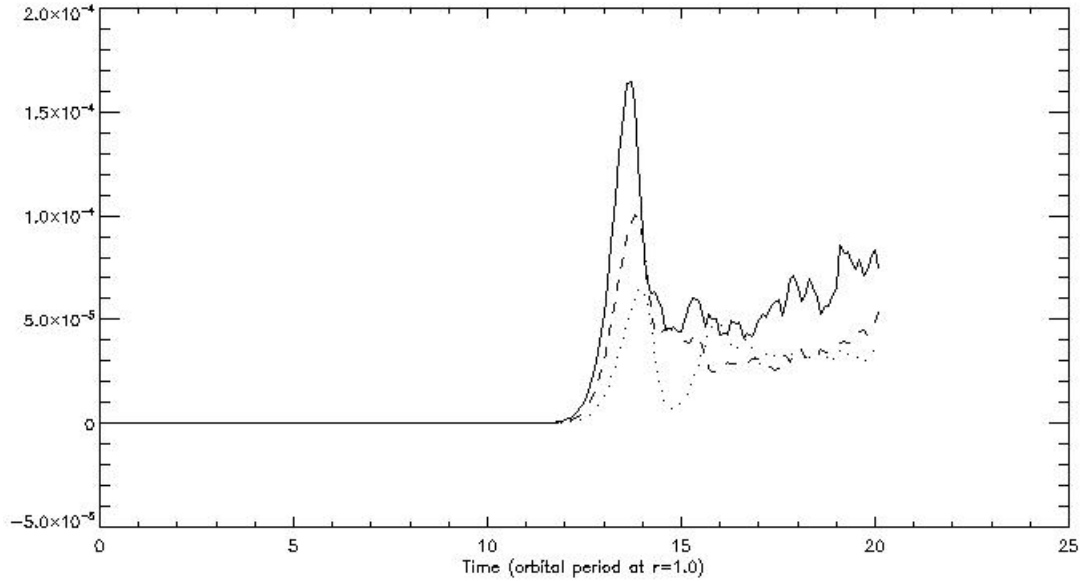


Figure 7.4: Plot of the Reynolds stresses for the 480-mf-halldom (solid line), res4-ideal (dotted line) and res4-mf (dashed line) runs. As in the case of the Maxwell stresses above, the Reynolds stresses for the Hall dominated case are large in magnitude compared to the other two cases.

field is aligned with the net angular momentum vector of the disk (as in this case), the Hall effect creates a drift that is orthogonal to the tension forces that can destabilise the disk further. It can be seen from the right pane of Fig.7.3 how this happens and the inner fluid element now has a resultant velocity vector that is pointing more inward radially due to the Hall drift and the opposite effect is seen for the outer element. The drift due to ambipolar and Ohmic diffusion actually acts to stabilise the disk somewhat. Once this stabilising drift is lessened or removed and the drift due to the Hall effect is still present, this will act to further destabilise the disk and increasing angular momentum transfer. This is an explanation for why the stresses are seen to be considerably higher in the Hall dominated case (Wardle and Salmeron, 2012).

Just like in the full multifluid case, the Hall dominated case shows an exponential growth in the magnetic field that continues without bound in the time period studied. The profile of the growth appears much more variable with time in the Hall dominated case. Ambipolar diffusion appears to slow the rate of growth in the magnetic field in the full multifluid case but it is not sufficient to quench the growth altogether. Ohmic (field parallel) diffusion

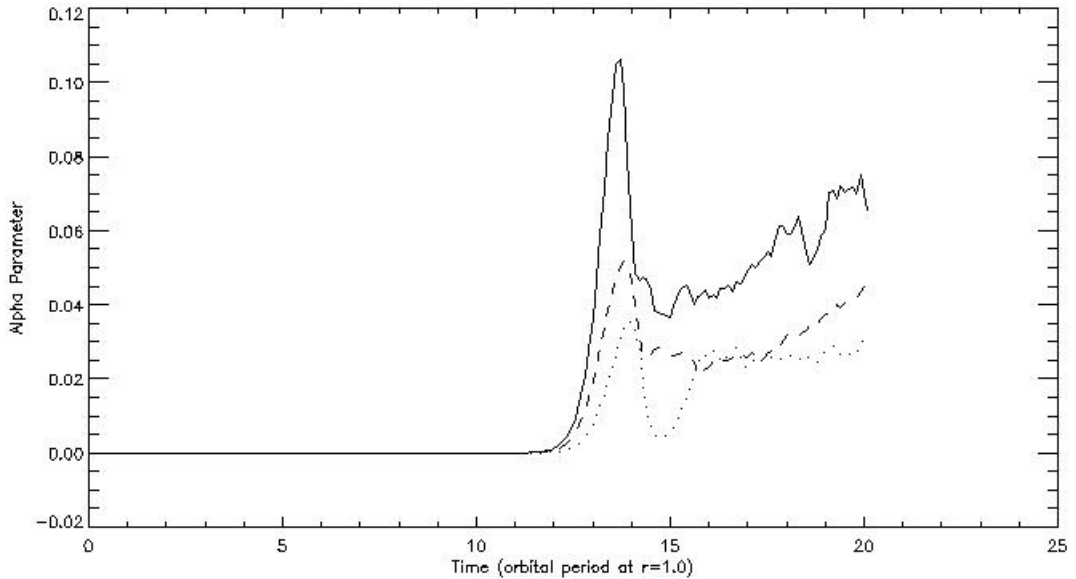


Figure 7.5: Plot of the alpha parameter for the 480-mf-halldom (solid line), res4-ideal (dotted line) and res4-mf (dashed line) runs. The alpha parameter for the Hall dominated case is much larger than both the ideal MHD and full multifluid cases and shows that the anomalous viscosity is enhanced considerably by the Hall effect, especially when ambipolar diffusion is removed.

remains small. In other regions of the disk such as closer to the central object this growth may be stopped entirely due to increased levels of diffusion but in the radial range studied here, Ohmic diffusion is expected to be weak except near the midplane of the disk if vertical stratification were present.

In the simulations of Sano and Stone (2002a,b) such growth in the magnetic field was seen in local 2-dimensional simulations which are presented in Sano and Stone (2002a) where the channel flow was seen to develop and grow unbounded. This effect did not carry over to the 3-dimensional local simulation carried out in Sano and Stone (2002b), the channel flow would grow in this case and then break up and continue in this way quasi-periodically. A global analogue of the channel flow seen in local simulations could be manifesting itself here. Qualitatively no evidence is seen of any channel flow present on the grid.

The perturbed kinetic energy does show the same exponential growth as seen in the total magnetic energy (see Fig.7.7). The deviations of the fluid velocity about the mean flow are much stronger for the Hall dominated case.

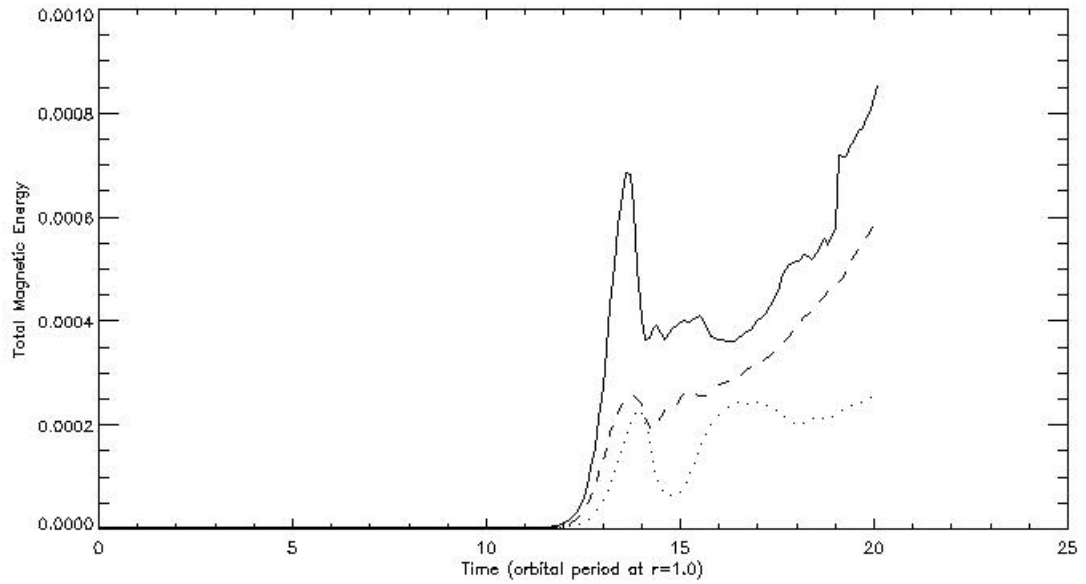


Figure 7.6: Plot of the total magnetic energy for the 480-mf-halldom (solid line), res4-ideal (dotted line) and res4-mf (dashed line) runs. Both the full multifluid and Hall dominated cases show exponential growth without bound in the total magnetic energies. The Hall dominated case shows a profile that is more variable with time compared to the full multifluid case.

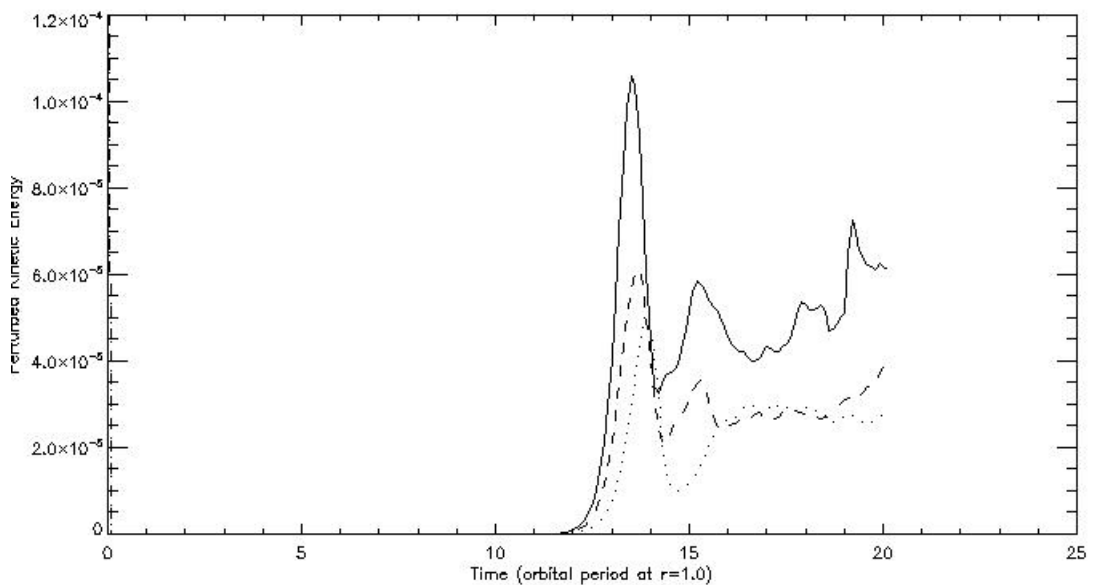


Figure 7.7: Plot of the perturbed kinetic energy for the 480-mf-halldom (solid line), res4-ideal (dotted line) and res4-mf (dashed line) runs. The perturbed kinetic energies in the Hall dominated case are larger in magnitude than the other two cases and show more variability with time suggesting that turbulence on the grid is more severe.

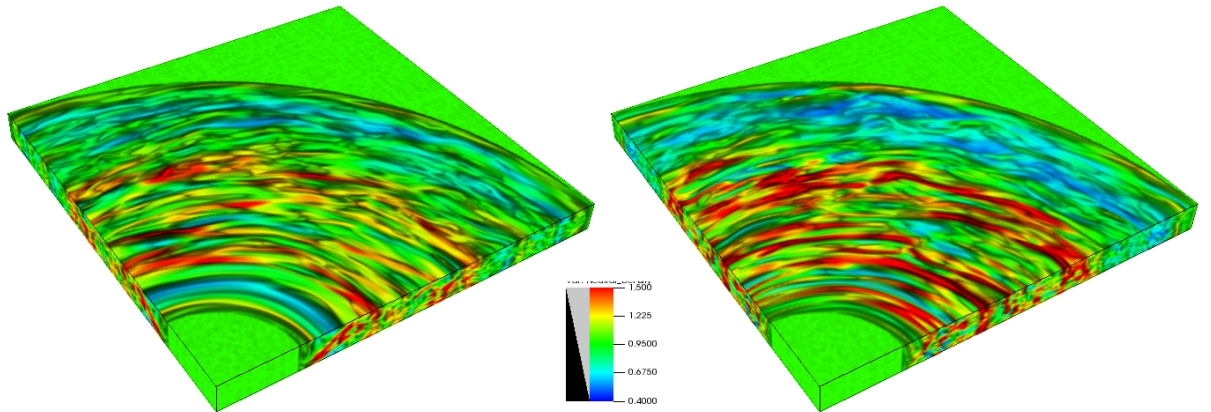


Figure 7.8: A volume plot of the neutral density for the res4-mf (left frame) and 480-mf-halldom (right frame) cases after the disk has evolved through 8 orbits (after perturbation injection) at $r=1.0$. Once ambipolar diffusion is removed the enhancement of the MRI is more pronounced. Banded accretion is present on the grid where accretion is enhanced locally.

Qualitatively, turbulence is seen to be more severe in the Hall dominated case when compared to either the ideal MHD or full multifluid cases. Evidence can be seen in Fig.7.8 of banded accretion where gaps appear to be forming in the disk leaving radii where the density is low relative to surrounding regions. This has relevance for protoplanetary disks where such gaps are believed to be opened when planets form, this requires self-gravity. Here gaps are forming without self-gravity being present. Rapid accretion due to locally enhanced transport has created these gaps.

Parameter	res4-ideal	res4-mf	480-mf-halldom
Maxwell Stress	-3.8858e-5	-5.6863e-5	-1.0254e-4
Reynolds Stress	3.335e-5	3.4966e-5	6.3112e-5
Alpha parameter	0.0264	0.0331	0.0589
Total Magnetic Energy	2.2873e-4	5.842e-4(max)	8.124e-4
Perturbed Kinetic Energy	6.845e-5	2.9805e-5	5.2047e-5

Table 7.1: Results from the main parameters for the ideal MHD (res4-ideal), full multifluid (res4-mf) and Hall dominated (480-mf-halldom) simulations at saturation (if saturation has occurred). Runs where saturation has not occurred will be indicated by (max) indicating the maximum value reached. These are time averaged values taken from the point of saturation to five orbital periods later.

Chapter 8

Zero-Net Flux and Initial Field Orientation

In this chapter, simulations are presented that compare the case where the disk is initially dominated by a net vertical field and the case where the disk has a zero net magnetic flux. Also examined, is the effect of the initial field configuration. Specifically the effect that the initial orientation of the net magnetic field with relation to the angular momentum vector is studied. As seen in section 2.4, this situation leads to the MRI being suppressed and the disk is stabilised.

The case where a zero net field configuration is present is also studied to see what effect such a magnetic field configuration has on the magnitude of angular momentum transport when non-ideal effects are included..

8.1 Zero-Net Flux case

The presence of net magnetic flux is known to enhance the MRI and lead to enhanced angular momentum transport. The strength of this initial field also leads to higher saturation values for the stresses and alpha parameter.

In the paper of Hawley and Balbus (1992), local 2-dimensional simulations were carried out in the ideal MHD framework which showed that in the case of a net flux the results agreed with results obtained by linear analysis, that is that the growth rate was affected by the magnitude of the initial flux,

with saturation levels rising with initial field strength. Turbulence was easily sustained with a net field but surprisingly in the case of a zero-net flux (averaged across the grid) turbulence grew quickly initially and then began to die away slowly and eventually disappearing. The behaviour of the zero-net case is a consequence of Cowlings anti-dynamo theorem (Moffatt, 1978), which does not allow for field amplification in an isolated axisymmetric MHD flow. The case of a net flux avoids this problem as it does not satisfy the requirement of isolation because the magnetic field effectively extends to infinity. This situation can exist in real disks where the magnetic field might close far from the midplane of the disk. The results of Hawley et al. (1995b) confirm these results using 3-dimensional local simulations.

A local 3-dimensional study, that of Fleming et al. (2000), which included limited resistive effects in the form of Ohmic diffusion confirmed the important result that the nonlinear turbulent state is easier to maintain when a mean vertical magnetic field is present. Turbulence is not maintained as easily when the initial field is toroidal. The orientation of the initial field is shown to have importance with regards to the properties of the saturated state. The global cylindrical simulations of Hawley (2001) again compared initial field orientations, including vertical and azimuthal orientations. It was found that the turbulence generated by the MRI is more vigorous and more efficient in producing stress for a given total magnetic pressure when driven by an initial field that is vertical rather than toroidal.

Some work has been done studying the effect of including or removing a net vertical flux in simulations which look at regions of accretion disks where ambipolar diffusion is the dominant non-ideal diffusive process, i.e. 30-100 AU. In the study of Bai and Stone (2011) they found that for simulations with a net toroidal magnetic flux, but no vertical magnetic flux, the turbulence dies away for $Am \leq 1$ where Am is a parameter that describes the frequency of ion-neutral collisions with respect to the dynamical timescale of the accretion disk. For sustained turbulence runs, the saturated turbulent stresses increase with increasing Am , eventually asymptoting towards the ideal MHD level. However, in the presence of a net vertical magnetic flux, turbulence can always be sustained even for $Am < 1$, assuming that the background vertical magnetic flux is weak enough. For low Am values, however, the resulting turbulence levels are still fairly small.

It is not known whether the Hall effect will enhance the MRI in the case of a zero-net flux. MRI turbulence may generate vertical fields locally and so in certain regions angular momentum transport may be enhanced and in others it may be suppressed where the generated vertical field is counter aligned with the net angular momentum vector of the disk. It may then be expected that these regions of enhancement and suppression may cancel each other out over the entire disk and that overall no significant enhancement or suppression may take place. Structure formation may also occur which helps with the formation of planets.

8.1.1 Numerical Set-up

To obtain a zero-net flux through the disk. The magnetic field is initially set to be purely toroidal and extremely small. This is done for stability reasons as HYDRA cannot handle regions where there is no magnetic field in the fully multifluid case, this is however not a problem in the ideal MHD case. These global simulations require a settling period at the beginning, which lasts approximately 10 orbital periods at $r=1.0$. The zero-net field that is to be implemented is sinusoidal in nature and is aligned with the rotation axis. The magnetic field is sinusoidal in form and is given by

$$B_z(r) = B_0 \sin \left(2n\pi \frac{(r - r_i)}{(r_o - r_i)} \right) \quad (8.1)$$

where r_i and r_o are the interior extent of the sinusoidal field and r itself varies from $0.8 \leq r \leq 2.38$, and B_0 is the maximum strength of the magnetic field and is set to 50mG. The parameter n is the number of waves and is set to 4. Overall, the net flux through the computational domain is zero.

However, if this form of magnetic field is present throughout the settling period, then magnetic pressure will cause local regions of strong magnetic field to expand into regions where the magnitude of the magnetic field is small. In the full multifluid code, some magnetic field must be present and so the seed magnetic field described above is injected with the perturbation to the velocity field so that the settling period be allowed to pass by without compromising the simulation. Until this time, a very small toroidal component is initially present on the grid which is of the order of $10^{-6} \times B_z$. A

toroidal component is chosen as no net flux exists through the computational box and this component is small enough to be negligible compared to the seed field described above. The B_x and B_y components are given by

$$B_x = \left(\frac{-n}{\sqrt{m^2 + n^2}} \right) B_\phi \quad (8.2)$$

$$B_y = \left(\frac{m}{\sqrt{m^2 + n^2}} \right) B_\phi \quad (8.3)$$

where $m = i\Delta x - (\Delta x/2)$ and $n = j\Delta y - (\Delta y/2)$ which describe the cell centered position of the cell (i, j) in the x, y plane. B_ϕ is the magnitude of the small azimuthal magnetic flux component.

The inner and outer wavekiller boundaries are set so that they drive the magnetic field to the initial toroidal condition. In this way, no overall net component can develop from the boundaries. The run ID of this simulation is 480-mf-zeronet.

8.1.2 Results

In the 480-mf-zeronet simulation, the Maxwell stresses are greatly reduced compared to the full multifluid case (res4-mf) (see Fig.8.1). The initial state of the magnetic field would allow regions where the MRI is enhanced or suppressed depending on radial position. In regions where the magnetic field strength is high the magnetic pressure will cause an expansion of the fluid into regions where the magnetic field is weak. As this settling occurs the vertical magnetic field component in all regions will get smaller and the azimuthal component of the magnetic field (not the initial magnetic field) begins to dominate. The Hall effect will therefore have minimal influence on the saturation level of the stresses except for diffusive effects. The diffusion allowed by both the Hall and ambipolar terms will suppress the MRI somewhat leading to a lower saturation than would be expected in the ideal MHD case (res4-ideal). The importance of a net field in determining the efficiency of the MRI process in developing turbulence is obvious.

Quantitatively, turbulence in the 480-mf-zeronet run is very weak compared to the same time in res4-mf (see Fig.8.2). This reflects the results for

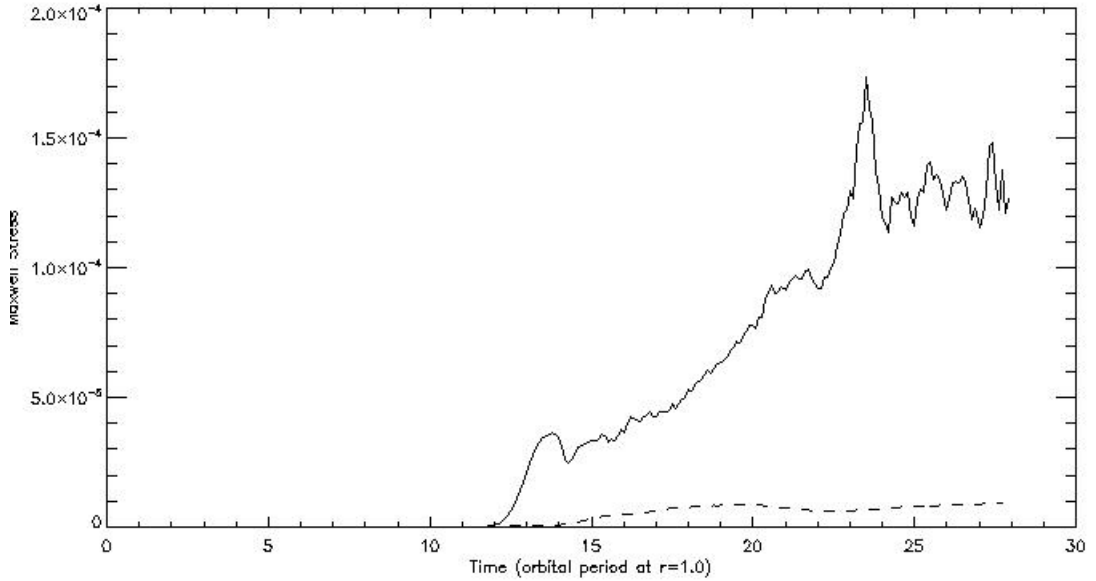


Figure 8.1: Plot of the Maxwell stresses for the res4-mf run (solid line) and the 480-mf-zeronet run (dashed line). A net field greatly enhances the MRI and leads to much more vigorous turbulence on the grid.

the stresses where the values Maxwell and Reynolds stresses at saturation are well below those of the full multifluid simulation. The Reynolds stresses are particularly small where the ratio of Maxwell stress to Reynolds stress 1.78 compared to 1.56 for the res4-mf run (see table 8.1 and Fig.8.3).

The saturation level of the alpha parameter in the 480-mf-zeronet run is approximately 6% of that seen in the res4-mf run (see Fig.8.11). Diffusive effects lead to a lessening of angular momentum transport which is parameterised by the alpha parameter.

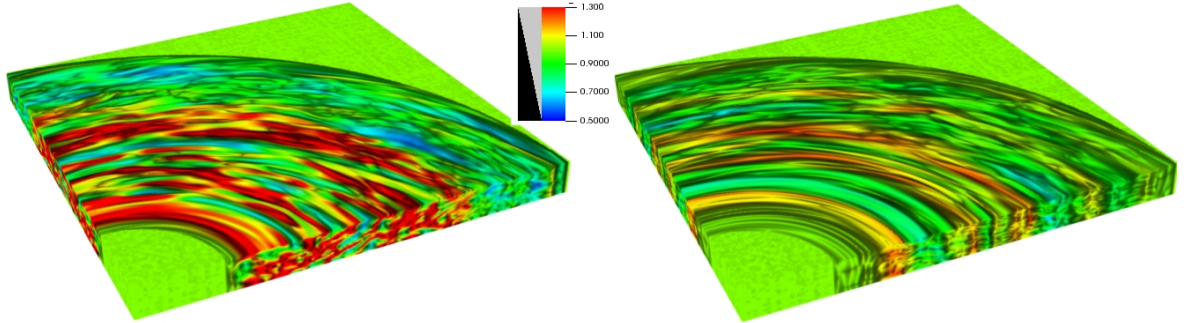


Figure 8.2: A volume plot of the neutral density for the res4-mf run (left frame) and 480-mf-zeronet run (right frame) after the disk has evolved through 20 orbits at $r=1.0$. Very weak turbulence is seen in the case of a zero-net flux through the computational domain. The full multifluid run shows very noticeable accretion taking place.

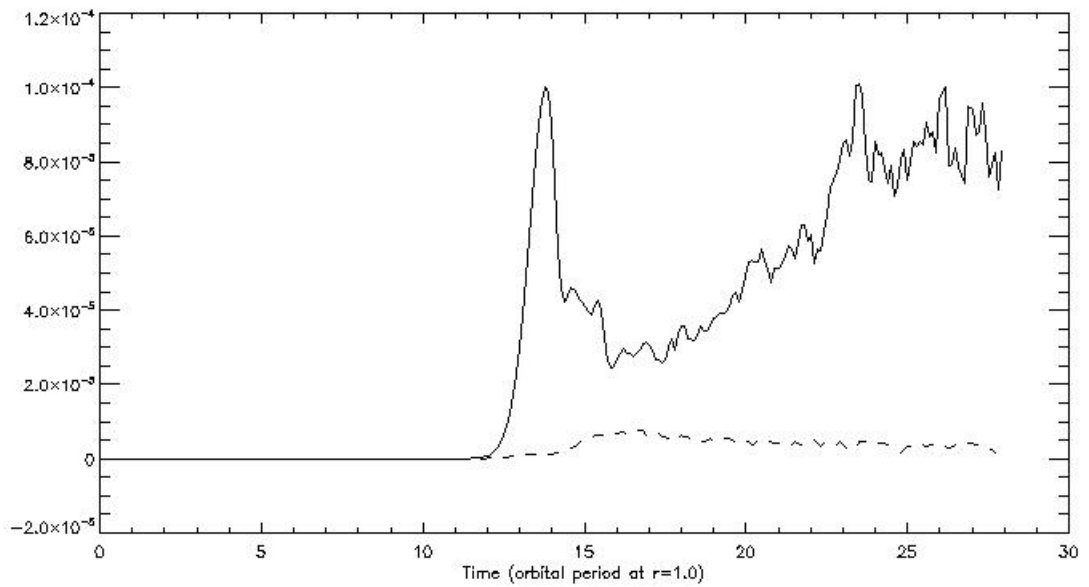


Figure 8.3: Plot of the Reynolds stress for the res4-mf (solid line) and 480-mf-zeronet (dashed line) runs. The Reynolds stresses in the zero-net case are very small compared to the full multifluid case.

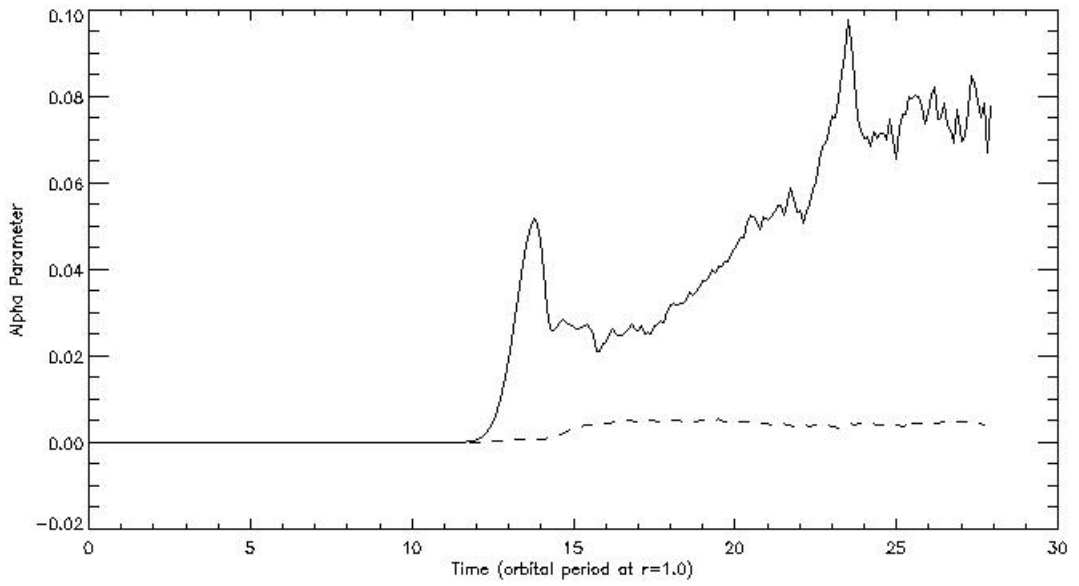


Figure 8.4: Plot of the alpha parameter for the res4-mf (solid line) and 480-mf-zeronet (dashed line) runs. The alpha parameter saturates at a significantly lower level than in the net flux case.

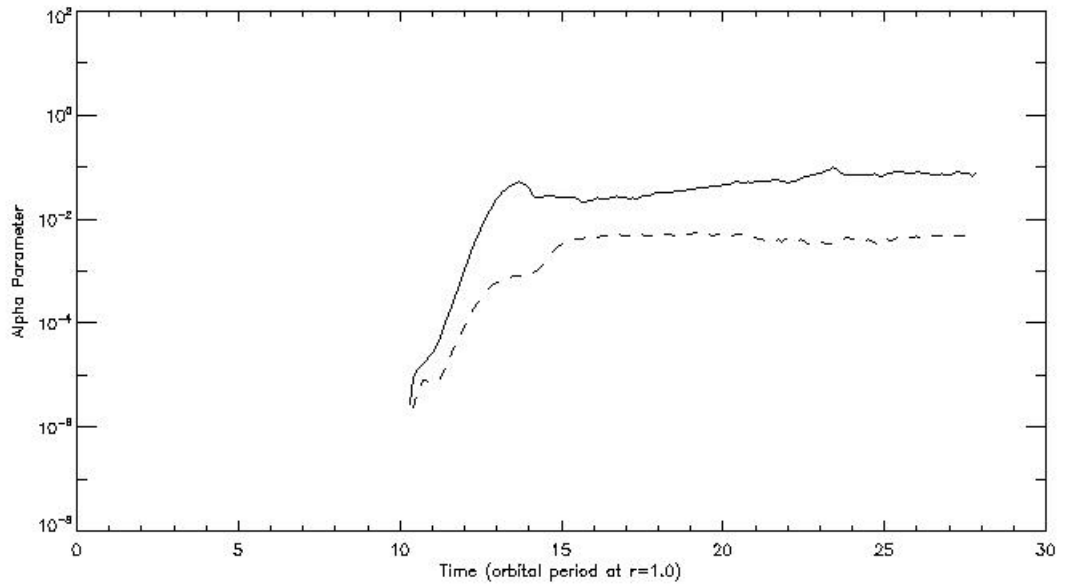


Figure 8.5: Log-linear plot of the alpha parameter for the res4-mf (solid line) and 480-mf-zeronet (dashed line) runs.

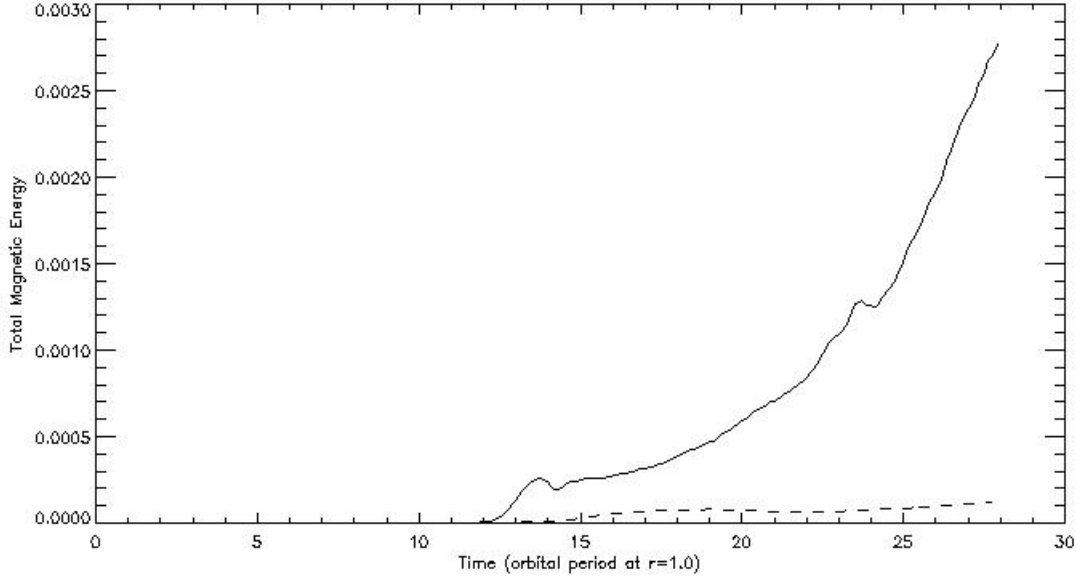


Figure 8.6: Plot of the total magnetic energy for the res4-mf (solid line) and 480-mf-zeronet (dashed line) runs.

Parameter	res4-mf	480-mf-zeronet	480-mf-minusbz
Maxwell Stress	-1.2987e-4	-7.7221e-6	-1.1243e-5
Reynolds Stress	8.3194e-5	4.2902e-6	1.4219e-5
Alpha parameter	0.07516	0.0045	0.00921
Total Magnetic Energy	0.002764 (Max)	8.040e-5	9.223e-5
Perturbed Kinetic Energy	6.845e-5	6.845e-05	1.874e-05

Table 8.1: Results from the main parameters for the res4-mf, 480-mf-zeronet and 480-mf-minusbz simulations at saturation (if saturation has occurred). Runs where saturation has not occurred will be indicated by (max) indicating the maximum value reached. These are time averaged values taken from the point of saturation to five orbital periods later.

The total magnetic energy in the 480-mf-zeronet does not show the seemingly unbounded exponential growth that is seen in the res4-mf and saturates relatively early in comparison. The saturation level does not vary much about the mean with time in the 480-mf-zeronet case (see Fig.8.6).

An initial field configuration which has an exactly zero net flux through

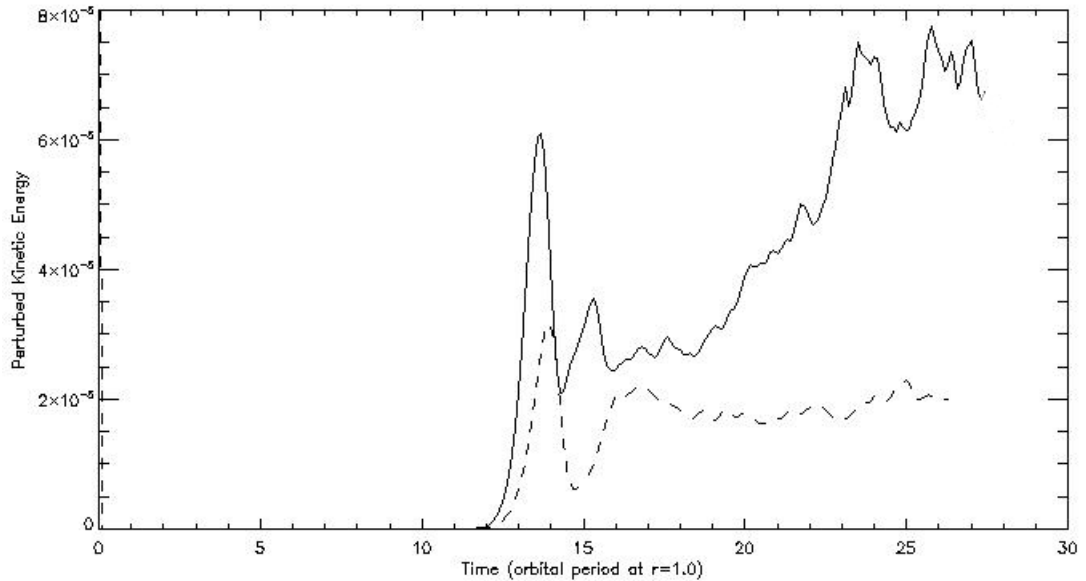


Figure 8.7: Plot of the perturbed kinetic energy for the res4-mf (solid line) and 480-mf-zeronet (dashed line) runs.

the computational box is probably unrealistic as a net field is a physically possible configuration and it is unlikely that such a physically exact zero net flux could exist over such a region of the disk. It is more likely that magnetic fields either from the central object or magnetic field which are present in the surrounding cloud (which is not part of the disk) will thread the disk and so a net field is a much more likely configuration.

8.2 Initial Magnetic Field Orientation relative to Rotation Axis of Accretion Disk

In this section, the results of a fully multifluid simulation identical to run res4-mf except for the orientation of the magnetic field are presented. The initial net magnetic field is initialised so that it is anti-parallel to the angular momentum vector. As outlined in section 2.4, this type of configuration is known to suppress the MRI as illustrated in Fig.2.3. This effect will be shown by direct comparison to run res4-mf and will confirm the local results of (Sano and Stone, 2002b) but for a global, fully multifluid disk model.

8.2.1 Numerical Set-up

The reversed orientation for the field is applied and the radial boundary conditions must be adjusted to drive the magnetic field present in the wavekilling zone to the initial field configuration. The numerical set-up in this model is exactly the same as in the full multifluid case except in the case of the initial net magnetic field which is set so as to be antiparallel to the net angular momentum vector of the disk (See 3.4 for details referring to the full multifluid model). The run ID for the Hall dominated case is 480-mf-minusbz.

8.2.2 Results

When the magnetic field is orientated antiparallel to the angular momentum vector of the disk the MRI is suppressed. This effect was first seen in the numerical results of Sano and Stone (2002a,b). The Maxwell stress saturates in this case at a level roughly 10% of that seen in the fully multifluid run with a net field parallel with the net angular momentum vector (res4-mf). Whereas the Reynolds stress saturates at roughly 17% of the same. Both the Maxwell and Reynolds stresses are close to uniform with time once saturated, whereas in the res4-mf case a lot time variability is seen (see Fig.8.8 and Fig.8.10). This is consistent with the results of Sano and Stone (2002b) where a global reversal of the magnetic field resulted in the MRI being suppressed.

Fig.8.9 compares the reversed initial field run with the res4-mf run. An interesting feature is that the MRI is almost completely quenched near the inner boundary and for some distance radially into the disk. The Hall effect seems to be acting to stabilise the disk at these inner radii as expected due to the initial magnetic field orientation. Weak turbulence is present at the outer radii. Some modes of the MRI are not completely suppressed. At later times the region remains free of turbulence and accreting material from the region where turbulence is active becomes non-turbulent.

The alpha parameter also saturates at a level which is approximately 10% that of that seen in the res4-mf run. Angular momentum transport is suppressed. The mechanism through which this suppression occurs is illustrated in Fig.2.3 and explained in the accompanying text. An order of magnitude drop in the alpha parameter is very significant change from the

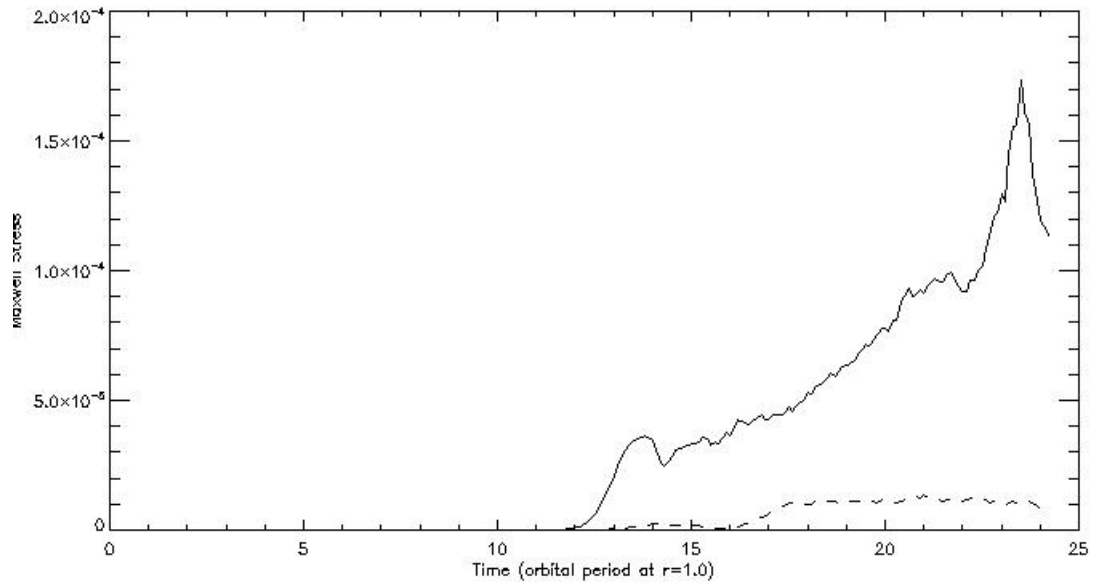


Figure 8.8: Plot of the Maxwell stresses for the res4-mf (solid line) and the 480-mf-minusbz (dashed line) runs.

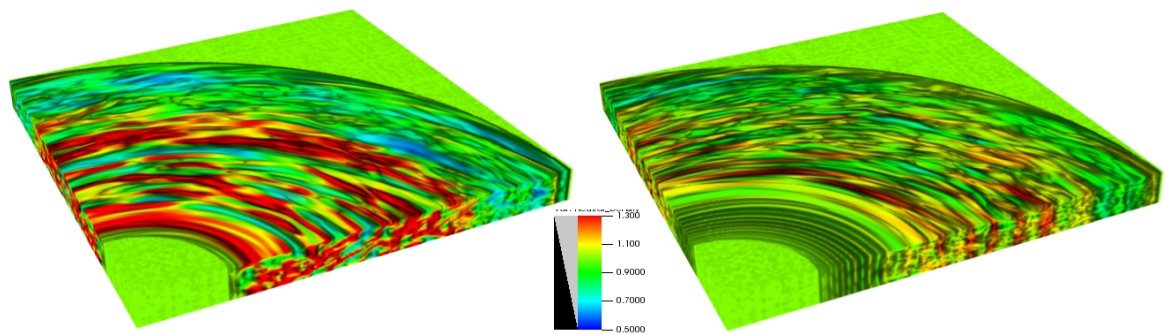


Figure 8.9: A volume plot of the neutral density for the full multifluid (res4-mf) (left frame) and multifluid case with reversed initial field(480-mf-minusbz) (right frame) after the disk has evolved through 20 orbits at $r=1.0$.

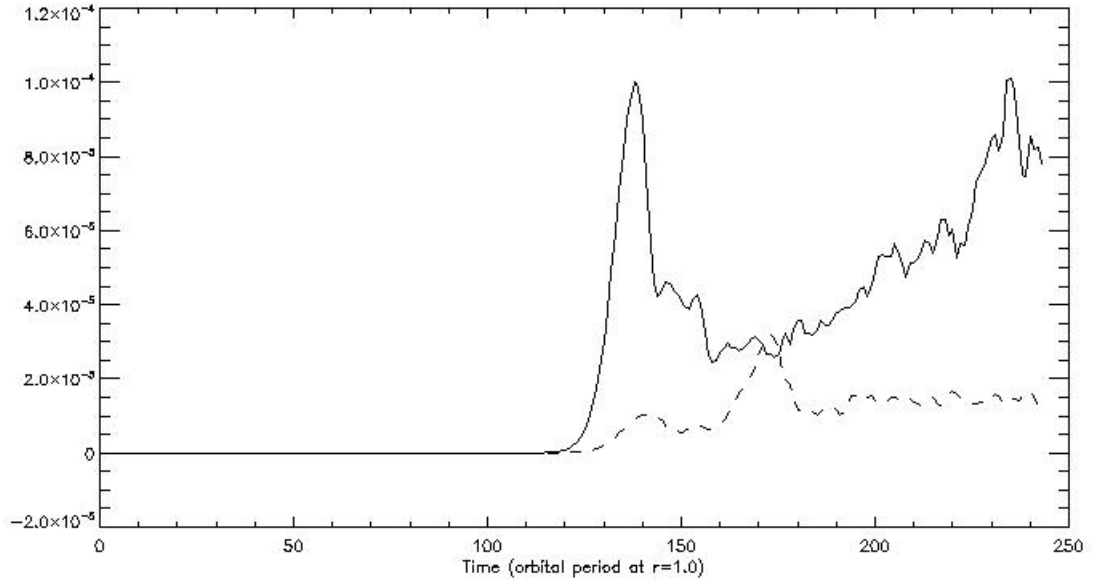


Figure 8.10: Plot of the Reynolds stresses for the res4-mf (solid line) and the 480-mf-minusbz (dashed line) runs.

full multifluid case with the net field aligned parallel with the net angular momentum vector.

The total magnetic energy saturates early compared to the fully multifluid case (res4-mf) and does not show the same unbounded exponential growth in the total magnetic energy. The total magnetic energy once saturated begins to decay very slowly over time. This rate of decay is small enough that it may be caused by the difference in the magnetic energy being transported through the radial boundaries of the grid, this may also be due to the slow stabilising of the disk due to the Hall effect.

The results obtained here stress the importance of the Hall effect for the efficient transport of angular momentum in accretion disks. Hall diffusion dominates much of the inner disk and so any enhancement or suppression of the MRI would have important consequences for the accretion disk as a whole possibly leading to large gaps in the disk. Also of importance is that the Hall effect makes it possible for regions such as the dead zone of the disk, previously thought to be free of MHD turbulence may actually be susceptible to the MRI.

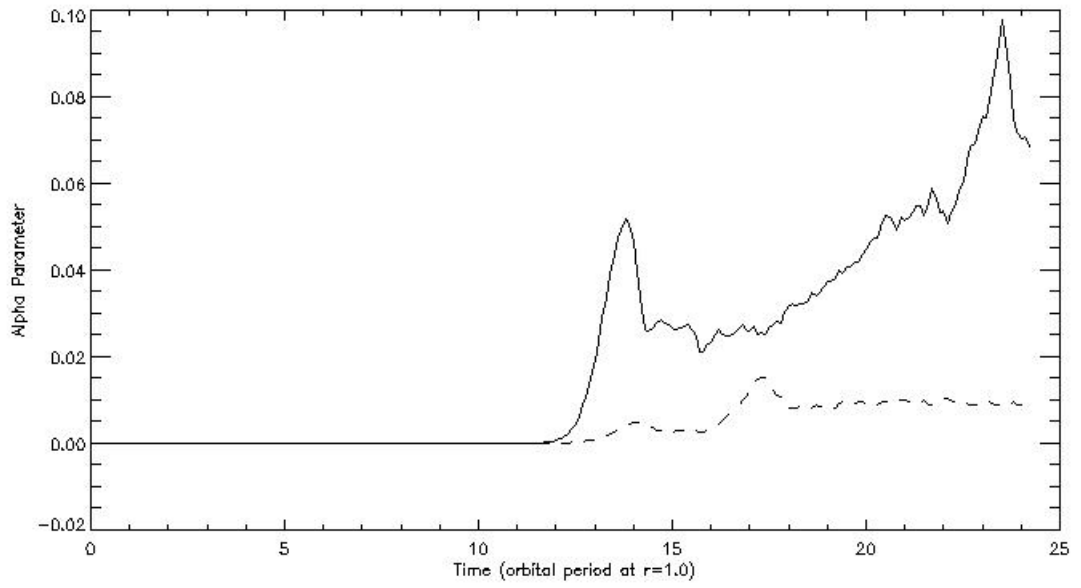


Figure 8.11: Plot of the alpha parameter for the res4-mf (solid line) and the 480-mf-minusbz (dashed line) runs.

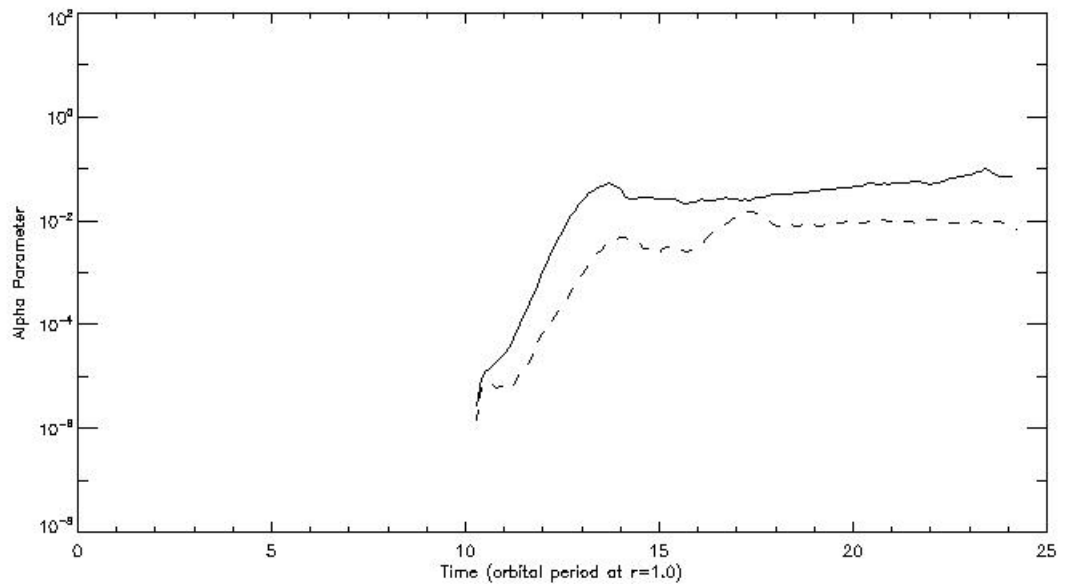


Figure 8.12: Log-linear plot of the alpha parameter for the res4-mf (solid line) and 480-mf-minusbz (dashed line) runs.

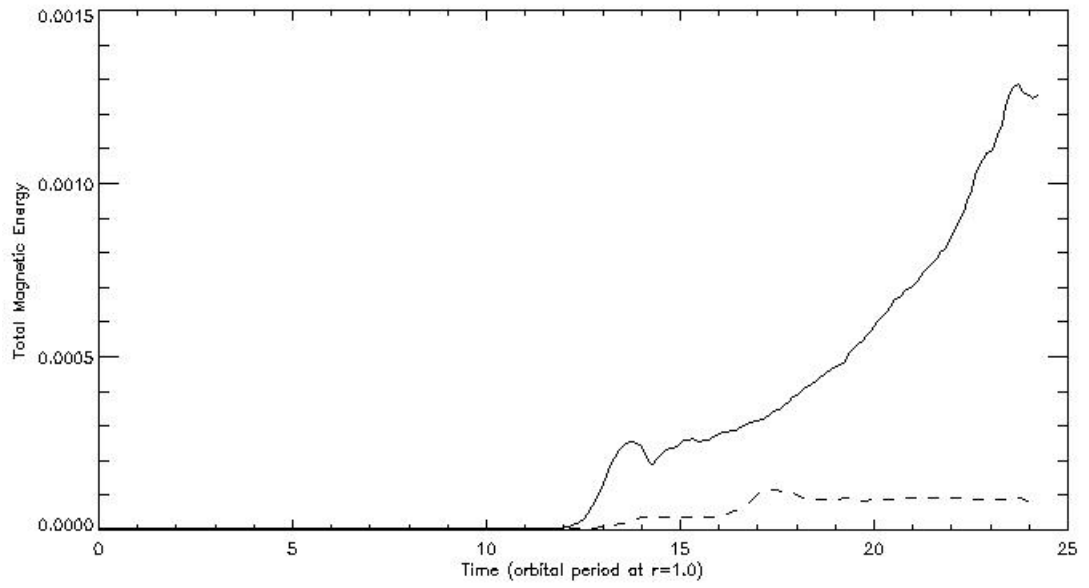


Figure 8.13: Plot of the total magnetic energy for the res4-mf (solid line) and the 480-mf-minusbz (dashed line) runs.

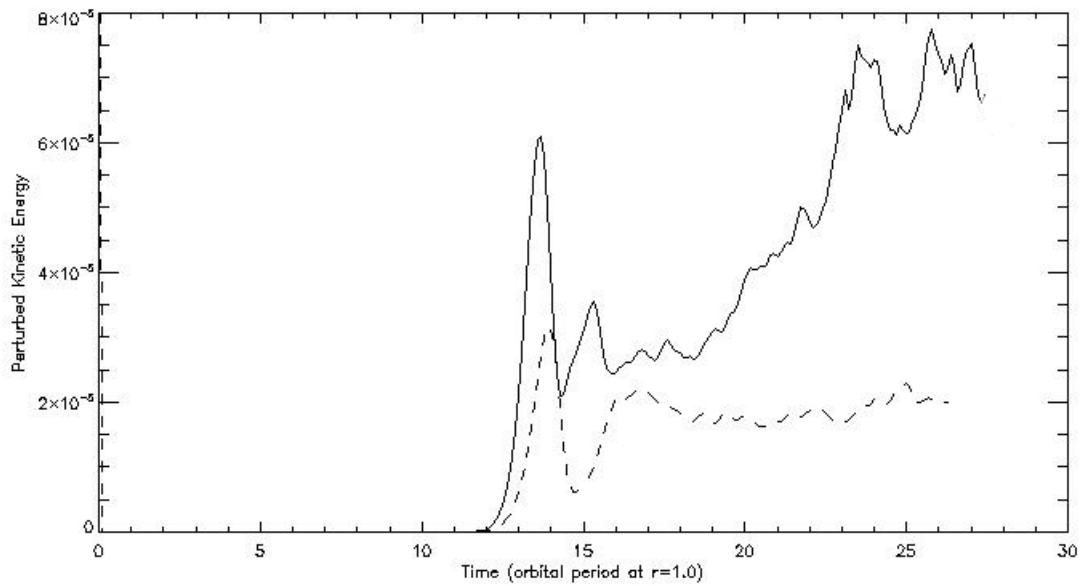


Figure 8.14: Plot of the perturbed kinetic energy for the res4-mf (solid line) and the 480-mf-minusbz (dashed line) runs.

Chapter 9

Discussion

This thesis contains a number of studies regarding the magnetorotational instability (MRI) in weakly ionised accretion disks around young stars. In particular, the consequences of the inclusion of non-ideal effects such as ambipolar diffusion and the Hall effect on the saturated state of the MRI are studied both quantitatively and qualitatively. The simulations described in the above work were carried out using the numerical code HYDRA which is described in detail in section 3.2. As HYDRA used an explicit scheme to carry out the integration of the multifluid MHD equations, it is possible to parallelise the algorithm easily. This makes very high resolution studies possible. HYDRA has been shown to scale well and so the maximum resolution allowable is realistically set by the computational resources available. The code was used to perform the very first fully multifluid global simulations of the magnetorotational instability using a cylindrical accretion disk model (see section 3.4 for details). Ideal and fully multifluid simulations are also carried out to ensure that a high enough resolution is being used so that the solution has converged and also so that the non-ideal multifluid effects are being adequately resolved.

HYDRA also makes it possible to isolate individual non-ideal effects so that consequence of a particular effect on the saturation amplitude of the MRI may be determined. Firstly a simulation with all non-ideal effects included is performed, and a point in evolution is reached so that information regarding the properties of the disk at saturation can be obtained. Next, a further two simulations are carried out where both ambipolar diffusion and the Hall

effect are individually isolated. The results obtained from these simulations make it possible to clearly see what influence each effect individually or in combination are having upon the disk evolution.

In chapter 5 results obtained from an ideal MHD simulation are compared to that of a fully multifluid MHD simulation which includes all non-ideal effects. The total magnetic energy was seen to grow exponentially and without bound in the fully multifluid case. It is concluded that the dynamo action that results from the turbulence driven by the MRI is enhanced by the inclusion of the non-ideal effects associated with weakly ionised plasma. This is surprising as Ohmic and ambipolar diffusion allows for the magnetic field to slip through the neutral fluid and so turbulence in the ionised fluids would not have as much of an effect on the neutral fluid as might be seen in the ideal MHD case with the bulk fluid. The stresses and alpha parameter are also significantly higher at saturation than the ideal MHD case. It is proposed that the Hall effect significantly enhances the dynamo associated with the MRI and further destabilises the accretion disk. It is shown that in the case of an initial vertical field that if just ambipolar and Ohmic diffusion are included, the magnetic field lines tend to straighten out and the disk MRI is suppressed. However, if the Hall effect is included, the drift due to Hall is in such a direction as to further destabilise the disk.

Power spectra of the neutral densities were calculated for both the ideal and full multifluid cases. There is considerably more power in all wavenumbers compared to the ideal MHD case. There is a concentration of power in the range $8 < k < 16$ in the full multifluid case whereas the opposite seems to be true in the ideal MHD case. At large length scales there is a significant difference in the power spectra showing that larger scale structures are present in the full multifluid case.

The effect that ambipolar diffusion has on the saturation of the MRI is investigated in chapter 6. The Hall effect is completely removed from the system. When the ambipolar dominated run is compared to the ideal MHD run a significant difference is seen in the stresses and the energies. In the ambipolar dominated case, the mean anomalous viscosity calculated at saturation is roughly 67% that of the ideal MHD case. Qualitatively it can be seen that the turbulence in the ambipolar dominated case is less severe than in the ideal MHD case. This is to be expected as the field lines can now

slip through the neutral fluid whereas in the ideal MHD case the field lines are in effect frozen into the bulk fluid. The absence of the Hall effect in the ambipolar dominated run ensures that the run away growth in the magnetic field is not allowed to develop. Turbulent motions are not able to wind and twist the magnetic field to the same degree as is seen in the ideal MHD case. The magnetic dynamo associated with the MRI is damped and the MRI is suppressed somewhat.

When the fully multifluid simulation is compared to the ambipolar dominated case, the Maxwell and Reynolds stresses are seen to saturate much early in the evolution in the disk. This is because when the Hall effect is excluded the total magnetic energies saturate shortly after the perturbation injection (within 5-8 orbits at $r=1.0$) whereas in the full multifluid case the total magnetic energies are seen to grow exponentially without bound. This behaviour is not seen in the ambipolar dominated case. The stresses are much more variable over short temporal ranges in the full multifluid case once saturation occurs. This is because of the significant accretion that takes place early on in the simulation meaning more of the mass and magnetic energy is concentrated in faster moving regions nearer the inner disk. The stresses can be seen to be higher at the inner regions of the disk than in the ambipolar dominated or ideal cases. Turbulence occurs on slightly smaller length scales in the ambipolar dominated case, showing that the Hall effect leads to turbulence acting on larger length scales and perhaps impedes the cascade of turbulent energy onto smaller lengthscales.

Next, the Hall effect is isolated by having ambipolar diffusion removed from the system. The effect this has upon the saturation of the MRI is investigated in chapter 7. Removal of ambipolar diffusion leads to a much higher saturation amplitude in the stresses and anomalous viscosity compared to the full multifluid and ideal MHD cases. The total magnetic energy when ambipolar diffusion is removed shows similar behaviour as in the full multifluid case. The exponential growth seen in the total magnetic energy is seen in the Hall dominated case and the rate of growth is roughly equal although the removal of ambipolar diffusion allows the total magnetic energy to jump to a higher level after the time of perturbation injection and before the exponential growth is seen to begin. This combined with the results obtained from the ambipolar dominated and full multifluid runs confirm that the Hall

effect is responsible for the behaviour seen in the total magnetic energies in the full multifluid case. It also confirms that the Hall effect is responsible for the enhancement of the MRI and the increased accretion that follows from this.

A simulation identical to the full multifluid case described in chapter 5 but with a global reversal of the magnetic field so that it is antiparallel with the net angular momentum vector was run. As expected from previous results in the literature, the saturation levels of the stresses and energies were much reduced compared to both the full multifluid and ideal MHD cases. The fact that the Hall effect now has a suppressing effect on the MRI, combined with the ambipolar diffusion means that the MRI leads to a much more stable disk overall. Some turbulence is present as the MRI is not completely quenched.

The case where a zero-net magnetic flux is present is also investigated. The stresses and energies again saturate at a very small level compared to the full multifluid and ideal MHD cases. Initially regions exist where the initial magnetic field is orientated in such a way to enhance or suppress the MRI. This is due to how the zero-net flux is obtained. As the disk evolves, the magnetic field becomes dominated by an azimuthal component. The stresses and energies saturate at a very low level compared to the ideal MHD and full multifluid cases. The Hall effect does not have an enhancing effect in the zero-net flux case. It may be naively assumed that with simulations of this type, a net vertical field is required for the Hall effect to have a significant enhancing effect. However, a situation where an exact zero-net flux exists is not likely to be found in reality so the results illustrating the enhancing property of the Hall effect may be considered to be applicable to accretion disks in the radial region studied here.

We conclude that the Hall effect in the region 4-12 AU of protostellar disks, where Hall is believed to dominate other non-ideal effects, has a considerable enhancing effect on the MRI, leading to considerably more accretion. This result is applicable in regions where the Hall effect is the dominant non-ideal process, as long as diffusion is not strong enough to suppress the MRI completely. This is believed to be the case in the range of 1-30 AU. The Hall effect can increase the turbulent lengthscale. The Hall effect can make it possible for banded structures and gaps to appear in the disk due to the enhancing or suppressing effect due to the inherent handedness of the

Hall effect. It is believed that planets are responsible for creating gaps in protoplanetary disks, however the results presented here suggest that the Hall effect may also be responsible for the appearance of gaps. It is clear that ideal MHD global simulations are simply not sufficient to give a clear picture of the properties of global accretion disks in this radial range due to the weak ionisation of the disk fluid.

The computational expenditure of the above work is considerable but not so extreme as to be impractical at the time this work was completed. The potential for future work is considerable. Simplifications which were made in building the accretion disk model used in this study can be relaxed. The use of a cylindrical disk in this work is the most extreme example. This was done to save computational time and limits the amount of information which can be obtained from the simulations. One recent result of Wardle and Salmeron (2012) is that the estimations of the depths of magnetically active regions in protostellar and protoplanetary disks are likely to be wildly inaccurate because the Hall effect can destabilise the disk to a greater depth than was thought. HYDRA can be used to test this hypothesis and quantify to what extent the Hall effect can destabilise a disk which contain large magnetically inactive regions. A stratified disk model with a spherical potential is required for this work. Much of the coding for this model is complete at the time of writing but the computational time was not available to fully test and run the required simulations. It is also possible with HYDRA to introduce dust grains. The introduction of dust is believed to extend the dead zone in the disk. What effect the introduction of a dust fluid has upon the above model and whether the dust fluid settles towards the midplane of the disk would be interesting. If Hall is dominant, can the Hall effect excite regions where the dust has caused them to become inactive to the MRI. A further investigation of the gap opening mechanism associated with the Hall effect would also be very interesting. This work, if carried out would greatly enhance the understanding of accretion disk physics.

Bibliography

- Alexiades, V., Amiez, G., Gremaud, P.A., 1996, *Comm. Num. Meth. Eng.*, 12, 31
- Alfvén, H., 1942, *Nature*, 150, 405
- André, P., Montmerle, T., 1994, *ApJ*, 420, 837
- Arlt, R., Rüdiger, G., 2001, *A&A*, 374, 1035
- Bai, Z.N., 2011, *ApJ*, 736, 2
- Bai, Z.N., Stone, J.F., 2011, *ApJ*, 739, 1
- Balbus, S.A., 2003, *Ann. Rev. Astron. Astrophys.*, 45, 555
- Balbus, S.A., Hawley, J.F., 1991, *ApJ*, 376, 214
- Balbus, S.A., Hawley, J.F., 1998, *Rev. Mod. Phys.*, 70, 1
- Balbus, S.A., Tarquem, C., 2001, *ApJ*, 552, 235
- Berger, M.J., Colella, P., 1989, *Journal of Computational Physics*, 82, 64
- Blaes, O.M., Balbus, S.A., 1994, *ApJ*, 421, 163
- Blitz, L., Fukui, Y., Kawamura, A., Leroy, A., Mizuno, N., Rosolowsky, E., 2007, *Protostars and Planets V*, 81
- Bodo, G., Mignone, A., Cattaneo, F., Rossi, P., Ferrari, A., 2008, *A&A*, 487, 1
- Bonanno, A., Urpin, V., 2008, *A&A*, 480, 27
- Brandenburg, A., Nordlund, A., Stein, R.F., Torkelsson, U., 1995, *ApJ*, 446, 741

- Carpenter, J.M., Sanders, D.B., 1998, *AJ*, 116, 1856
- Chacón, L., Knoll, D.A., Finn, J.M., 2002, *Phys. Lett. A*, 308, 187
- Chandrasekhar, S., 1960, *Proc. Natl. Acad. Sci.*, 46, 253
- Chen, X., Arce, H.G., Zhang, Q., Bourke, T.L., Launhardt, R., Schmalzl, M., Henning, T., 2010, *ApJ*, 715, 1344
- Ciolek, G.E., Roberge, W.G., 2002, *ApJ*, 567, 947
- Crutcher, R.M., 2012, *Ann. Rev. Astron. Astro.*, 50, 29
- Dedner, A., Kemm, F., Kröner, D., Munz, C.D., Schnitzer, T., Wesenberg, M., 2002, *Journal of Computational Physics*, 175, 645
- Downes, T.P., 2012, *MNRAS*, 425, 2277
- Downes, T.P., O’Sullivan, S., 2009, *ApJ*, 701, 1258
- Downes, T.P., O’Sullivan, S., 2011, *ApJ*, 730, 12
- Enoch, M.L., Evans, N.J., Sargent, A.I., Glenn, J., 2009, *ApJ*, 684, 1240
- Enoch, M.L., Lee, J.E., Harvey, P., Dunham, M.M., Schnee, S., 2010, *ApJ*, 722, L33
- Falle, S.A.E.G., 2003, *MNRAS*, 344, 1210
- Ferrière, K.M., 2001, *Rev. Mod. Phys.*, 25, 23
- Fleming, T.P., Stone, J.M., Hawley, J.F., 2000, *ApJ*, 530, 467
- Fricke, K., 1969, *A&A*, 1, 388
- Goodman, A.A., Benson, P.J., Fuller, G.A., Myers, P.C., 1993, *ApJ*, 406, 528
- Goodman, J., 1993, *ApJ*, 406, 596
- Gullbring, E., Hartmann, L., Briceño, C., Calvet, N., 1998, *ApJ*, 492, 323
- Haisch, K.E., Lada, E.A., Lada, C.J., 2001, *AJ*, 553, L153
- Hawley, J.F., 2000, *ApJ*, 528, 462

Hawley, J.F., 2001, *ApJ*, 554, 534

Hawley, J.F., Balbus, S.A., 1992, *ApJ*, 400, 595

Hawley, J.F., Gammie, C.F., Balbus, S.A., 1995a, *ApJ*, 440, 742

Hawley, J.F., Gammie, C.F., Balbus, S.A., 1995b, *ApJ*, 440, 742

Hawley, J.F., Gammie, C.F., Balbus, S.A., 1996, *ApJ*, 464, 690

Hawley, J.F., Stone, J.M., 1995, *Comp. Phys. Comm.*, 89, 127

Hawley, J.F., Stone, J.M., 1998, *ApJ*, 501, 758

Heitsch, F., Mac Low, M.M., Klessen, R.S., 2000, *ApJ*, 547, 280

Ilgner, M., Nelson, R.P., 2006a, *A&A*, 445, 205

Ilgner, M., Nelson, R.P., 2006b, *A&A*, 445, 223

Jeans, J.H., 1902, *Phil. Trans. of the R. Soc. of London. Series A*, 199, 1

Jones, A.C., Downes, T.P., 2011, *MNRAS*, 418, 390

Jones, A.C., Downes, T.P., 2012, *MNRAS*, 420, 817

Kant, I., 1755, *Universal Natural History and Theory of Heaven*

Klahr, H.H., Bodenheimer, P., 2003, *ApJ*, 582, 869

Konigl, A., Ruden, S.P., 1993, *Protostars & Planets III*

Kunz, M.W., Balbus, S.A., 2004, *MNRAS*, 348, 355

Lada, C.J., 1987, *Star forming regions; Proceedings of the Symposium, Tokyo, Japan, Nov. 11-15 1985*, 1

Laplace, P.S., 1796, *Exposition du Système du Monde*

Larmor, J., 1919, *Report of the British Assoc. of Adv. Science*, 87, 159

Larson, R.B., 1969, *MNRAS*, 145, 271

Larson, R.B., 2002, *ASP Conference Series*, 285, 442

Larson, R.B., 2003, *Rep. Prog. Phys.*, 66, 1651

Lawson, W.A., Lyo, A.R., Muzerolle, J., 2004, MNRAS, 351, L39

Lees, A.W., Edwards, S.F., 1972, J. Phys. C : Solid State Phys, 5, 1921

Lynden-Bell, D., 1969, Nature, 223, 690

Lyra, W., Johansen, A., Klahr, H., Piskunov, N., 2008, A&A, 479, 883

Mac-Low, M.M., Norman, M.L., Konigl, A., Wardle, M., 1995, ApJ, 442, 726

Mamajek, E.E., Meyer, M.R., Liebert, J., 2002, AJ, 124, 1670

Masunaga, H., Inutsuka, S., 2000, ApJ, 531, 350

Matsumoto, R., Shibata, K., 1997, ASP Conference Series, 121, 443

Mininni, P.D., Gómez, D.O., Mahajan, S.M., 2003, ApJ, 584, 1120

Moffatt, H.K., 1978, Magnetic field generation in electrically conducting fluids

Mouschovias, T.C., Spitzer Jr., L., 1976, ApJ, 206, 753

Muzerolle, J., Calvet, N., Briceno, C., Hartmann, L., Hillenbrand, L., 2000, ApJ, 597, L149

Norman, C., Hayvaerts, J., 1985, A&A, 147, 247

Oishi, J.S., Mac Low, M.M., 2006, ApJ, 638, 281

O'Sullivan, S., Downes, T.P., 2006, MNRAS, 366, 1329

O'Sullivan, S., Downes, T.P., 2007, MNRAS, 376, 1658

Pandey, B.P., Wardle, M., 2008, MNRAS, 385, 2269

Pandey, B.P., Wardle, M., 2012, MNRAS, 423, 222

Powell, K.G., Roe, P.L., Linde, T.J., Gombosi, T.I., De Zeeuw, D.L., 1999, Journal of Computational Physics, 154, 284

Pringle, J.E., 1981, ARA&A, 19, 137

Regev, O., Umurhan, O.M., 2008, A&A, 481, 21

Richardson, L.F., 1911, Phil. Trans. Royal Soc. London, 210, 307

- Romanova, M.M., Ustyugova, G.V., Koldoba, A.V., Lovelace, R.V.E., 2011, MNRAS, 416, 416
- Saigo, K., Tomisaka, K., Matsumoto, T., 2008, ApJ, 674, 997
- Salmeron, R., Wardle, M., 2003, MNRAS, 345, 992
- Sanders, D.B., Scoville, N.Z., Solomon, P.M., 1985, ApJ, 289, 373
- Sano, T., Stone, J.M., 2002a, ApJ, 570, 314
- Sano, T., Stone, J.M., 2002b, ApJ, 577, 534
- Shakura, N.I., Sunyaev, R.A., 1973, A&A, 24, 337
- Sheikhnezami, S., Frenzt, C., Porth, O., Vaidya, B., Ghanbari, J., 2012, ApJ, 757, 65
- Shu, F., 1991, Physics of Astrophysics, Vol II: Gas Dynamics
- Shu, F., Najita, J., Galli, D., Ostriker, E., Lizano, S., 1993, Protostars and Planets, III, 3
- Shu, F.H., Adams, F.C., Lizano, S., 1987, ARA&A, 73, 1031
- Sievers, A.W., Mezger, P.G., Gordon, M.A., Kreysa, E., Haslam, C.G.T., Lemke, R., 1991, A&A, 251, 231
- Simon, J.B., Bai, X.N., Stone, J.M., Armitage, P.J., Beckwith, K., 2013, ApJ, 764, 16
- Simon, J.B., Hawley, J.F., Beckwith, K., 2009, ApJ, 690, 974
- Skrutskie, M.F., Dutkevitch, D., Strom, S.E., Edwards, S., Strom, K.M., Shure, M.A., 1990, AJ, 99, 1187
- Stark, A.A., Lee, Y., 2006, ApJ, 641, L113
- Stone, J.M., 2011, IAU Symposium 2010, 274, 422
- Stone, J.M., Balbus, S.A., 1996, ApJ, 464, 363
- Stone, J.M., Hawley, J.F., Gammie, C.F., Balbus, S.A., 1996, ApJ, 463, 656
- Strang, G., 1968, SJNA, 5, 506

Swedenborg, E., 1734, Principia, volume 1

Tomisaka, K., 2002, ApJ, 575, 306

Tomisaka, K., Tomida, K., 2011, Publ. Astron. Soc. Japan, 63, 1151

Toomre, A., 1964, ApJ, 139, 1217

Umebayashi, T., Nakano, T., 1990, MNRAS, 243, 103

Velikhov, E.P., 1959, JETP, 36, 1398

Visier, Visier service catalogue, <http://vizier.u-strasbg.fr/>

Wardle, M., 2004a, AP & SS, 292, 317

Wardle, M., 2007, Ap&SS, 311, 35

Wardle, M., Ng, C., 1999, MNRAS, 303, 239

Wardle, M., Salmeron, R., 2012, MNRAS, 422, 2737

Williams, J.P., Blitz, L., Stark, A.A., 1995, ApJ, 451, 252

Wolk, S.J., Walter, F.M., 1996, AJ, 111, 2066

Zuckerman, B., Palmer, P., 1974, ARA&A, 12, 279